IN SITU FRINGE PROJECTION PROFILOMETRY FOR LASER POWER BED FUSION PROCESS

by

Bin Zhang

A dissertation submitted to the faculty of
The University of North Carolina at Charlotte
in partial fulfillment of the requirements
for the degree of Doctor of Philosophy in
Optical Science & Engineering

Charlotte

2017

Approved by:

_____
Dr. Angela Davies

_____
Dr. Faramarz Farahi

_____
Dr. John Zeigert

_____
Dr. Christopher Evans

_____
Dr. Brigid Mullany

ABSTRACT

BIN ZHANG. In situ fringe projection profilometry for laser powder bed fusion process. (Under the direction of DR. ANGELA DAVIES)

Additive manufacturing (AM) offers an industrial solution to produce parts with complex geometries and internal structures that conventional manufacturing techniques cannot produce. However, current metal additive process, particularly the laser powder bed fusion (LPBF) process, suffers from poor surface finish and various material defects which hinder its wide applications. One way to solve this problem is by adding in situ metrology sensor onto the machine chamber. Matured manufacturing processes are tightly monitored and controlled, and instrumentation advances are needed to realize this same advantage for metal additive process. This encourages us to develop an in situ fringe projection system for the LPBF process. The development of such a system and the measurement capability are demonstrated in this dissertation. We show that this system can measure various powder bed signatures including powder layer variations, the average height drop between fused metal and unfused powder, and the height variations on the fused surfaces. The ability to measure textured surface is also evaluated through the instrument transfer function (ITF). We analyze the mathematical model of the proposed fringe projection system, and prove the linearity of the system through simulations. A practical ITF measurement technique using a stepped surface is also demonstrated. The measurement results are compared with theoretical predictions generated through the ITF simulations.

ACKNOWLEDGMENTS

I sincerely thank my advisor Dr. Angela Davies for her supportive supervision. I was a novice in doing research when I first came as a Ph.D. student. Dr. Davies kindly showed me the way and taught me to think critically and positively. Thank my co-advisors, Dr. John Ziegert and Dr. Faramarz Farahi, who had supervised me while Dr. Davies was away. I couldn't appreciate more for their time, help and good advice. Thank my committee member, Dr. Christopher Evans, for the discussion of my research questions and the feedback to my dissertation. Thank my parents who were far apart from me in China while I was completing my Ph.D. in the United States. Your love has always been unconditional. Thank my friend, Yuanye Liu, for giving me feedback on the draft of this dissertation. Thank the funding sponsors – Edison Welding Institute, America Makes and National Institute of Standards and Technology. This project wouldn't be possible without them.

TABLE OF CONTENTS

LIST OF TABLES

LIST OF FIGURES

LIST OF ABBREVIATIONS

AM	additive manufacturing
CMOS	complementary metal-oxide-semiconductor
DLP	digital light processing
DMD	digital micromirror device
DMLS	direct metal laser sintering
DSLR	digital single-lens reflex (camera)
EBM	electron beam melting
ESF	edge spread function
FFT	fast Fourier transform
ITF	instrument transfer function
LBM	laser beam melting
LPBF	laser powder bed fusion
LSF	line spread function
NIR	near infrared
MTF	modulation transfer function
OTF	optical transfer function
PSF	point spread function
RMS	root mean square
SLM	selective laser melting
SLS	selective laser sintering

CHAPTER 1: OVERVIEW OF IN SITU METROLOGY FOR METAL ADDITIVE MANUFACTURING

1.1 Introduction

Additive manufacturing (AM) is the process which parts are fabricated by adding material layer by layer, as opposed to subtractive manufacturing, where parts are produced by material removal processes such as cutting, milling and turning. AM is sometimes called the third industrial revolution as it extends the current manufacturing ability to create parts with complex geometries and internal structures more economically [1]. Among all the AM technologies, metal AM is of great importance [2]. One primary reason is that metal is the most important industrial material. Compared to conventional metal manufacturing techniques, such as casting and machining, metal AM has several distinct advantages. One of the biggest benefits is that it uses less material by making topology-optimized shapes that eliminate unnecessary bulk. Material conservation is important to manufacturing. Less material means lower cost per product. Since AM process is carried out in a layered manner, there is more freedom to invent novel geometries without the current limitations. One example is the hinge bracket used on the Airbus A320 as shown in Figure 1-1 (a). The back part is made by the conventional steel casting process, while the front component is created by the metal AM process called direct metal laser sintering (DMLS). The AM bracket uses over 30% less material than its conventional counterpart but remains the same strength. The AM part is topology optimized and has an increased geometry complexity that cannot

be made by any existing technologies. The AM process also improves the functionality because of the weight reduction, which leads to an increase in fuel efficiency.

Another advantage is evident in the manufacture of medical implants [3]. The medical industry has already taken advantage of metal AM process to make customized implants [4]. Each human body is different and the additive process is the ideal way to make the customized part economically. In addition, the metal AM process can produce special surfaces that cannot be made other ways. One example is the acetabular cup implants made by the electron beam melting (EBM) process. The porous structure on the cup surface, as shown in Figure 1-1 (b), create what is called an osseointegrated connection between the natural bone and the implant. This special surface can significantly help the healing process.

Last but not the least, metal AM can expedite the manufacturing process when handling complex parts [5]. One primary reason is that it simplifies the process. The part made from many components can be created at once using an AM process; therefore, it saves time and money by eliminating an assembly step. The adoption of metal AM machines has an added economic value because one AM system can potentially replace multiple conventional tools. Although the current metal AM process is still slow and not yet error-free, it can be improved with higher power lasers and better scan strategies [6].

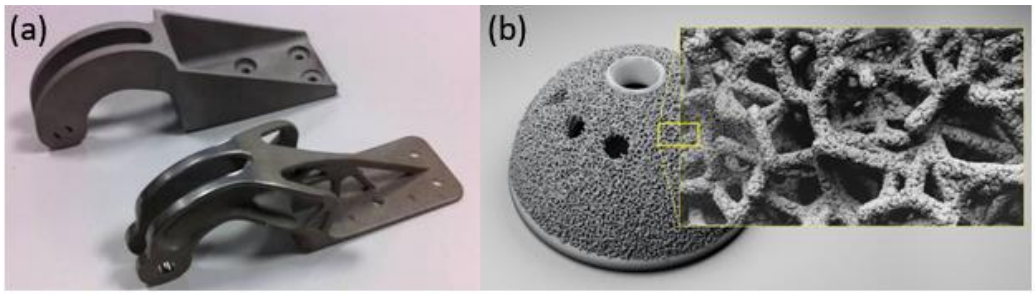

Figure 1-1: Examples of additively manufactured parts. (a) Topology optimized titanium nacelle hinge (front) and conventional steel cast nacelle hinge (back) [7]. (b) Acetabular cup implant produced by AM process [8].

Many metal AM processes exist. We only focus on one process called laser powder bed fusion (LPBF) in this dissertation. The LPBF process involves the direction of a focused laser beam over a flat metal powder surface. Figure 1-2 illustrates the operational principals. The laser beam is manipulated by a galvanometer laser scanner such that the powder being scanned is fused to solid metal. Melting, sintering or both can happen during the laser fusion. After the fusion, the build platform lowers by the thickness of a layer. A new layer of powder is spread atop the previous layer, and the laser fuses the powder again. In this manner, a 3D metal part can be built layer by layer.

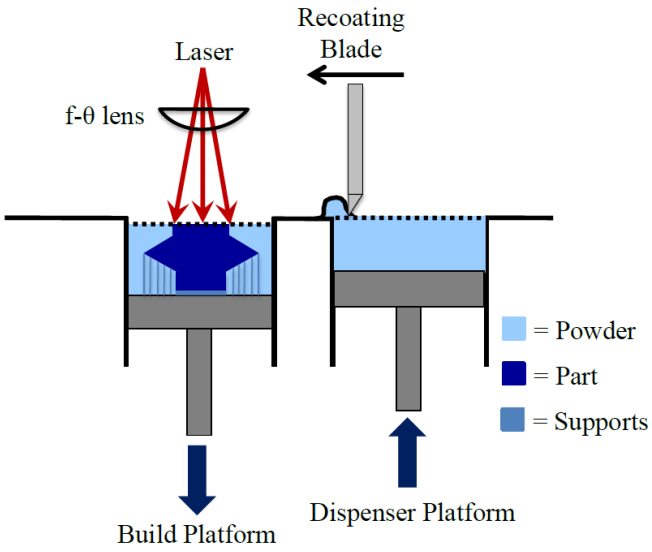

Figure 1-2: Laser powder bed fusion process [9].

Industrial LPBF systems, such as the EOS DMLS system [10] and the 3D System selective laser sintering (SLS) systems [11], are already available, and industry is showing great interest in capitalizing on the new technology [12]. However, commercial LPBF systems have not yet been widely adopted due to current limitations. One, perhaps the most significant, limitation is the inability to achieve consistent mechanical properties, even with nominally the same material and process parameters [13]–[15]. The mechanical properties

are directly related to the nature of the process where the metal powder is fused layer by layer and defects can occur during the fabrication. An example is porosity variability which directly impacts the hardness of the part [16]. Gas pores generated at one layer will be buried under the next layer. Post-process detection is almost impossible other than with X-ray tomography which is costly. If the voids could be detected on the layer when they were created, action could be taken to remove the voids [17].

Poor surface finish is another common limitation [18]–[21]. The relationship between surface finish and the process parameter is complex and largely still unknown. Post-process treatment is virtually always needed to meet the required surface specifications [22]. However, finishing the surface after the part has been built is possible only when the shape of the part is simple. For many situations where the part has a complex geometry and internal features, post-process treatment is extremely challenging or even impossible. This contradicts the most important advantage of AM process, namely the ability to produce complex geometry. If surfaces could be measured in situ and correlated to the input parameters, the information could be used to tune process parameters to yield a desired surface finish.

In situ metrology has the potential to address these metal AM limitations and more. There are two important aspects offered by in situ measurement. First, measurements add to our knowledge about the physics behind AM processes and expedite process development that leads to improved material and structural properties. Second, real-time monitoring allows for possible active feedback control to compensate or correct detected errors or to abort continued fabrication of defective parts.

1.2 Overview of In situ Metrology for LPBF Process

Everton, et. al. have reviewed current in situ metrology systems for metal AM [23]. There are roughly two classes of in situ metrology systems for an LPBF process – in-line and off-line systems. An in-line metrology system is a system which looks through the scanner head and the *f-θ* lens of an LPBF machine onto the fusion area. The optical path of the sensor is coaxial with the laser beam. Studies related to in-line systems primarily investigate the measurements of melt pool temperature and dimension [24]–[27]. An off-line metrology system is a system which is not coaxial with the laser beam. Instead, the system is usually installed outside of the machine chamber and looks through an optical window into the machine chamber. The primary reason for this configuration is to avoid damage and contamination from fusion splatter. Examples of the two types of metrology systems are discussed below.

1.2.1 In-line Systems

The in-line metrology system developed at the University of Leuven is shown in Figure 1-3. The system consists of a low-resolution high-speed CMOS camera and a photodiode. The camera and the photodiode are configured coaxially with the laser beam such that the monitoring area is always around the fusion region. This is achieved with a special mirror which reflects the laser light (at 1064 nm) and transmits part of the near-infrared light radiated by the melt pool (780 nm to 900 nm). A beam splitter was placed after the mirror to separate the signal to the camera and the photodiode. The camera takes images of the melt pool at a frame rate of 10 kHz with a resolution of 20 × 16 pixels, and the photodiode measures the average radiation flux of the melt pool continuously. This in-

line camera system is primarily used to measure melt pool dimension and melt pool temperature history during LPBF process, and the applications of the system have been investigated both on a commercial SLM system from Concept Laser [24] and on an in-house developed SLM system [25]–[27]. The main goal of the investigation is to find the correlations between the process errors, such as stage error, balling and overheating, and the change in the received signals, in both the camera images and the photodiode signal. Preliminary studies have shown some interesting results. They demonstrated a correlation between an increase of the photodiode output and a z-stage error [24]. They also developed an elliptical fitting algorithm to calculate the area and the length-to-width ratio of the melt pool [25]. They showed that a balling problem caused by scanning of an overhang region could be detected by an increase of the length-to-width ratio of the melt pool. They also found the correlations between an overheating problem and an increase of radiation flux received by the photodiode and an increase of the length-to-width ratio detected by the camera.

An improvement of the system is later made to expand the measurement area, i.e. to stitch all local images together to generate an irradiance signal map of the full powder bed using the location registered by the laser scanner [26]. This advances detection of more process defects, such as deformation caused by thermal stress and the overheating at an overhang region. Figure 1-4 demonstrates this improvement. Figure 1-4 (a) shows the stitched irradiance map of a rectangular part where a deformation was detected at the bottom right corner. The deformation on the build layer led to the defocus of the camera, causing the received radiation signal lower than the rest of the molten area. With development of advanced automation and control algorithm, more applications were

subsequently demonstrated. For example, some voids on the x-z plane were detected by stacking the measurements from different layers as shown in Figure 1-4 (b) [27].

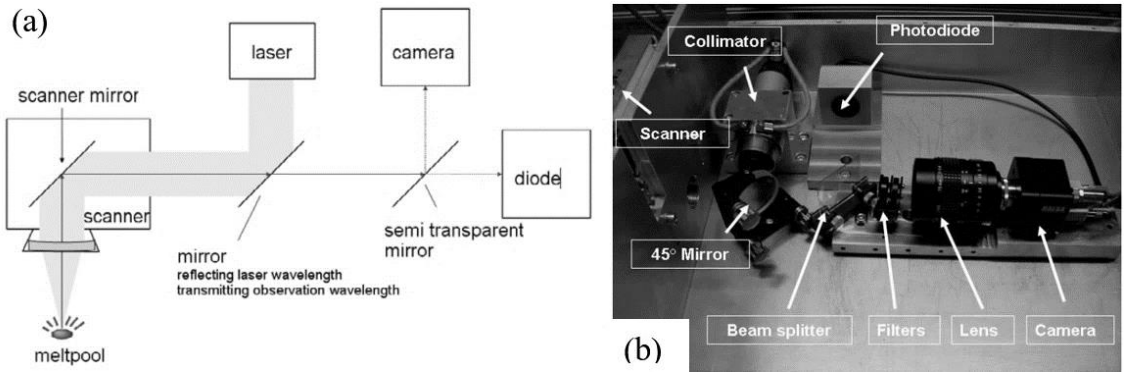

Figure 1-3: In-line monitoring the melt pool signatures with a camera and a photodiode [24], [25]. (a) Schematic diagram of the system. (b) Photo of the system highlighting the primary components.

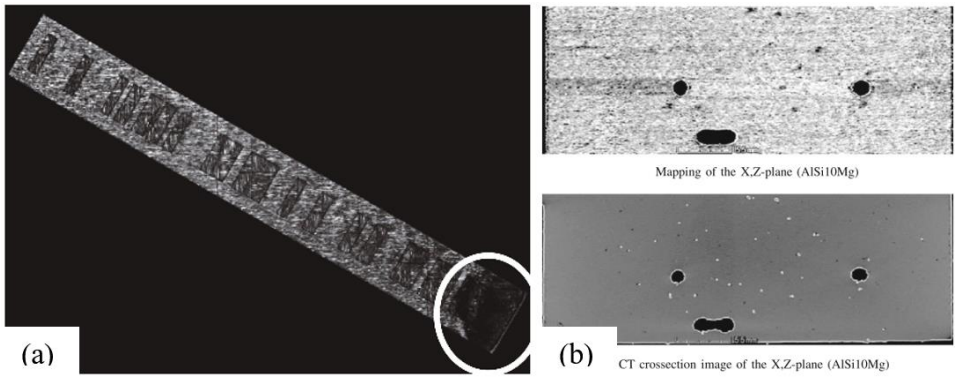

Figure 1-4: Results from the improved in-line monitoring system at University of Leuven. (a) A stitched map of local melt pool images shows a layer deformation [26]. (b) Comparison of a stitched image with an X-ray CT scan on the x-z plane.

Pavlov et al. developed an in-line pyrometer for a commercial SLM machine, Phenix PM-100 [28]. The schematic diagram of the system is shown in Figure 1-5 (a). A band-pass mirror was used to filter the laser beam and transmit the melt pool radiation to the pyrometer. They demonstrated that the pyrometer reading was correlated to process parameters such as the powder layer thickness, the hatch distance, and the scan velocity. Figure 1-5 (b) is an example of the pyrometer output. A significantly low signal occurred

at around 0.8 seconds when the laser fused a region where the powder layer is thinner than the average layer thickness.

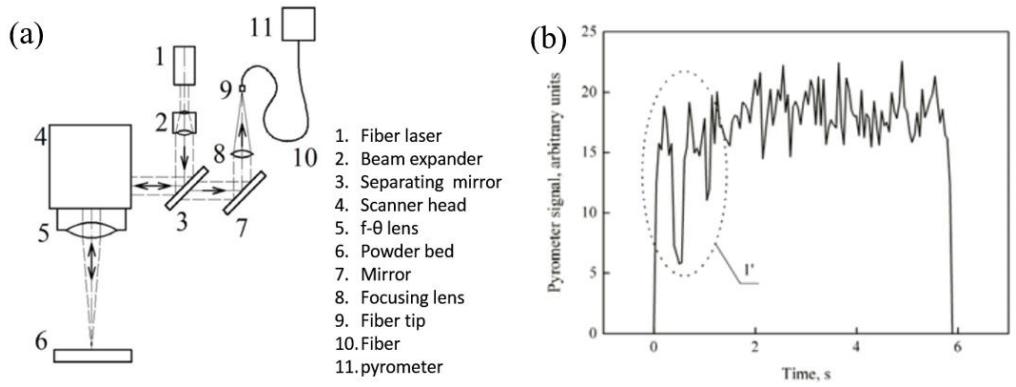

Figure 1-5: Pavlov's in-line pyrometer system. (a) Schematic diagram of the system. (b) The pyrometer output showing a signal change caused by a thin powder region.

Lott et al. designed an in-line optical system to monitor high scanning velocities and melt pool dynamics [29]. The system integrated a high-speed camera and an illumination laser coupled to the laser scanner. Instead of monitoring the near infrared radiation of the melt pool, like the in-line metrology system developed at the University of Leuven, Lott's system captured the scattered light of the illumination laser. The system measured a maximum area of 3.58 × 3.58 mm at a speed of 2000 frames per second. Development of the system was still at the beginning stage, and the system had not been tested on an LPBF system.

1.2.2 Off-line Systems

In contrast to the in-line metrology systems, the off-line metrology systems are the systems which have an optical path different than the laser beam path. Most of the off-line metrology systems reported to date are camera-based systems where the cameras are placed

outside the machine chamber mainly to avoid possible contamination and damage from fusion splatter.

Furumoto et al. developed an off-line metrology system to investigate the interaction of metal powder and laser, or what they refer to as “the consolidation process”. Figure 1-6 (a) shows a schematic diagram of their experimental setup. A high-speed camera was mounted before a quartz glass window on top of their in-house developed system, monitoring an area of 2 mm ×1.7 mm. With an extra light source (a metal halide lamp), the camera recorded the laser fusion process at a speed of 10,000 frames per second. Figure 1-6 (b) shows the experimental results. The laser powder interaction, particularly the formation of metal balls on a 1-mm thick powder layer, was observed at a speed of 500 frames per second. The impact of powder layer thickness on the metal forming process was also observed.

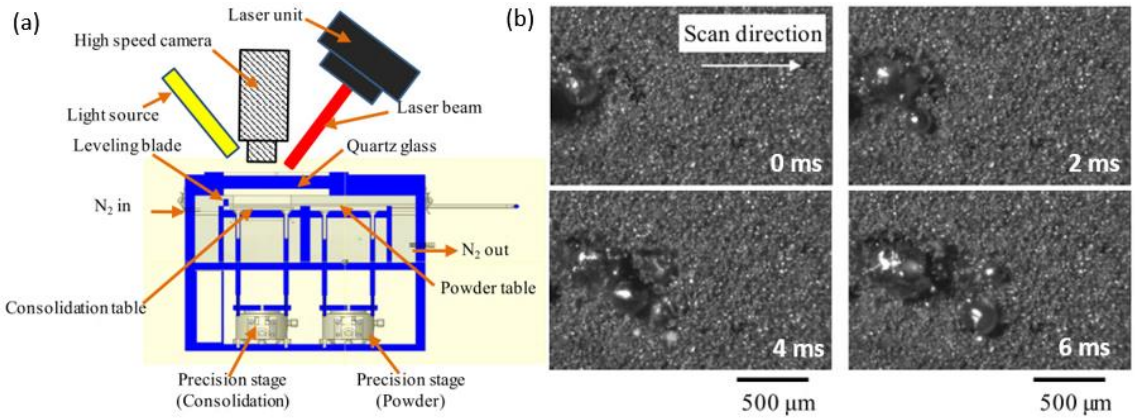

Figure 1-6: Furumoto’s off-line camera system. (a) The schematic diagram of the system. (b) The formation of metal balls on a 1-mm thick powder layer.

An off-line metrology system based on a two-color pyrometer was also investigated by the same research group to detect temperature related signatures [30]. A common limitation of pyrometry is the inability to measure the absolute temperature when the emissivity of the target is unknown [31]. The two-color pyrometry overcame this limitation

by using two sensors, an InAs sensor and an InSb sensor, such that the ratio of the two outputs could be calibrated with respect to a thermal couple (low-temperature range) and the melting points of several metals (high-temperature range). Figure 1-7 (a) shows the experimental setup of the two-color pyrometer on their in-house developed LPBF system. With the two-color pyrometer, the absolute temperature of the melt pool was measured and compared with the melting point of the metal powder to determine whether the powder was melted or sintered (partially melted). An application example is to generate in-process feedback to compensate insufficient laser fusion. To achieve this, the relationship between the melt pool temperature and the laser energy density were measured ahead as shown in Figure 1-7 (b). If the measured temperature was below the melting point, the pyrometer could tell the system to increase the laser energy density to prevent insufficient fusion.

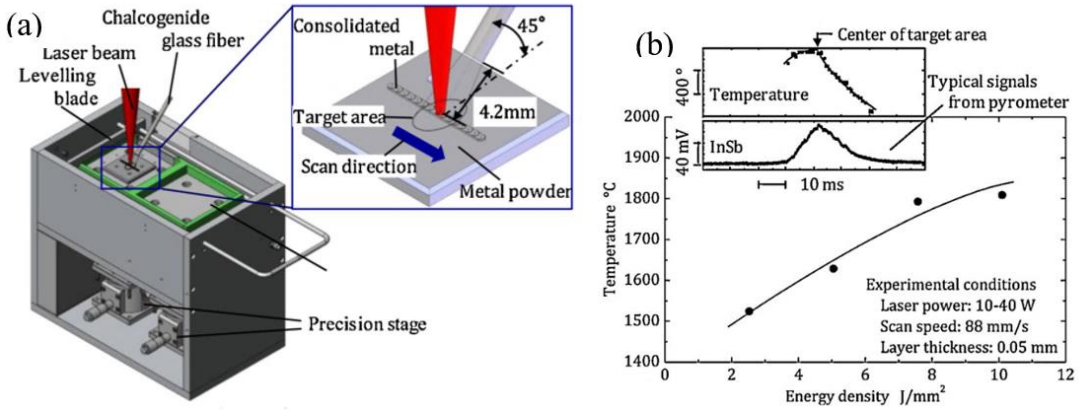

Figure 1-7: Furumoto's two-color pyrometer system installed on an in-house developed LPBF system. (a) An illustration of the system. (b) The calibrated correlation between the melt pool temperature and the laser energy can be used to determine the fusion sufficiency [30].

Another example of an off-line camera setup was reported by Jacobsmuhlen et al. [32]–[34]. A high-resolution camera was used to monitor the build process of the EOSINT M270 machine. The experimental setup is shown in Figure 1-8 (a). The camera was mounted to the chamber side wall through a custom fixture such that the camera could look

through the front window. The viewing angle of the camera was approximately 8°. The small angle minimized the perspective distortion and depth of focus limitation. The high-resolution camera had 6576 × 4384 pixels covering an imaging area of 130 ×114 mm. Lighting was crucial to the success of machine vision imaging. Multiple light sources and reflectors were installed in the machine chamber to facilitate the image capturing. Unlike the high-speed camera, the high-resolution camera could only acquire two images per layer – before fusion and after fusion. Several signatures could be detected on the images, such as the boundary of the fused area, waviness on the powder surface and some surface deformation. Figure 1-8 (b) shows the comparison of surfaces created with the +40% and the -40% hatch distance. Details on the fused powder surfaces could be qualitatively identified at a micrometer level, but online control with the high-resolution images required further research into image processing software and correlation to process parameters.

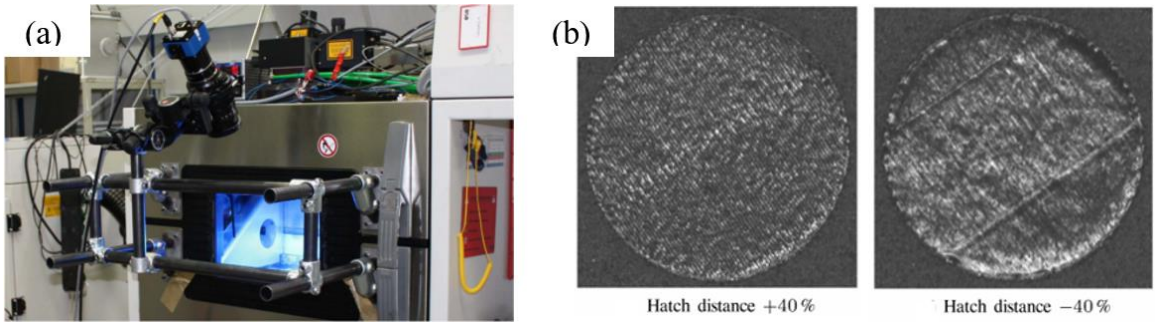

Figure 1-8: High-resolution camera system for in situ measurement of a LBM process [34]. (a) A photograph of the system. (b) The camera sees a clear difference between the fused surfaces with +40% and -40% hatch distance.

Craeghs et al. investigated an off-line camera system where the camera was placed above the powder bed [25]. The experimental setup is shown in Figure 1-9 (a). Three extended light sources were placed inside the chamber to light the powder surface from three different angles. Imaging alone relied on shadowing that was caused by side

illumination in the presence of surface elevation changes and topography variation. Figure 1-9 (b) is an image captured by the off-line camera, showing the trenches on the powder surface caused by a damaged wiper blade.

Krauss, et al. proposed a layer-wise monitoring method to detect the heat distribution with an off-line IR camera [35], [36]. Figure 1-10 (a) shows the experimental setup for the IR camera on the EOSINT M270 system. A germanium glass window was added to the side wall of the machine chamber to protect the IR camera from contamination. The thermal images were captured at a 45° angle with a frame rate of 50 frames per second. The thermal images could be used to detect the drift in some process parameters and the process errors, such as hot spots and insufficient heat dissipation, during the build. Temperature discontinuities were observed on the thermograms and these could indicate a material discontinuity due to the difference in thermal conductivity between the metal and the void. Figure 1-10 (b) is an example of the captured thermal image. The authors argue this effect was an overheating spot caused by a void underneath.

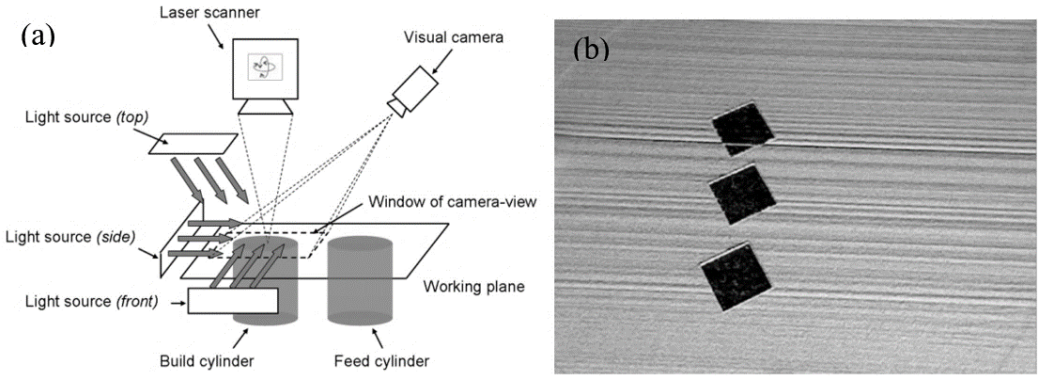

Figure 1-9: Craeghs' off-line camera system. (a) A schematic diagram of the system. (b) A captured image showing line scratches on the powder surface caused by a damaged wiper blade [25].

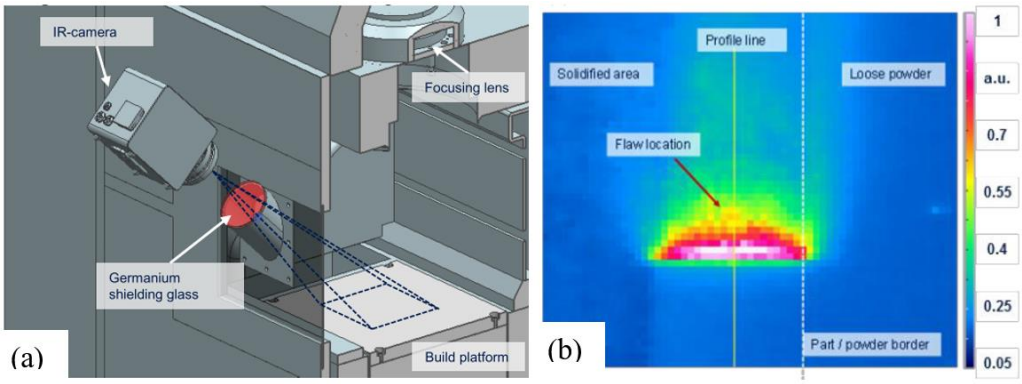

Figure 1-10: Krauss' thermal imaging system. (a) An illustration of the system. (b) A captured temperature profile shows a flaw on the surface [36].

1.3 Motivation for Developing an In situ Fringe Projection System

There are many benefits of measuring surface geometry in situ. Firstly, measurements are most valuable when they are made right after creation of a defect when it is most likely fixable. When the part is completed, the defect will be inside the built and no longer accessible. Secondly, in situ dimensional measurements help us to evaluate final part geometry. AM process can produce complex internal structures, which are challenging and costly to measure ex situ. Instead, in situ measurements can, in principle, be used to reconstruct a whole-body measurement by combining layered measurements. Thirdly, in situ measurements will add to our knowledge, namely physics of the LPBF process, the laser-powder dynamics and more. The knowledge will, in turn, help to improve process parameters which will ultimately lead to better final product quality.

Investigations on in situ surface measurement of LPBF process is limited, presumably because metrology systems with suitable measurement capabilities are not available [37]. A desired metrology system should have the following characteristics: non-contact, a long working distance, and the capability of measuring rough surfaces. Figure 1-11 maps the measurement uncertainty as a function of the part dimension for most optical 3D

measurement instruments. Although modern optical profilers, such as interferometers and confocal microscopes, can produce high-resolution surface measurements, their small measurement area and short working distance (millimeter scale) do not allow for integration into a typical LPBF machine. More importantly, the general measurement specifications, namely a micrometer scale measurement uncertainty over a measurement area on the order of tens of millimeters, are challenging for many measurement approaches. Among all the surface profiling techniques, the fringe projection profilometry is the most viable solution [38]–[40]. Fringe projection profilometry is a well-studied technique for measuring the aerial profile of small- to large-sized objects. The measurement area can be adjusted by changing the optics. In this study, two fringe projection systems are developed to measure form of powder bed surface and texture on fused metal regions.

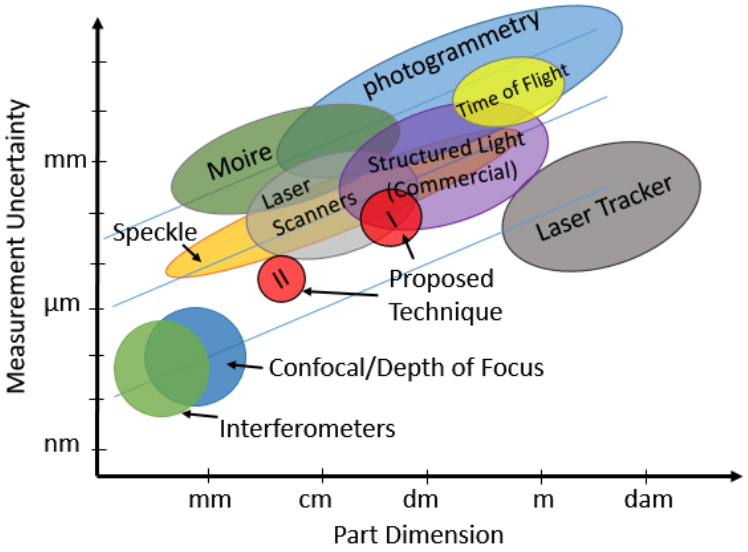

Figure 1-11: Summary of the measurement uncertainty versus part dimension for various optical 3D shape measuring instruments.

Compared to other non-contact surface profilers such as laser scanners, a fringe projection system is much faster because the surface is captured at one shot. A fringe projection system has a long working distance, so it can be mounted far from the powder

bed to avoid interference with the fabrication process. One important motivation for us to develop an in-house fringe projection system is to have full control over the raw data and the image processing software, which is not accessible in a commercial system. Commercial fringe projection systems (also called structured light systems) are available, but they are not ideal for the metal AM application [41]–[45]. They are mostly too big to be integrated into the metal AM system and/or their measurement uncertainty is too large for measuring height features on the size scale of interest, e.g. 50 μm height deviations are expected between the powder and the fused metal region. A few high-end commercial systems meet the uncertainty requirement but are far beyond our budget. For example, the Breuckmann StereoScan Neo has a 5 μm vertical resolution (quote from the specifications) for a 144 × 108 mm measurement area is sold for over 100,000 US dollars [46].

1.4 Outline of Study

This dissertation demonstrates the development of an in situ fringe projection system for an LPBF machine and characterization of the measurement performance of this system. Chapter 2 describes the principles of fringe projection profilometry including the basics of triangulation, phase shifting algorithms, phase unwrapping techniques, and calibration. Chapter 3 demonstrates the development of the in situ fringe projection system. Two setups are developed – one for global surface geometry measurement and the other for detailed surface texture measurements. Some preliminary analysis of in situ measurements is shown to validate the capabilities of the system. Chapter 4 explores characterization of vertical measurement performance through evaluation of the surface topography repeatability and through an intercomparison study with a commercial stylus profilometer. Chapter 5

investigates the applicability and measurement of the instrument transfer function (ITF) to the fringe projection system. The linearity conditions are determined through mathematical analysis and simulation. A practical ITF measurement technique using a stepped surface is demonstrated. Chapter 6 provides a conclusion to this study.

CHAPTER 2: BASIC PRINCIPLES OF FRINGE PROJECTION PROFILOMETRY

In the previous chapter, we discussed the importance of in situ surface measurements of the LPBF process and proposed fringe projection as the most viable solution. In this chapter, we will introduce the basic principles of fringe projection with an emphasis on aspects relevant to design specifications. Section 2.1 gives a brief history of fringe projection. Section 2.2 develops the geometrical principles of the fringe projection system from a triangulation model. Section 2.3 describes the fringe analysis method, followed by the phase unwrapping method in Section 2.4. Section 2.5 presents the calibrations and nonlinearity correction techniques.

2.1 Historical Development and Conventional Uses

Fringe projection profilometry is a surface measuring technique that uses projected sinusoidal or binary fringe patterns to reconstruct the 3D profile of a diffuse surface. Historically, the idea of measuring the surface contour using projected fringes was first proposed by Rowe and Wolford in 1967 [47]. The invention was inspired by the light slit microscope of Schmaltz, where a single slit of light was projected obliquely onto the surface which was viewed normally by a microscope. The limitations of the light slit microscope are 1) only one fringe is used to measure the contour of the surface, and 2) the depth of focus is very small. Rowe and Wolford proposed to replace the single fringe projector with a laser interferometer which can produce a 2D fringe pattern with two plane waves, referred to as an interferogram. The interferogram is equally spaced sinusoidal

fringes which can be used to contour the entire surface area with one shot. Another advantage of this invention was that the system sensitivity, which is mostly determined by the fringe spacing, can be changed by adjusting the angle of the two wavefronts. A large angle creates dense fringes giving higher sensitivity and vice versa. Rowe and Wolford demonstrated the creation of 3-mm fringes with a Wollaston double-image prism setup, and 18-μm fringes with a beam splitter setup [47].

Fringe projection profilometry did not immediately take off as soon as it was invented because analysis of acquired fringe images is slow and challenging. The first breakthrough was made by Takeda in 1982 when he introduced the Fourier transform approach to fringe analysis to extract the underlying phase distribution from a single fringe image [48], [49]. This technique became known as Fourier transform profilometry [50], and it is still widely used today for applications that don't require high spatial resolution. With this breakthrough, fringe projection techniques developed dramatically, and the studies began to divide into specific areas. These research areas are: design of fringe patterns [51]–[54], fringe analysis [43], [44], [55]–[58], phase unwrapping [59]–[64], calibration [65]–[70], and reduction of phase errors [71]–[80].

Conventional applications of fringe projection profilometry measure the 3D profile of mid- to large-sized objects such as the human face[81], the human body [45] and the aircraft/automobile body [82], [83]. If the optics are properly chosen, a fringe projection system can also be used to measure a small-sized object with small height variations such as solder pastes [84], [85] and surface roughness [38], [86], suggesting its feasibility for in situ measurements of surfaces produced by the LPBF process. It is a versatile method that can be used to inspect newly spread powder surfaces (mid-sized measurements) as well as

texture of fused metal surfaces (small-sized measurements). Examples of the measurements are given in Chapter 3.

2.2 Triangulation

An intuitive way to understand fringe projection profilometry is to look at how straight lines on a surface appear bent when viewed at an angle. Figure 2-1 shows distorted fringes (a sinusoidal irradiance pattern) on the metal powder (Inconel 625) surface created by obliquely projected fringes. Notice the fringes are bent because of the viewing angle and the surface height variations. The underlying phase distribution of the sinusoidal fringes can be retrieved using fringe analysis techniques, and the height distribution of the surface can be calculated by a system calibration. Details of these procedures will be discussed in later sections.

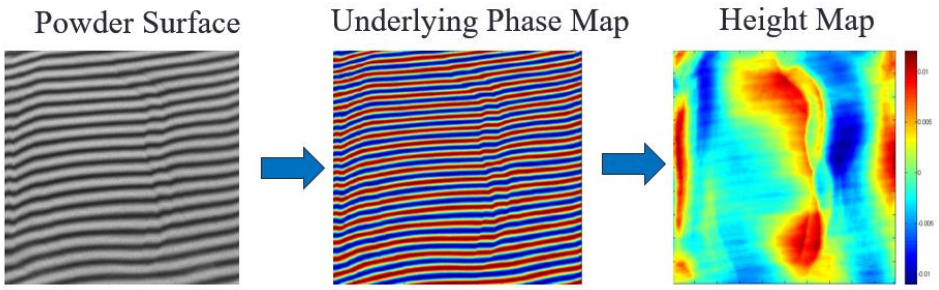

Figure 2-1: Surface reconstruction procedure of fringe projection profilometry.

Triangulation is the fundamental principle in fringe projection profilometry. Triangulation allows the height of the object to be retrieved relative to a reference plane. Triangulation is a geometry measurement technique that uses the relations of similar triangles to calculate the distance from the measured points to the imaging system. Figure 2-2 illustrates the application of triangulation to fringe projection. The profile of an object

is measured with respect to the reference plane which is perpendicular to the optical axis of the camera. Consider a ray (or a fringe), PA, from the projector incident at point A on the reference plane. If an object is placed on the reference plane, the ray PA will, instead, intersect at the point O, meaning the ray will be observed at a lateral position shifted by Δx. The vertical height of the object at point O can be measured by measuring the fringe shift on the reference plane, Δx. Since the triangles ΔOPC and ΔOAB are similar triangles, the following relationship can be established:

$$\frac{d-z}{z} = \frac{l}{\Delta x}, \tag{2-1}$$

where d is the distance from the reference plane to the projector-camera plane, z is the height of the object, l is the distance between the projector and the camera, and Δx is the fringe shift on the reference plane. This equation can also be reformulated as

$$z = \left(\frac{\Delta x}{l + \Delta x}\right) d\,. \tag{2-2}$$

When the amount of phase shift on the reference plane is much smaller than the distance between the camera and the projector ($\Delta x << l$), the relationship between the object height and the fringe shift can be simplified to a linear form, namely

$$z = \frac{d}{l}\Delta x\,. \tag{2-3}$$

It is also easy to know the sinusoidal fringe shift as a function of fringe pitch, p, and the phase shift, $\Delta\varphi$, that is

$$\frac{\Delta x}{p} = \frac{\Delta\varphi}{2\pi}\,. \tag{2-4}$$

Combining the last two equations, the height of the object can be written as

$$z = \frac{1}{2\pi} \cdot \frac{p \cdot d}{l} \Delta\varphi \, . \tag{2-5}$$

We call the term after *1/2π* and before the phase shift, *Δφ*, the effective wavelength, and it is written as

$$\lambda_{eff} = \frac{p \cdot d}{l} \, . \tag{2-6}$$

The effective wavelength is a measure of the sensitivity of a fringe projection system. A smaller effective wavelength yields a higher sensitivity. Because effective wavelength is a function of the fringe pitch, *p*, and the projection angle, *θ* (*tanθ =l/d*), the key to improving the system sensitivity is to decrease the fringe pitch or/and to increase the projection angle. Choosing the proper effective wavelength for measuring different surface height variations is an important design for a system, and it will be discussed in detail in Chapter 3.

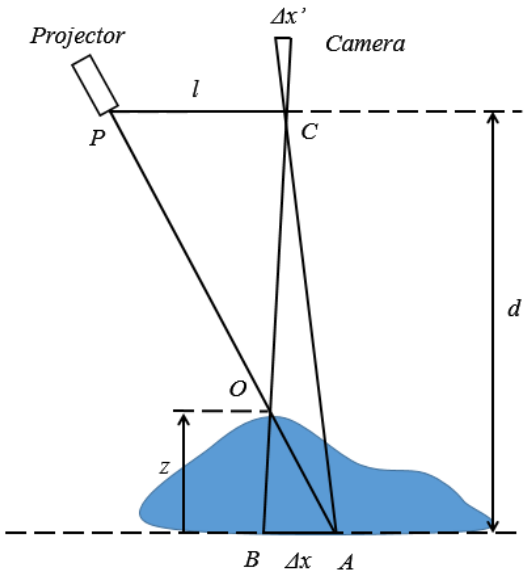

Figure 2-2: Geometry of a fringe projection system.

Figure 2-3 shows the operational procedures for the fringe projection system. Before taking the measurements, the system is calibrated. Three calibrations steps are required.

The first step is the effective wavelength calibration. This step establishes the relationship between the phase shift and the relative height of the object. The second step is the lateral calibration. This step calculates the conversion factors to convert pixels to millimeters. The last step is the nonlinearity correction which linearizes the projector/camera irradiance response. This step reduces the harmonic noise on the measurements. A measurement starts with projecting a sequence of sinusoidal fringe images onto the surface to be measured. Images of the surface are captured at an angle and processed through a phase shifting algorithm to obtain the wrapped phase map. Then a reference-guided phase unwrapping algorithm is used to unwrap the wrapped phase maps. Next, the carrier phase map is removed from the unwrapped phase map with filtering based on lower-order Legendre polynomials. An optional Fourier filter is used at this point to further remove residual harmonic noise from the phase maps. Lastly, the phase map is converted to the height map using the vertical and lateral calibration results. These steps are discussed in detail below.

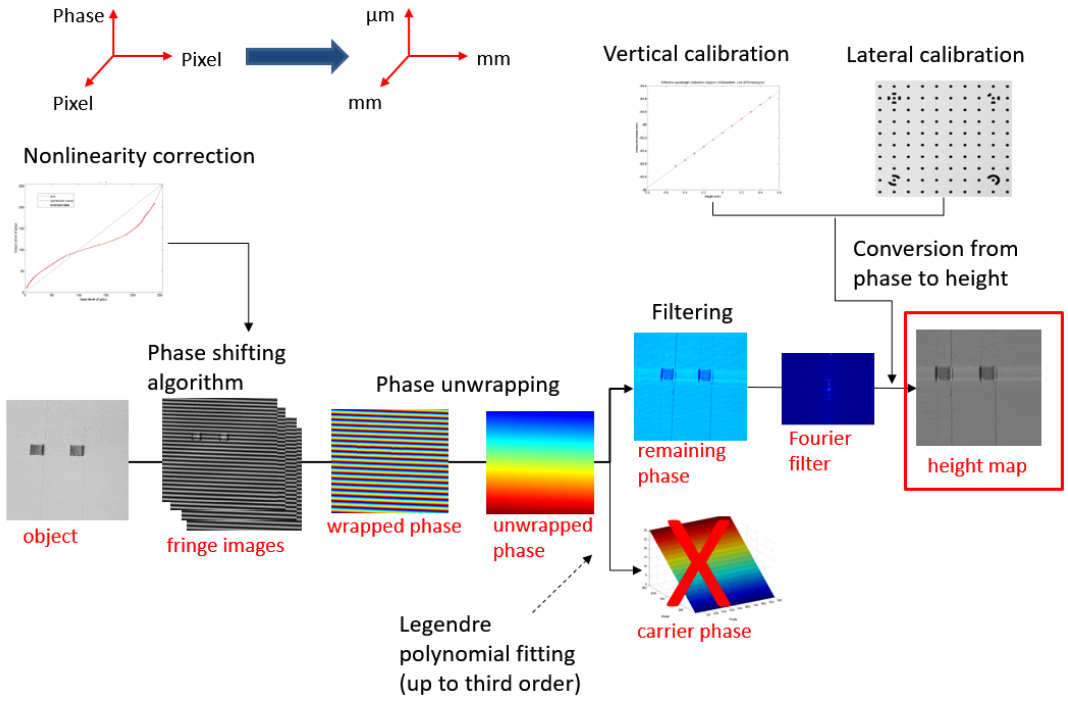

Figure 2-3: Measurement and calibration procedures.

2.3 Fringe Analysis

The fringe analysis is the process of calculating the underlying phase distribution by acquiring and processing a series of systematically phase-shifted fringe images. The performance of a fringe projection system is greatly affected by the fringe analysis method. There are many fringe analysis methods, and they can be divided into two main categories – spatial fringe analysis methods and temporal fringe analysis methods.

Spatial fringe analysis techniques calculate the phase distribution of the projected fringe pattern by analyzing the spatial distribution of the fringes within one image. The success and efficiency of the techniques require a carrier frequency (projected fringe spatial frequency) much higher than the spatial frequency content of the object to be measured. Two of the most famous spatial fringe analysis methods are the Fourier transform method [49], [50] and the spatial phase detection method [87]. The Fourier transform method derives the wrapped phase map of the object by shifting one of the carrier peaks to the center of the image in the Fourier domain, effectively removing the carrier frequency from the data. The retrieved phase is the inverse Fourier transform of the filtered Fourier spectrum. The spatial phase detection method calculates the wrapped phase map by sinusoidally fitting the fringe pattern with the phase detection algorithm similar to that used in communication techniques. The retrieved phase is approximately the ratio of a sine-wave integral of the fringe image to a cosine-wave integral of the fringe image. Both methods are limited to measuring a smooth surface with slowly varying height features. Because the fused metal surface is usually rough with many high spatial frequency details, these techniques are not suitable for this application.

Temporal fringe analysis techniques, also called the phase shifting/stepping algorithms, calculate the phase map from a sequence of temporally shifted fringe patterns. Quality of the resulting phase maps is largely affected by the number of phase-shifted images - the more images taken, the better the quality of the phase map. The biggest advantage over spatial fringe analysis methods is that spatial resolution can be as high as the camera resolution. The cut-off spatial frequency is usually limited by the equivalent noise floor and the MTF of the camera [88]. For these reasons, the phase-shifting fringe analysis technique is used for our in situ fringe projection system.

The least-squares phase shifting algorithm is the most widely adopted and most well studied temporal fringe analysis method. It uses *N* frames of sinusoidal images; each frame has an initial phase that is shifted *2π/N* from the previous frame. One advantage of this algorithm is to reduce phase error by increasing the number of acquired fringe images. The irradiance distribution of each fringe pattern is expressed as

$$I_i(x,y) = I_b + I_m \cos\left(\frac{2\pi x}{p} + \delta_i\right), \tag{2-7}$$

where *i* indicates the ith frame, I_b is the irradiance bias, I_m is the irradiance modulation, p is the period of the sine wave, and δ is the step size which is given by

$$\delta_i = \frac{i-1}{N} 2\pi, \qquad i = 1, \dots, N. \tag{2-8}$$

The wrapped phase map is obtained by applying the phase shifting algorithm. The wrapped phase map is written as [89]

$$\phi(x,y) = arctan\left(\frac{-\sum_{i=1}^{N} \sin(\delta_i) I_i(x,y)}{\sum_{i=1}^{N} \cos(\delta_i) I_i(x,y)}\right). \tag{2-9}$$

2.4 Phase Unwrapping

In the real computation process, the four-quadrant inverse tangent function in Matlab, *atan2(Y, X)*, is used to remove the ambiguity of sign of numerator and denominator in the *arctan(Y/X)* function. The result of the *atan2* function is limited to the range [-π, π], but the real phase of the sine wave is continuous. Thus, a phase unwrapping procedure is needed to expand the wrapped phase from [-π, π] to an extended range.

The simplest phase unwrapping algorithm (Itoh, 1982) is to unfold all the phase jumps bigger than π along rows and columns respectively [63]. This technique is fast and straightforward but susceptible to noise in a wrapped phase map. More advanced phase unwrapping algorithms, such as the quality-guided phase unwrapping algorithm, use the modulation of the fringe images as a "quality map" to decide the unwrapping paths [61]. This algorithm is robust but time-consuming. In our application, the rough metal surfaces lead to noise in the wrapped phase maps and this is our main challenge of phase unwrapping. Two major noise sources cause unwrapping failure. One is saturation that results from high reflectance of metal, and the other is shadowing caused by anisotropic texture of fused metal surfaces.

We tested the Itoh unwrapping algorithm and found that it works with the wrapped phase maps of the powder surfaces, but many unwrapping errors occur for the wrapped phase maps that contain fused metal regions. To cope with this problem, we introduce what we call a reference-guided phase unwrapping algorithm. This algorithm uses the reference phase map obtained from the first powder layer to unwrap the other wrapped phase maps. The conventional unwrapping algorithm is used for the unwrapping of the first powder layer. We then fit this unwrapped phase map to Legendre polynomials (up to the third

order) and this polynomial fit becomes the unwrapped reference phase map used in the unwrapping algorithm for all subsequent measurements. The algorithm can be mathematically expressed as

$$\varphi_u(x,y) = \varphi_r(x,y) + 2\pi \cdot Round\left(\frac{\varphi_{ref}(x,y) - \varphi_r(x,y)}{2\pi}\right), \quad (2\text{-}10)$$

where $\varphi_u(x,y)$ is the unwrapped phase, $\varphi_r(x,y)$ is the wrapped phase, $\varphi_{ref}(x,y)$ is the reference map, and the operator "*Round( )*" means rounding to the nearest integer. This method is valid because all the measurements are taken at around the same height level, and the height variation of the surface is relatively small (less than a half of the effective wavelength). The primary advantages of this algorithm are 1) it is very fast because the unwrapping is path independent, and 2) the phase unwrapping is achieved at each pixel such that unwrapping errors will not propagate along the pixel arrays.

The unwrapped phase map contains both the object phase and the carrier phase. The carrier phase is a chirped sinusoidal wave, where the chirping is a result of the camera-projection angle. To estimate the carrier phase, simply fit the unwrapped phase map to Legendre polynomials (up to third order is sufficient). Then subtracting the carrier phase from the unwrapped phase map will give the object phase map.

2.5 Calibrations

Calibration is a procedure of establishing the conversion from unwrapped phase map to height map of an object. There are many fringe projection calibration techniques, and they can be divided into two main categories. The first category combines photogrammetry principles with fringe projection [42], [65], [70], [90], [91], and the second category is the

least-squares calibration approach. The photogrammetry calibration method requires a conventional camera calibration procedure from the field of photogrammetry where internal and external parameters of the camera can be solved through a bundle adjustment approach [92]. Calibration of the projector follows a similar process where the project is regarded as an “inverse camera” [93]. A calibration grid is used to correlate the phase distribution of the project fringes to the global coordinates of the grid. The least-squares calibration approach establishes the conversions for the X, Y and Z dimensions separately. The X and Y conversion is achieved with a calibration grid. The grid distance is calibrated with a ball-probe CMM or an optical CMM. The conversion factors (from pixel to millimeter) are calculated at a reference plane. The Z calibration is complicated because the relationship between phase and height is nonlinear, meaning more than two unknown coefficients are in the nonlinear equation of phase and height. The nonlinear equations are usually established through measurements of calibrated gauge blocks or a precision linear translation stage. Then a least-squares approach, such as the Levenberg-Marquardt algorithm [94], is used to solve for the unknown coefficients [67], [68], [95], [96].

The calibration method used for our fringe projection system falls in the second category. It combines the effective wavelength calibration for height [97] with a standard machine vision calibration for XY coordinates. The conversion matrices in the lateral and vertical directions are obtained separately. The effective wavelength calibration converts a phase value at each pixel to a height value. The machine vision calibration converts the height map from a camera pixel space to metered XY coordinates.

2.5 1 Effective Wavelength Calibration

Effective wavelength is the scale factor that converts an unwrapped phase map to a height map. It is defined as the height change when the fringe is shifted one cycle and has a unit of mm/cycle. The mathematical expression of the effective wavelength is written as

$$\lambda_{eff} = \frac{2\pi}{\Delta\phi/\Delta h}, \tag{2-11}$$

where $\Delta\phi$ is the phase shift and Δh is the corresponding height change. The height map is obtained by multiplying the effective wavelength map with the object phase map, namely

$$z(x,y) = \frac{\lambda_{eff}(x,y)}{2\pi} \cdot \phi(x,y). \tag{2-12}$$

The effective wavelength is directly related to the system geometry. From the geometry given in Figure 2-2, the projection angle, θ, can be defined as

$$tan\theta = \frac{l}{d}. \tag{2-13}$$

Therefore, the effective wavelength can also be written as

$$\lambda_{eff} = \frac{p}{tan\theta}, \tag{2-14}$$

where p is the fringe pitch. Determining the effective wavelength accurately through the geometric layout of the system is not possible. Equation 2-14 shows that the effective wavelength directly depends on the fringe pitch and the projection angle. For example, assume a 10° projection angle which gives an effective wavelength of 5.7p. If the projection angle is inaccurately measured as 11°, the effective wavelength will be 5.1p. That is over 9% discrepancy in λ_{eff} for a 1° angular error. In practice, the projection angle is very difficult to accurately measure, so relying on knowledge of this angle – the

geometric layout of the system – for calibration leads to significant errors. An alternative calibration method must be used to determine the effective wavelength.

Conventionally, the effective wavelength is evaluated by moving the stage vertically while counting the number of fringes passing a reference line for several cycles. This method calibrates the effective wavelength as one number for the entire measurement region. This is reasonable when the projected fringes are equally spaced, such as those generated by a telecentric projection system. A single effective wavelength is mostly used when the measurement uncertainty requirements are not very strict. However, when measuring small height variations with low uncertainty requirements, such as the laser fused powder surfaces, it is necessary to consider the variation of effective wavelength over the measurement area. Therefore, the wavelength must be computed and used for each pixel.

The ideal artifact for the effective wavelength calibration is a diffuse flat plate. Diffuseness ensures a high signal-to-noise ratio for the projected fringes, and flatness ensures well-defined upper and lower calibration boundaries. We tested many surface samples to select our calibration surface including a white cardboard, a ground glass (Edmund Optics Grit ground glass diffuser), a sand-blasted aluminum plate and a spray-painted float glass. A white cardboard has a perfect diffuse surface, but not enough flatness. The ground glass has a diffuse surface but not enough surface scattering; a great portion of light transmits through the glass and is reflected from the second surface interfering the measurement. The sanded aluminum plate also has a diffuse surface, but the surface appears sparkling (shiny at sparse spots) because of free electrons in metal that vibrate, stop and re-emit light. Among all the tested surfaces, we found a thin layer of developer

coating (Spotcheck SKD-S2 Aerosol, Part No. 01-5352-77) on an optically flat surface, e.g. float glass, provides the best diffuse flat surface for calibration.

The effective wavelength is measured by moving a vertical stage over a calibration range; for our system, this range is -0.5 mm to 0.5 mm in increments of 0.1 mm. The unwrapped phase map is obtained at the 11 height positions. To reduce the calibration uncertainty, the unwrapped phase maps are measured 10 times at each height position. The mean phase values are fit to a straight line at each pixel using the least squares method [98], and the slope of each fitted line is used to calculate the effective wavelength. The effective wavelength equals to 2π divided by the slope. Figure 2-4 shows the plot of phase versus stage height at the center pixel with error bars indicating the standard uncertainty of the mean. The plot confirms the linear relationship between phase and height within a small height range. The slope of the line in the graph is found to be 1.60 rad/mm, resulting in the effective wavelength of $2\pi/1.60 = 3.92$ mm/cycle. This calculation process is carried out at each individual pixel in the field of view, and the distribution of the effective wavelength is shown in Figure 2-5. The effective wavelength map contains a tilted slope caused by the varying fringe pitch and the varying projection angle. The variation of the effective wavelength across the field of view is approximately 0.09 mm/cycle.

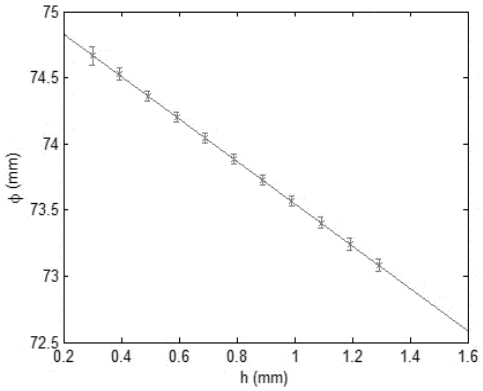

Figure 2-4: The unwrapped phase versus relative height at the center pixel.

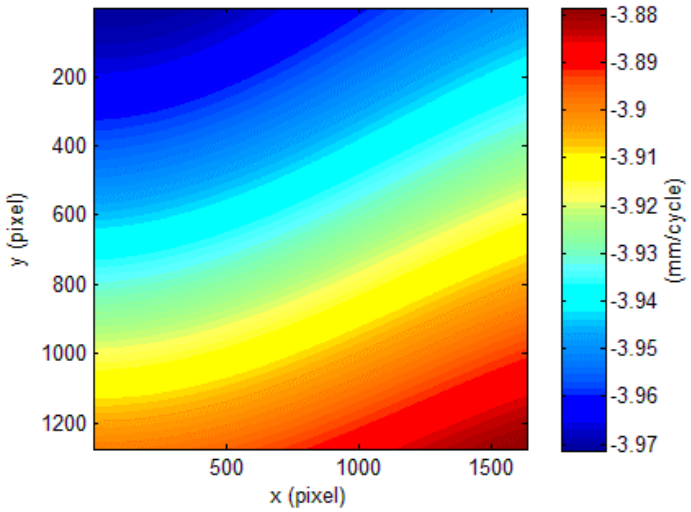

Figure 2-5: The effective wavelength map.

2.5.2 Lateral Calibration

Lateral calibration is the process of converting the height map from a pixel space to a XY metered space using a machine vision technique. This is achieved by imaging a calibration grid at the nominal zero height position. The size of the grid depends on the required measurement region. We have developed two grid artifacts for the calibration of a large measurement area (150 × 150 mm) with a lateral sampling interval of 60 μm and a small measurement area (28 × 15 mm) with a lateral sampling interval of 6.8 μm. The two grid artifacts are shown in Figure 2-6.

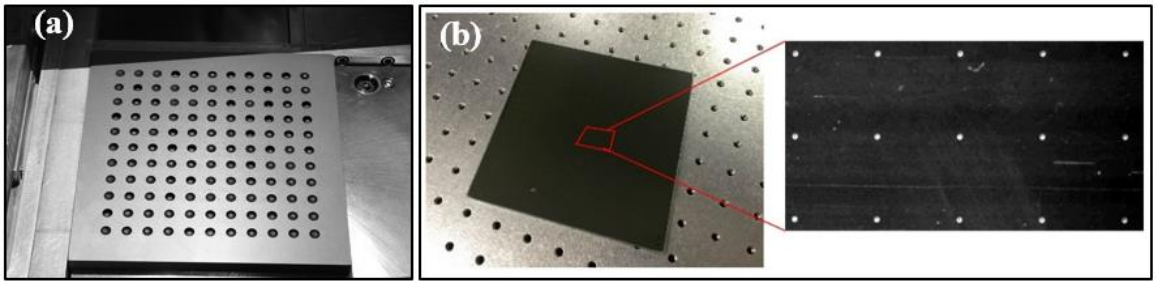

Figure 2-6: Lateral calibration artifacts: (a) 11×11 with 15-mm pitch and (b) 5×3 with 6.5-mm pitch.

The grid plate for global area calibration is made with a 200 × 200 mm aluminum plate. It contains an 11 × 11 grid of reamed holes of nominally constant 15 mm pitch, covering an area of 150 × 150 mm. The reamed holes are measured with a CMM to calibrate the position of each hole; this measurement and its uncertainty are used as a reference for the lateral pixel-to-millimeter conversion. Then the holes are filled with black epoxy for enhanced contrast for imaging. The grid plate for local area calibration is made from an aluminum glass mirror, where the back of the mirror is coated with a layer of protective black paint. A grid of dots with a nominal pitch of 6.5 mm is created with the laser scanner from an LPBF machine. The high-power laser removes the topical paint layer and the aluminum layer uncovering the highly reflective glass surface. The position of each dot is measured with an optical CMM. The measurement and the uncertainty are used as a reference for the lateral conversion.

To calculate the lateral scaling factors, the images of the grid plate are first acquired with the grid plate at the nominal zero height level where laser fuses powder. Then the centers of the holes are extracted using standard least-square circle fit method. The four corner coordinates and their CMM measured coordinates are used to construct a projective transformation matrix,

$$T = \begin{bmatrix} a_{11} & a_{12} & a_{13} \\ a_{21} & a_{22} & a_{23} \\ a_{31} & a_{32} & a_{33} \end{bmatrix}. \tag{2-15}$$

This matrix describes the position and orientation of the camera. By multiplying each pixel location (u, v) with the matrix, the perspective distortion caused by the camera viewing angle is removed. The new pixel space coordinates are given by [99]

$$[x'y'w'] = [u\ v\ 1] \cdot T\ , \tag{2-16}$$

where (x'/w', y'/w') are the coordinates in the normalized planar object space. The transformation matrix derived above is saved and used to remove the perspective distortion from all future images under the assumption that the system is geometrically stable. The transformation matrix can also be applied to the grid plate image to correct the perspective distortion. The original image of the grid plate and the image after perspective correction is shown in Figure 2-7.

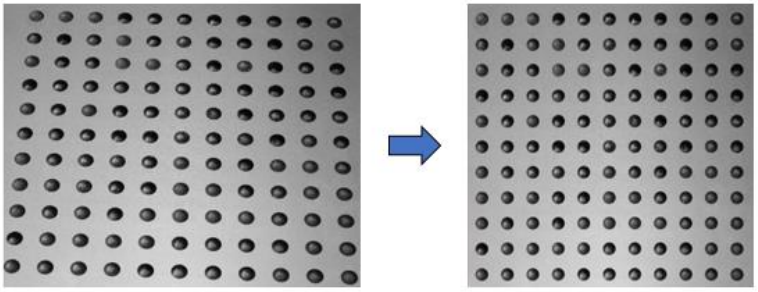

Figure 2-7: Transformation of calibration grid from camera coordinates to world coordinates through a projective transformation.

After using the projective transformation to remove the perspective distortion, the relative locations of the hole centers in the transformed images are compared with those measured by the CMM. The ratio of the two locations gives a conversion factor from pixel to millimeter for each hole center. The ratios between the hole centers are determined using a bilinear interpolation method. The conversion factor for each pixel is defined as

$$s_x = \frac{x_{ref}}{u_N}, \qquad s_y = \frac{y_{ref}}{v_N} \quad \left(\frac{mm}{pixel}\right), \tag{2-17}$$

where (x_{ref}, y_{ref}) is the location of the reference grid measured by the CMM, and (u_N, v_N) is the location of each hole in pixels in normalized object space. Finally, the height map is converted from a pixel space to a metered space by multiplying the scaling factor, (s_x, s_y), with the height map in normalized object space, that is

$$[x\ y] = \begin{bmatrix} s_x \\ s_y \end{bmatrix} \cdot \left[\frac{x'}{w'}, \frac{y'}{w'}\right] \quad (mm). \tag{2-18}$$

2.5.3 Nonlinearity Correction

The projector-camera pair is intrinsically a nonlinear system. The irradiance detected by the camera is usually not proportional to the irradiance projected by the projector. This means a projected sinusoidal irradiance pattern is viewed by the camera as a distorted sinusoidal pattern. The distortion implies the presence of harmonics in the sinusoidal irradiance pattern. The consequence is the height maps also contain harmonics.

Correction of nonlinearity requires measurement of a responsive curve – the curve of detected irradiance as a function of projected irradiance. We projected a series of uniform irradiance patterns on a spray-painted float glass (as the calibrated surface). The camera has 8-bit digitized outputs with a dynamic range of 256 gray levels, but a practical range for nonlinearity correction is [10, 200] since not all gray levels will be used. Another practical consideration is the uniformity of the irradiance pattern. The acquired irradiance is not uniform within the measurement area; therefore, an area of 10 × 10 pixels in the center of the measurement region is selected and the average irradiance in this region is used for calibration. To reduce the calibration uncertainty, ten measurements are made and the average of the ten measurements is used for calibration. Figure 2-8 (a) shows the responsive curve measurement -- the irradiance detected by the camera as a function of the irradiance projected by the projector. The standard uncertainty of the mean irradiance is also shown in the graph. To correct nonlinearity, we constructed an inverse function to modify the projected irradiance such that the irradiance detected by the camera is linear to

the modified irradiance. The inverse function is a polynomial derived from fitting of the inverse curve. The inverse curve is symmetrical with the responsive curve about the straight line of y=x. Figure 2-8 (b) shows the inverse curve and the polynomial fitting.

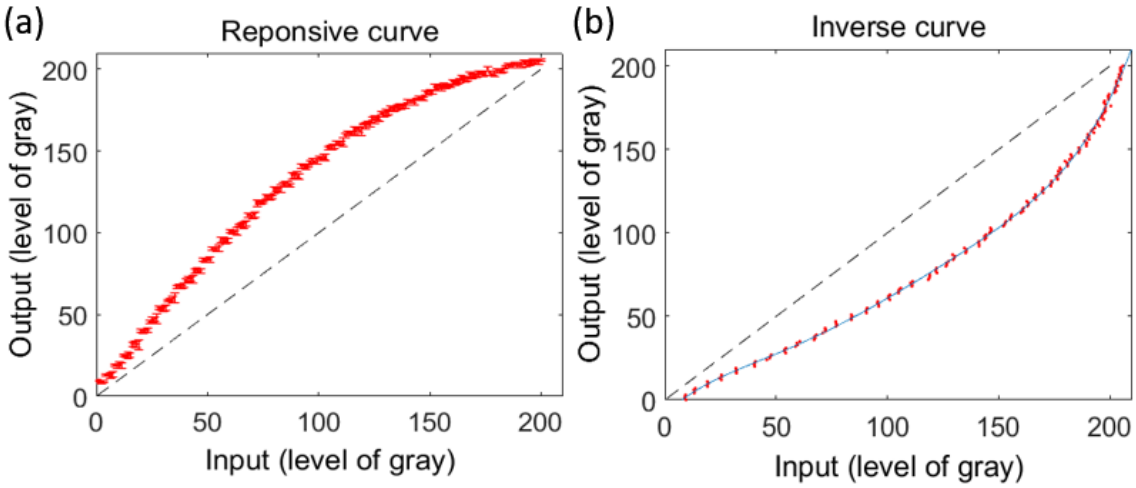

Figure 2-8: Correcting the nonlinearity of a projector-camera pair: (a) Natural response of the projector-camera pair and (b) the inverse function for correcting the nonlinearity.

After we obtained the inverse function, we measured the responsive curve again to check the result of the nonlinearity correction. We checked the irradiance detected at five different locations in the measurement region. They are the pixels at the center and the four corners of the images. The response curves at these pixels are shown in Figure 2-9. Since linearity is calibrated at the center area, the response curve at the center pixel follows the relationship of y=x. The response curves at the corner pixels are also linear but have slightly different slopes. It is worth mentioning that the system is linear across the field view even though the response curve is different at different locations. In fact, we only need the responsive curve at each pixel to be linear because the object phase is retrieved independently at each pixel.

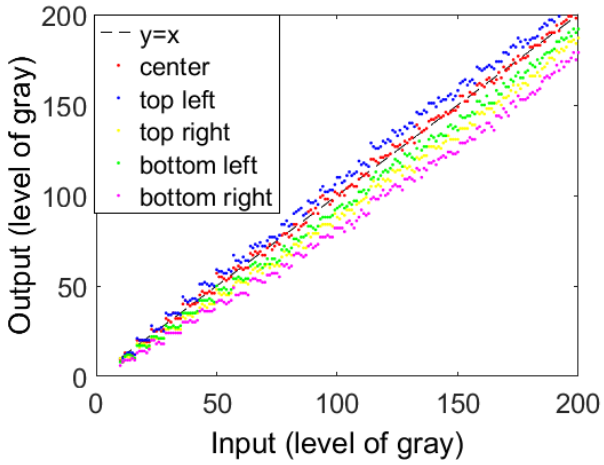

Figure 2-9: The corrected response curves at center and corner pixels.

The linearization process should remove the harmonics in the sinusoidal fringe pattern, meaning the fringe pattern should be a pure sine wave. We can prove this by evaluating the Fourier spectrum of a slice of the sinusoidal fringe pattern. Figure 2-10 compares the Fourier spectra of a slice of the fringe pattern before and after the nonlinearity correction. A peak related to the 2nd harmonic appears in the Fourier spectrum of the noncorrected fringe pattern. In contrast, the Fourier spectrum of the corrected sinusoidal fringe does not have the 2nd order harmonic peak.

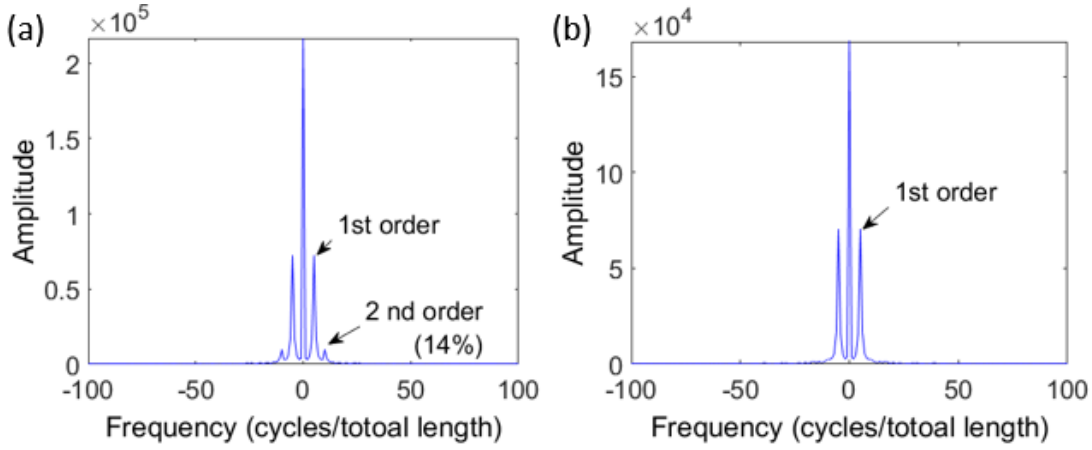

Figure 2-10: Fourier spectra of sinusoidal fringes before (a) and after (b) nonlinearity correction.

CHAPTER 3: DEVELOPMENT AND TESTING OF A FRINGE PROJECTION SYSTEM FOR THE LPBF PROCESS

In the previous chapter, we established the basic principles of fringe projection profilometry with an emphasis on selection of the appropriate fringe analysis, phase unwrapping, and calibration techniques. In this chapter, we will describe the selection of the appropriate hardware and the development of the system geometry based on the LPBF machine chamber. We will discuss the design of two fringe projection systems – one for global surface geometry measurements and the other for detailed surface texture measurements.

3.1 In situ Global Powder Bed Measurements

The LPBF machine under investigation is designed and made at Edison Welding Institute, Ohio. It is designed as an open-architecture system for testing various in-process sensors which can benefit improvement of the LPBF process. The machine chamber is approximately 1016 mm wide, 477 mm tall and 532 mm deep. The primary components of the machine include a scanner head for melting the powder, a build platform for supporting the build, a powder reservoir for holding the powder and a recoating arm for dispensing the powder (see Figure 3-1). The size of the build platform is 256×256 mm^2, and the laser scanning region (the building area) is a 150×150 mm^2 square region to the top left corner of the platform. This region is the full-field measurement region for the fringe projection system.

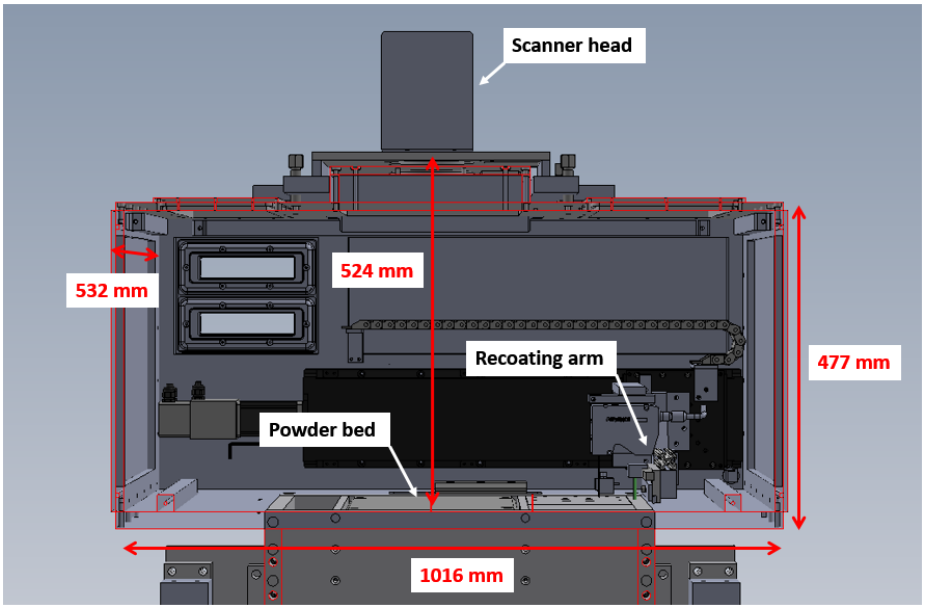

Figure 3-1: Primary components and length scale of the LPBF machine.

3.1.1 Selection of Hardware

A challenge to realize in situ metrology for the LPBF process is that the instrument must be incorporated into the LPBF machine and not interfere with the LPBF process. This means the metrology system must be compact and preferably mounted outside the machine chamber to avoid contamination from powder dust and fusion splatters. One of the main components of a fringe projection system is a projector that can generate phase-shifted fringe patterns. A digital-light-processing (DLP) projector will provide such a functionality. A desired projector should have an image size close to the 150 ×150 mm^2 printing area at approximately 524 mm. To select the correct projector, we need to find the desired throw ratio. The throw ratio is defined as the ratio of the projection distance to the image width. A desired throw ratio based on the chamber geometry is 524 mm / 267 mm =2.0 (assuming the aspect ratio is 16:9). However, such a projector doesn't exist on the market. We chose the Vivitek Qumi Q5 projector with a throw ratio of 1.55, which

generates a projected image size approximately 340 × 210 mm^2. The native resolution of the projector is 1280 × 800 pixels, giving a pixel footprint of 0.3 mm/pixel. The minimum projection distance is 0.7 meter which is longer than the desired projection distance, approximately 0.5 meter, when it is mounted outside the chamber. The projected fringe pattern is slightly defocused, but this does not affect the measurements because a slight defocus does not create distortion of the sinusoidal fringe pattern [73].

For image acquisition, we choose commercial digital single-lens-reflection (DSLR) cameras over scientific cameras for two reasons. Firstly, commercial DSLR cameras have a much higher pixels number than scientific cameras. This is beneficial because having more pixels means having more data points in the measurements. Secondly, commercial DSLR cameras use larger pixels than scientific cameras. This design reduces the cost of the camera and generate better image quality (lower noise). Scientific cameras use smaller pixels to achieve a higher sampling rate close to, and sometimes better than, the optical diffraction limit because they are mostly used for applications such as high-resolution (meaning high spatial frequency cut-off) imaging. However, this quality is not important for the fringe projection application.

To choose the appropriate camera lens, we need to calculate for the effective focal length which can produce the desired measurement field, i.e. the 150 × 150 mm^2 printing area. The effective focal length is a function of magnification and the object distance expressed as

$$f_E = \frac{m \cdot z}{1 - m}\,, \tag{3-1}$$

where f_E is the effective focal length, z is the distance from the object to the camera, and m is the magnification. The magnification can be calculated as the camera sensor size divided

by the desired measurement field. The camera sensor size is 22.3 × 14.9 mm^2, and the desired measurement field is 225 × 150 mm^2, leading to a magnification of -4.9/150 = -0.10. Assuming the object distance is 600 mm, the desired effective focal length is 0.1×600/(1+0.1) = 55 mm.

3.1.2 System Geometry

Figure 3-2 shows the fringe projection system mounted on the LPBF machine. The projector is placed on top of the chamber illuminating the powder bed through a glass window onto the targeted measurement region. Three DSLR cameras (Canon T3i) with standard zoom lenses (Canon EF-S 18-55mm f/3.5-5.6) are used to capture the images of the powder bed at different viewing angles. The focal length of the three lenses are set to 55 mm. The optical axis of camera A is approximately 35° with respect to the vertical direction, and the angles of camera B and C are approximately 38°. The camera lenses are adjusted to focus on the build platform at a nominal build height, then epoxy glue is applied onto the lens rims to secure the focus. The camera lenses are connected to the machine chamber through three custom-made chimney pipe connectors (not shown in the figure). The lens connectors ensure a sealed chamber enclosure because the laser powder bed fusion process must be carried out in an argon environment to minimize metal oxidation during the fusion process.

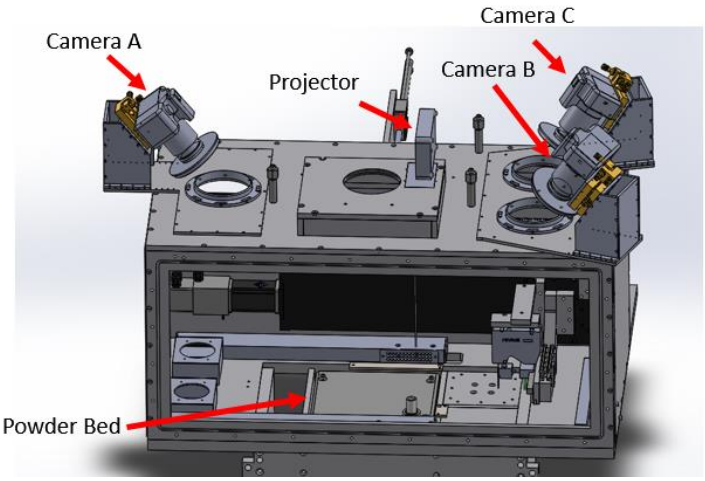

Figure 3-2: The LPBF machine with the fringe projection system installed for global powder surface measurement.

To check the field of view, the projector illuminates a uniform pattern on the build platform, and the powder bed is observed from the cameras. Figure 3-3 shows an image of the powder bed taken from Camera A. A 160 × 160 mm^2 build plate (steel) is mounted on the build platform. The powder is only spread on the left side of the build plate where the building takes place. The calibrated measurement region is the 120 × 120 mm^2 square outlined in red. The images captured at an angle have a key-stoning effect, and a projective transformation is used to remove the key-stoning. This image shows one layer of our test builds, which are ten 10-mm square pillars fused with different process parameters and a 10-mm dome.

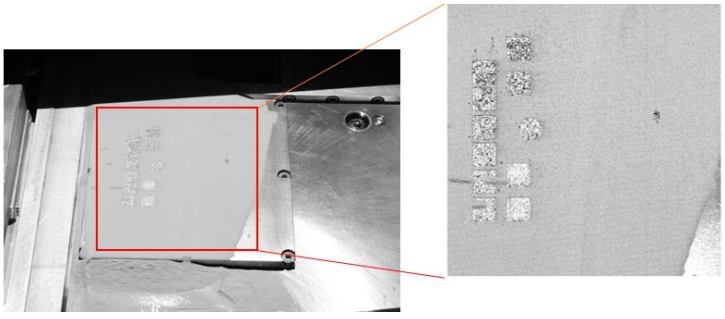

Figure 3-3: An image of the powder bed taken by Camera A (left) and the monitored region after projective transformation (right).

Printing on a layer of powder takes three steps, and a measurement is taken at each step (Figure 3-4). The first measurement is taken after the recoating arm spreads a layer of powder over the build platform. This measures the evenness of the newly spread powder layer prior to laser fusion. The second measurement is taken after a high-power laser beam fuses a selected region in the powder. This measurement examines the boundary and the surface texture of the fused region. The last measurement is taken after the build platform lowers a step height of 40 μm. This measurement evaluates the height drop of the build platform and the average thickness of the next powder layer.

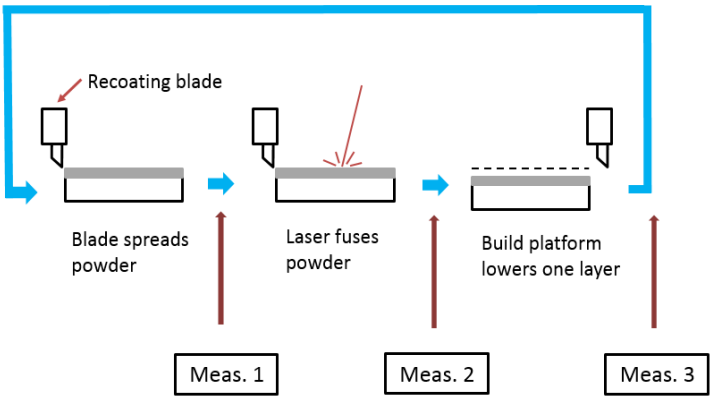

Figure 3-4: Three measurements are taken on each layer during the LPBF process.

3.1.3 Full-field Powder Bed Measurements

To demonstrate the performance of the proposed fringe projection system, some measurement results are shown and compared with the photograph generated by averaging all fringe images. The topography maps are expressed relative to a fixed reference coordinate system through the entire build process. This result is achieved by subtracting a reference unwrapped phase map generated at the first fresh powder layer from the unwrapped phase maps of all subsequent layers. Figure 3-5 shows the measured topography of a freshly laid powder layer (not the first layer). The powder layer is not

evenly distributed intentionally because the laser fusion only takes place on the left side of the powder bed; therefore, the left side of the powder layer is higher than the right side. This is clearly shown in the topography measurement, but not evident in the photograph.

Figure 3-6 shows the image and the topography map of the powder surface after fusing some selected regions of the powder. The average height of the fused region is lower than the unfused powder region due to the density change through the fusion process. The fused regions is distinguishable in the gray image, but the topography map shows its superiority by providing the height distribution of the surface. The average height drop of the fused region measured from the topography map is approximately 58 μm. The height drop of the fused powder is related to the shrinkage ratio, the powder layer density (different than the powder density) and the fused metal density which can, in theory, be used to calculate the porosity of the fused metal and to determine the efficiency of the fusion process. Further analysis of the height drop can provide insights of the fusion process. Due to the scope of this research, the author will not investigate more here.

Figure 3-7 shows the image and the topography map of the powder surface after the build platform is dropped 40 μm and the recoating arm has gone back to its starting position. The topography map shows some powder "bumps" around the second fused square on the left, and this is likely caused by the drag of excessive powder on the surface by the recoating blade as it moves back to its starting position. The recoating blade moves from the top to the bottom in the picture. Even though the powder "bump" will be smoothed out with the next layer of powder, detection of such signature will help diagnosis of the recoating arm errors and prevent them in the future build.

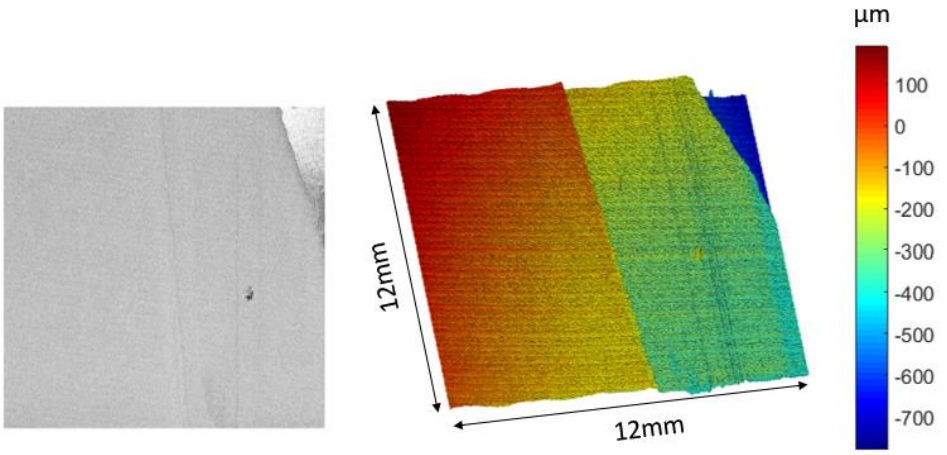

Figure 3-5: Fresh powder layer: a photo (left) and a topography (right).

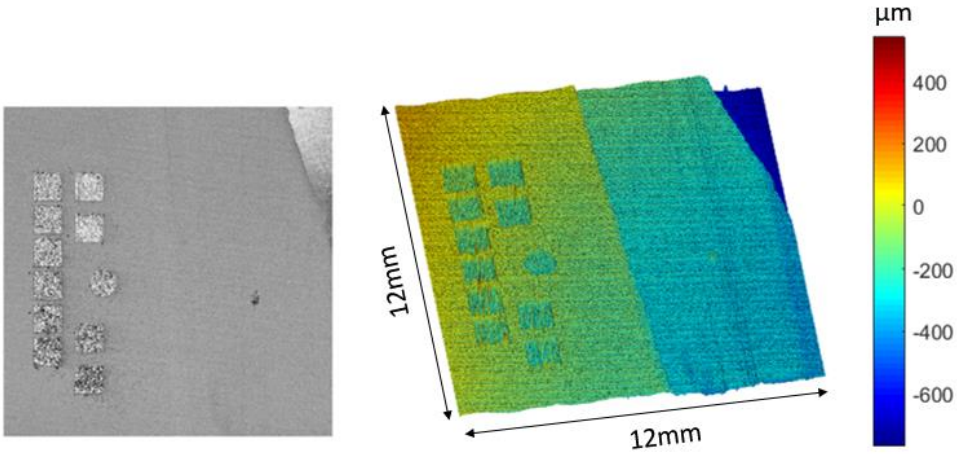

Figure 3-6: Powder layer after laser fusion: a photo (left) and a topography (right).

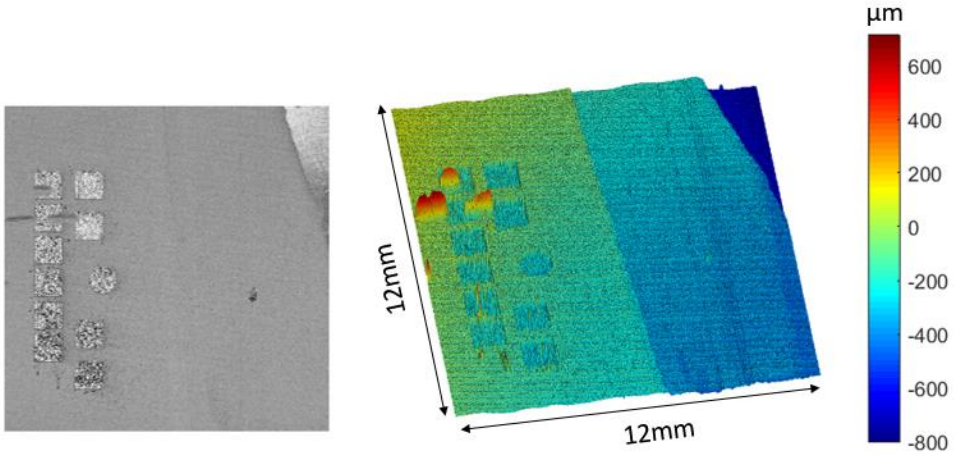

Figure 3-7: Powder layer after platform drop: a photo (left) and a topography (right).

Figure 3-8 shows the difference of the height maps before and after laser fusion. The major difference is in the fused regions which have a lower average height than the unfused powder region due to the material density change during the fusion. With the powder surface form removed, this height map is useful for evaluating the relative height difference between the fused and the unfused regions, which can reflect other process characteristics.

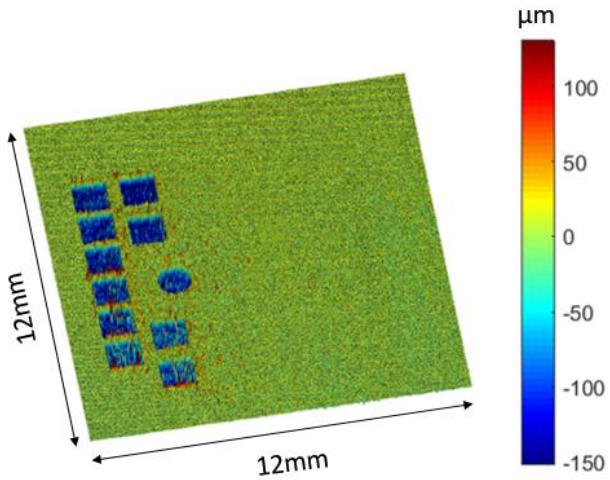

Figure 3-8: Difference of the topographies measured before and after the laser fusion (color bar range ±3σ).

Figure 3-9 shows the difference before and after build platform drops. The differences between the two maps reflect the build platform drop and any changes on the surface as the recoating arm returns to its starting position. The average height of the height map is -43 µm, which is consistent with the programmed stage drop, 40 µm. Again, this map shows the powder bumps created by the returning recoating arm dragging a small amount of powder and deposition that likely occurred.

More useful information can be discovered by tracking the average height of this difference map. Figure 3-10 shows that the height drop of the build platform through 30 layers of the build is approximately 40 µm with a deviation of approximately 5 µm. This

measurement is consistent with the 40-μm programmed stage height drop through the 30 layers of build, except for the 20th layer.

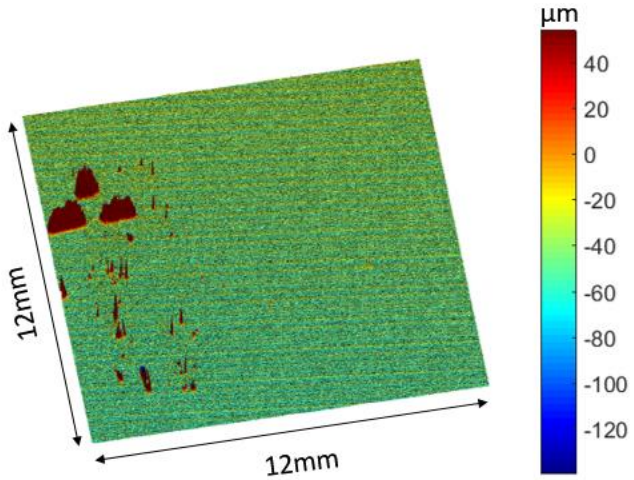

Figure 3-9: The difference of the topographies measured before and after build platform drop (color bar range ±3σ).

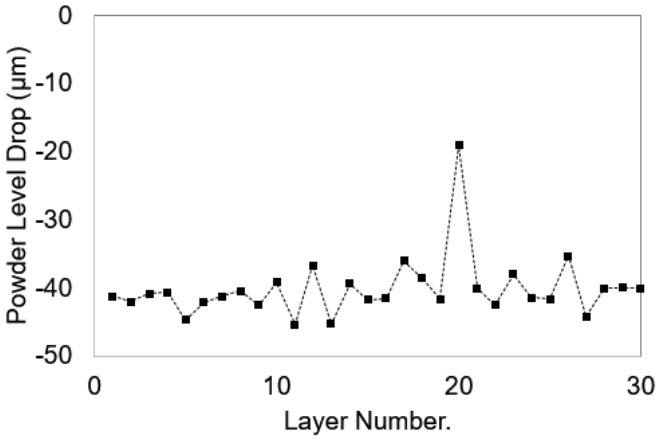

Figure 3-10: Tracking of average height drop of the build platform through 30 layers of the build.

In summary, this study succeeds in measuring the topography maps of the powder layer surfaces both before and after laser fusion. The topography measurements offer the potential for benefits in the analysis and characterization of the build area, including measuring the height distribution, measuring the height drop of the fused metal,

determining boundaries of the fused region, and tracking the height drop of the build platform.

3.2 In situ Local Powder Bed Measurements

3.2.1 New System Geometry

A second-generation fringe projection system is designed and built to measure the local fused regions in the powder bed with a higher spatial resolution. We use a machine vision camera (PointGray Flea3, resolution 4096×2160 pixels) with a 50-mm high-resolution lens (Edmond Optics Part No. 86574) that is already installed in the machine chamber. This camera is placed approximately 200 mm above the powder bed, providing a measurement field of 28 × 15 mm^2 and a pixel footprint of 6.8 μm. Figure 3-11 shows the second-generation fringe projection system. The projector is mounted on top of the chamber, illuminating the powder bed at an angle of approximately 35° through an anti-reflection coated window. The distance between the projector and the powder bed is about 532 mm/cos (35°) = 650 mm. At this distance, the customized projection system creates a 42 × 26 mm^2 image, which allows us to generate a dense fringe pattern as small as 0.32 mm/cycle to achieve the desired height sensitivity.

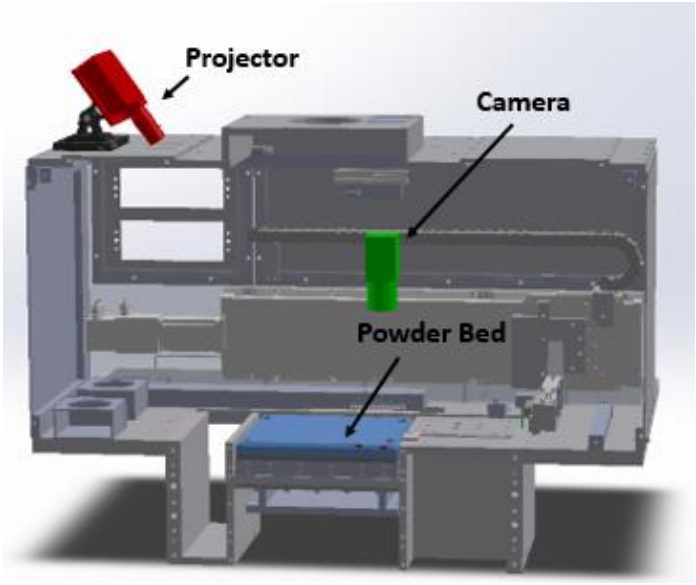

Figure 3-11: Second-generation fringe projection system (some machine components are hidden for clarity).

To achieve a higher measurement sensitivity, the system uses a smaller effective wavelength which is achieved by replacing the original projection lens with a custom-made long-focal-length lens. The effective wavelength is a function of the triangulation angle and the projected fringe pitch. Estimates of the desired sensitivity calls for an effective wavelength smaller than 1 mm/cycle. The effective wavelength is mainly determined by the projection image size and the resolution. The Nyquist sampling theorem requires the minimum sampling rate for a sine wave to be two pixels per cycle, and added noise considerations suggest the use of at least 8 pixels per cycle. Most commercial projectors have a pixel footprint of approximately a half millimeter, which limits the effective wavelength to over 5 mm/cycle (assuming a triangulation angle is 35°). Assuming we achieve the phase error limit of 1/100 wave, this limit leads to an estimate of the height uncertainty of ±50 μm (k=1), which do not meet the measurement requirements. To overcome this limit, a customized projection lens is designed.

3.2.2 Design of a Projection Lens

The small projected image is achieved by replacing the original projection lens with a custom lens. In doing so, the projector is modelled as a "reverse" camera where the digital micro-mirror device (DMD) is "imaged" by the projection lens onto the screen. The Qumi Q5 projector contains a Texas Instrument DLP4500 DMD chip whose native resolution is 911 pixels (columns) × 1139 pixels (rows). Figure 3-12 (a) shows the resolution and dimension of the DMD chip. The DMD is 9.855 mm in width and 6.161 mm in height. Figure 3-12 (b) shows the pixel arrangement of the DMD. Each pixel is approximately 7.6 μm long on the side and 10.8 μm long diagonally. The pixels are oriented at a 45° angle; the columns are numbered at every other pixel and the rows are numbered at each pixel. This means the longer side of the DMD has fewer pixels than the shorter side. Thus, the conversion from the input image resolution (1280 × 800 pixels) to the DMD native resolution (911 × 1139) is presumably achieved by an interpolation algorithm.

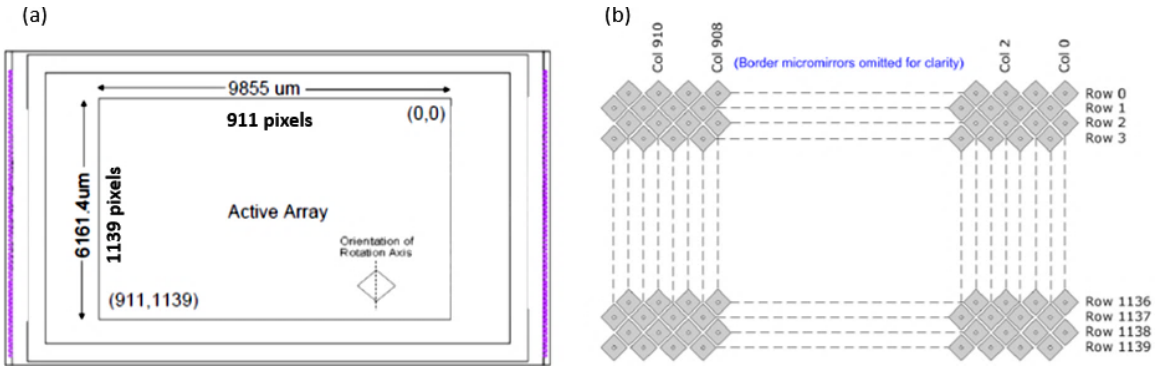

Figure 3-12: Texas Instrument DLP4500 DMD chip [100], [101]. (a) dimension of active pixel array, and (b) the diamond pixel arrangement.

Figure 3-13 shows the simplified geometry of the projector system, where the projection lens is modelled as a single lens. The magnification of the lens, *m*, is determined by the effective focal length at a given image distance, *z'*. This relation is described by

$$\frac{1-m}{z'} = \frac{1}{f_E}. \tag{3-2}$$

Figure 3-14 shows the magnification as a function of the effective focal length at a 650-mm projection distance. From the graph, we see that a 125-mm effective focal length has a magnification of approximately 4.2, leading to a pixel footprint of 7.6 μm × 4.2 = 32 μm. If the fringe orientation is parallel to the horizontal pixel array and 80 fringes fill the entire image, the average fringe pitch is 6.161mm ×4.2 /80 = 0.32 mm. Thus the average effective wavelength will be 0.32mm/*tan*(35°) = 0.45 mm/cycle.

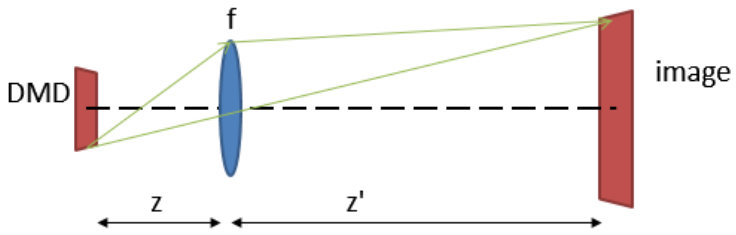

Figure 3-13: A single-lensed projection system.

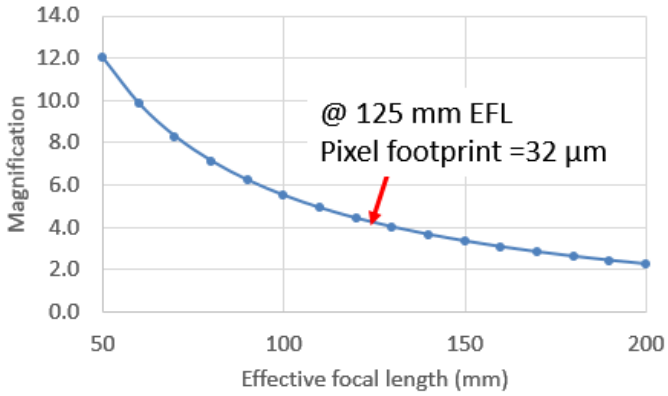

Figure 3-14: Plot of lens magnification versus effective focal length.

To test this design, the original lens in the Qumi Q5 projector is removed and replaced with a 125-mm achromatic doublet lens (Thorlabs AC254-125-A-ML). The experimental setup is shown in Figure 3-15. The external lens is placed approximately 155 mm before the DMD chip, and an aperture stop is inserted between the projector and the lens to limit

the field. The image observed on the screen at 650 mm shows that the achromatic doublet is sufficient to produce a sharp image of the sinusoidal fringe pattern.

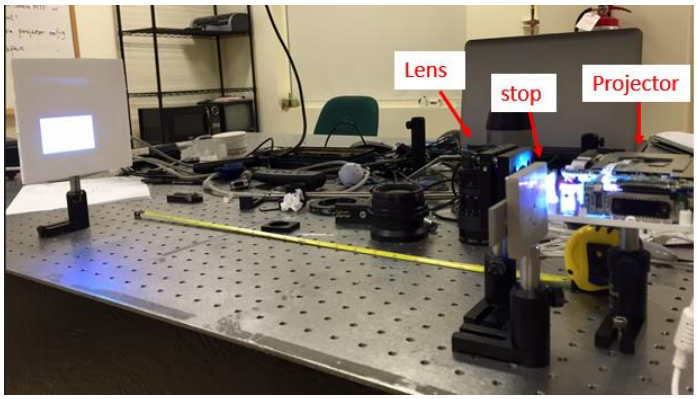

Figure 3-15: Testing projection image size with a 125-mm convex lens.

Figure 3-16 shows the configuration of the projection lens assemblies. A custom aluminum substrate is made to hold the projector body and the new projection lens. A threaded gauge plate (Thorlabs CP02) is used to position the projection lens such that the optical axis of the lens is aligned with the DMD chip. The projection lens consists of an adjustable lens tube (Thorlabs SM1NR1), an aperture (Thorlabs SM1D12D), and a 125-mm achromatic lens (Thorlabs AC254-125-A-ML).

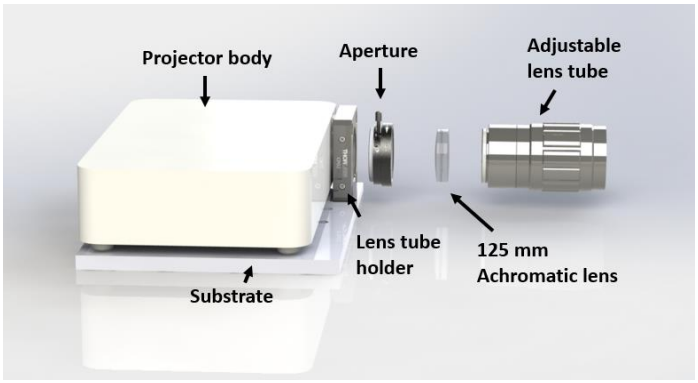

Figure 3-16: Qumi 5 projector and the redesigned projection lens assemblies.

3.2.3 Measurements of Local Fused Regions

To demonstrate local powder bed measurements, a 6 × 6 mm^2 square pillar is built with the nominal process parameters, i.e. laser power 290 W, scan speed 960 mm/s, hatch distance 0.09 mm and powder layer thickness 40 μm. The scan strategy varies from build to build. In this experiment, the laser scans back and forth along the recoating direction without rescanning the contour of the square as shown in Figure 3-17 (a). In addition, the scan direction alternates between adjacent layers. The powder surface is measured by the fringe projection system. An example of the fringe pattern on the fused square surface is shown in Figure 3-17 (b). The average effective wavelength is 0.52 mm/cycle. The height map of the measured surface is shown in Figure 3-17 (c). The black and white points on the height map are data drop-outs caused by shadowing and pixel saturation respectively. The height map provides rich information about the fusion process. Firstly, the fused region is surrounded with a narrow groove. This structure is not easily extracted from the photograph and is potentially useful for applications such as edge detection and geometric accuracy evaluation. Secondly, the average height of the fused surface is lower than that of the unfused surface because of the increase of density during powder fusion. This is observed as an average height change between the fused and the unfused regions. The average height difference between the fused and unfused surface can also be calculated by layers as a tracking parameter for monitoring the process. Thirdly, detailed features are observed in the height map of the fused region, such as abrupt changes in the elevation at the edges, and the height variation within the fused region. Some small spheres appear in the height map, particularly noticeable in the unfused region. They are most likely splatter drops formed during the laser fusion process. Splatter drops are expected on both fused and

unfused regions. Although the impact of splatter drops on final product quality is unclear, the ability to detect them may provide useful information for process control and yield assessment.

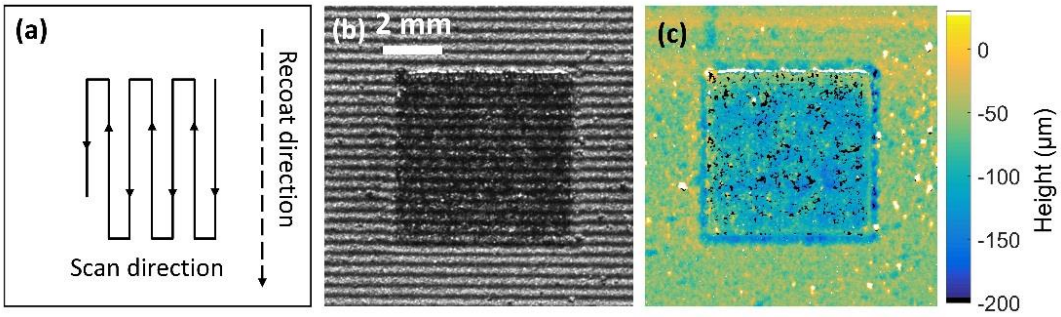

Figure 3-17: Demonstration the scan process on a powder bed. (a) Laser scan path and recoating direction, (b) photograph of fringe pattern on a fused powder surface, and (c) the corresponding topography. Black and white points in (c) are data drop-outs caused by shadowing and camera saturation, respectively.

The build process is monitored by taking two measurements for each layer. The first one is taken after the new layer of powder is spread on the powder bed, and this measurement monitors the evenness of the powder layer and waviness of the powder surface that can be caused by vibrations of the recoating arm. The second measurement is taken after laser fusion. These measurements provide rich information about the effects of the fusion process. Figure 3-18 shows the height maps of the powder bed at layers 2, 4, and 6. The color bars for the six figures are set to a range from -0.2 to 0.1 mm for easy comparison between the height maps. Several interesting aspects of the powder bed before fusion (left column) are evident. “Waviness” can be observed on the freshly laid powder layers. For example, the two small arrows next to layer 2 in Figure 3-18 show powder surface waves with a peak-to-valley height of approximately 28 μm. This is likely due to vibration of the recoating blade as it goes across the build area. Fused metal is also exposed above the powder surface in some locations where the local height of the build is higher

than the powder layer. This is observed as the saturated pixels (white points) along the edge of the fused region. The average height of the powder represents the average distance from the measurement plane to the camera. Thermal growth of the chamber or drift in the build platform position can cause this distance to change.

For the height maps after fusion (right column in Figure 3-18), the general features discussed above continue - a narrow groove is around the boundary of the fused area, the edges of the fused surface are slightly above the average powder height level, and the average height of the fused region is significantly below the powder level. The height maps also show that the fused surface changes with layer number. For example, the edge roughness reduces as the layer number increases. The height variation of the fused region also appears to decrease as the build layer accumulates, while the average depth (indicated by color) of the fused area increases with layer number.

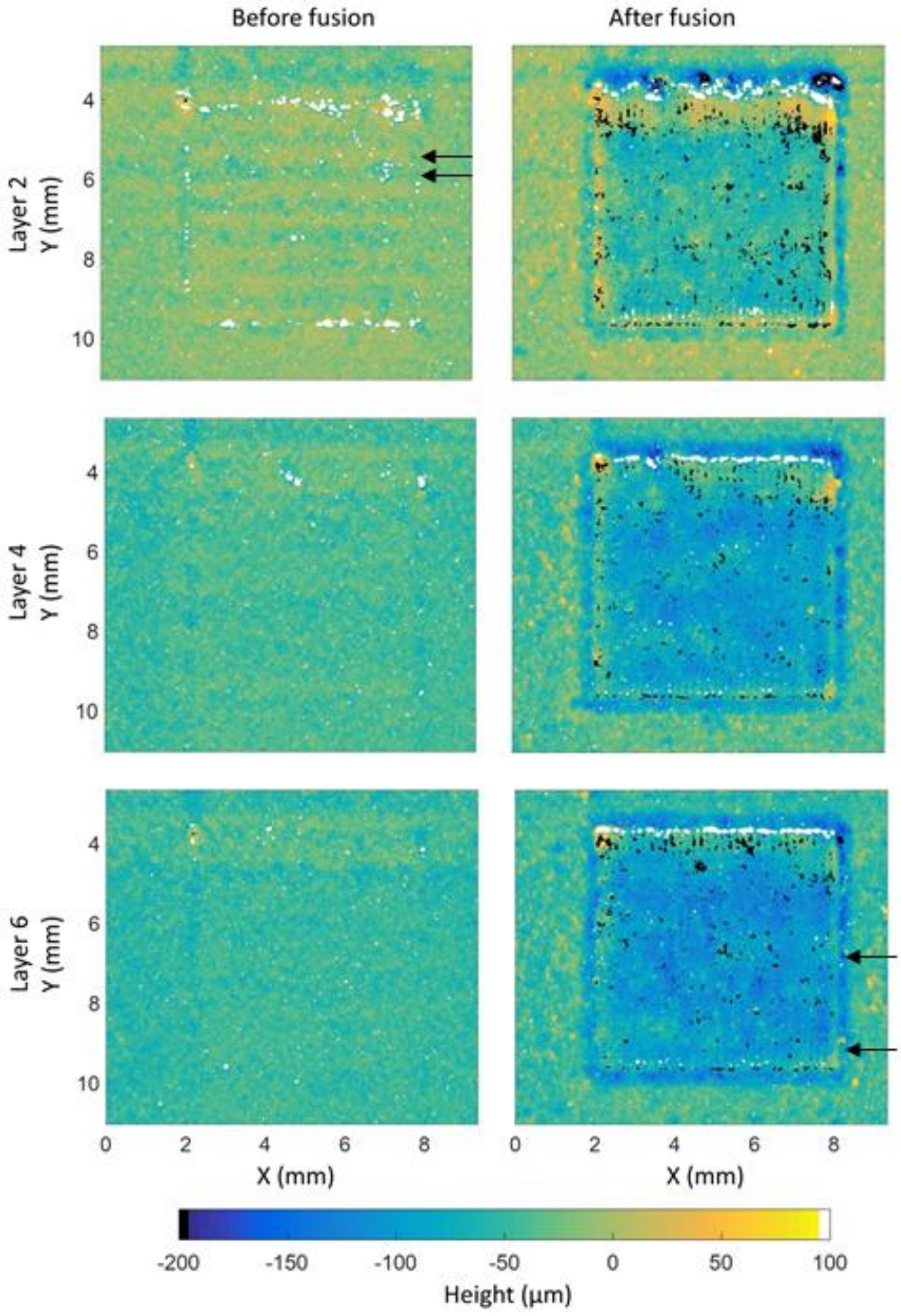

Figure 3-18: Height maps of the powder bed before and after laser fusion on every other layer.

The surface produced by LPBF process is expected to have an oriented linear texture along the laser scanning direction [34], and Fourier analysis of the height maps is used to

monitor such texture. As an example, the one-dimensional Fourier transform of each of the ten lines around the center and the edge of the fused region, indicated by the tick marks at the 6^{th} fused layer shown in Figure 3-18, are averaged together. The results are shown in Figure 3-19. The average Fourier transform at the bottom region shows a signature peak at the spatial frequency of 5.6 cycles/mm, which is the frequency corresponding to twice the hatch distance. There is no observable peak at the laser raster frequency, i.e. 11.5 cycles/mm, but this could be limited by the spatial resolution of the instrument. Although the instrument transfer function has yet to be characterized, it is reasonable to expect that measurements of spatial frequencies approaching 0.1 Nyquist (7.4 cycles/mm) are significantly attenuated [102]. Tenth Nyquist is indicated in the figure, and we see that the 11.5 cycles/mm laser scan spatial frequency (1/hatch distance) is to the right. Interestingly, the Fourier spectrum in the middle of the fused region does not show any strong peaks. Ex-situ measurements of the fused regions with a confocal microscope (with much higher spatial resolution and a 0.1 Nyquist frequency of 77 cycles/mm) confirm this claim. The high-resolution confocal measurement shows that the Fourier component corresponding to twice the hatch distance is stronger than the component corresponding to the hatch distance, suggesting an asymmetry in the fusion process when scanning toward the edge versus away from the edge.

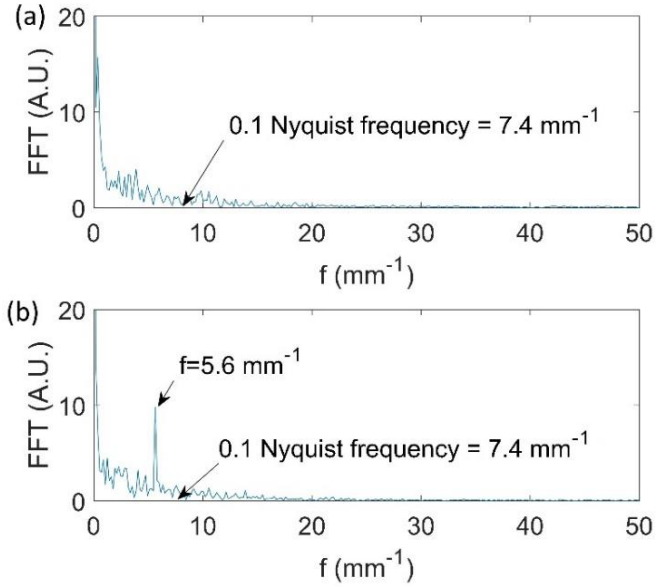

Figure 3-19: Fourier spectra of line traces at center (a) and bottom (b) at Layer 6 as indicated by tick marks in Figure 3-18.

The fusion process is expected to reach a stable state after a few layers of fusion. This can be monitored by tracking the average height drop between the fused and unfused regions. Figure 3-20 shows the average height drop as a function of layer number. A rapid decrease of the average height is seen in the first few layers, and then it converges to a constant value. The error bars in the graph are the standard deviation of the average height and are very small. A simple model is constructed to predict the trend of the average height drop. This model considers the powder shrinkage to be a constant factor during the process. The amount of height drop depends on the powder layer thickness and the shrinkage ratio. The shrinkage ratio, β, is defined as the ratio of powder density to the metal density. The average height drop for each layer, h_n, can be expressed as

$$\begin{aligned} h_1 &= -t \cdot \alpha\,, \\ h_2 &= -(t + h_1) \cdot \alpha\,, \\ &\vdots \\ h_n &= -(t + h_{n-1}) \cdot \alpha, \end{aligned} \tag{3-3}$$

where n is the layer number, t is the powder layer thickness and $\alpha = 1 - \beta$. The negative sign means the average height of the fused surface is below the powder level. This series represents a geometric progression, so the average height drop is written as

$$h_n = -t\alpha \cdot \left(\frac{1-\alpha^n}{1-\alpha}\right). \tag{3-4}$$

Notice this equation converges to a constant value. The average height drop is greater than the powder layer thickness for the first few layers because the shrinkage ratio, β, is smaller than 0.5. After a few layers of build, the height drop quickly approaches to a constant value, namely

$$\lim_{n\to\infty} h_n = -t \cdot \frac{\alpha}{\beta}. \tag{3-5}$$

A least-square approach is used to determine the best-fit value for α using the 40-μm powder thickness value as a constant [98]. The best fit indicates a value for α of 0.59, representing a powder-to-metal density ratio of β =0.41. Inserting this value of α into Equation 3-5, the steady-state height drop is estimated to be 58 μm. The model with these parameters, Equation 3-4, is also plotted in Figure 3-20.

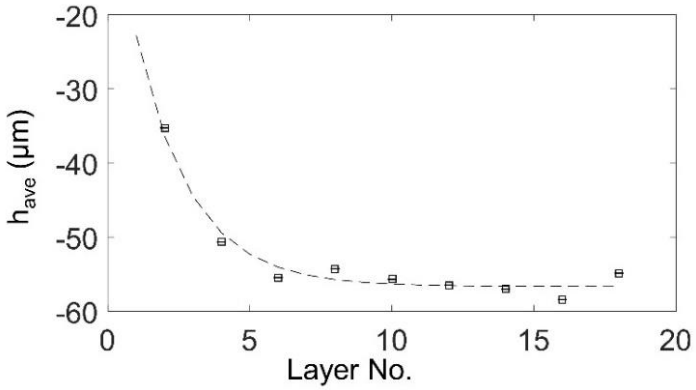

Figure 3-20: The average height difference between the fused metal and the unfused powder converges to a constant after several layers of build. This agrees with our mathematical model (the dashed line).

To demonstrate the ability to measure the surface variations on the fused metal surface, a 1× 1 mm^2 patch is cropped from the center of the fused region in Figure 3-18. The height map of this region is shown in Figure 3-21. The measurement shows that the fused region has over 120 μm in height variation over this area. Figure 3-21 (b) shows the profile of a line in the center of the map. The peak-to-valley height variation of this profile is approximately 75 μm.

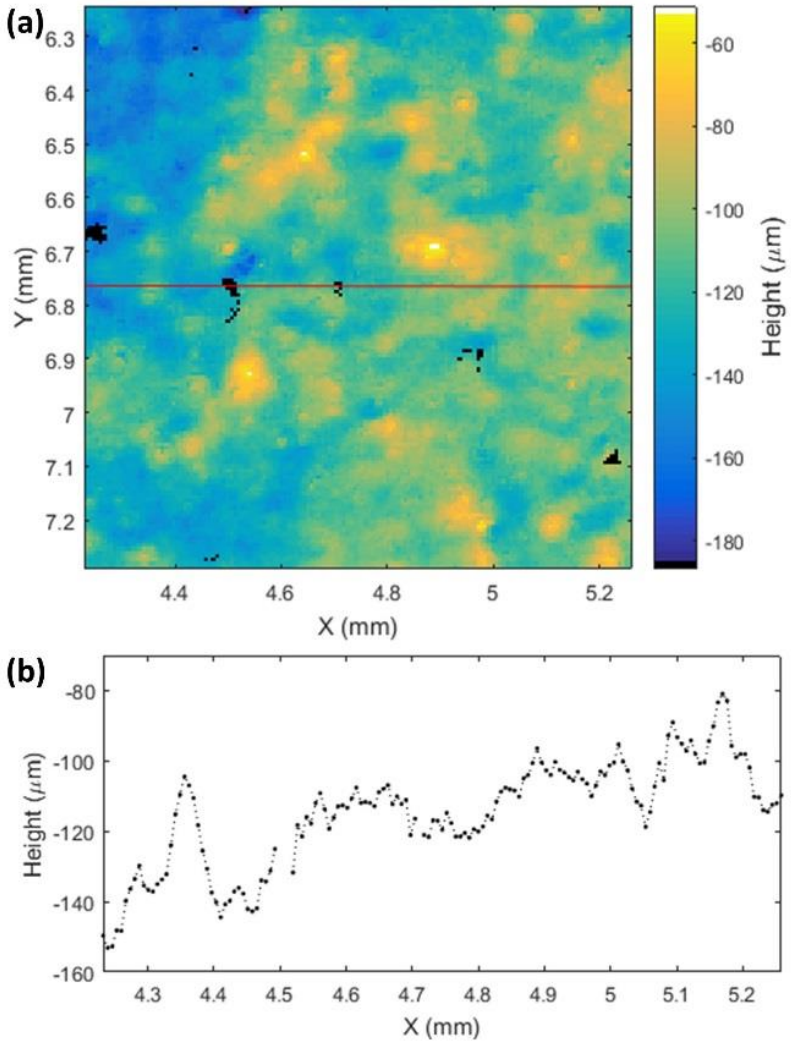

Figure 3-21: Demonstrating the ability to measure surface variations on a fused metal surface. (a) The height map of a fused surface created with 350W laser power at the 18th layer, and (b) a line trace at the center.

3.3 Summary

We develop two fringe projection systems for measuring a powder bed during the LPBF process. The first system has a measurement field of 120 × 120 mm^2. This system provides topography maps of the entire powder bed area and can be used to inspect the evenness of the powder layer and to detect waviness created by vibration of the recoating arm. The full-view powder bed measurements also show height drop between fused and unfused regions due to the change of material density. It also provides tracking of build platform movement throughout the build.

Through modifying the projection lens, we develop our second-generation fringe projection system with an average effective wavelength of 0.5 mm/cycle. This system uses the machine vision camera with a 50-mm high-resolution lens which is already installed in the LPBF chamber. This camera provides a measurement field of 28 × 15 mm^2 with a pixel footprint of 6.8 μm. These two changes lead to better spatial resolution in the measurement which is demonstrated by selected topography maps of the powder bed. We observe detailed surface textures on the fused metal surface, including a periodic line structure which corresponds to twice the hatch distance near the edge of the fused region. We also measure the average height drop between the fused and unfused regions and find it increases in the first few layers of build and converges to a constant value which can be greater than the powder layer thickness if the shrinkage ratio is smaller than 0.5. We also examine the variations on the fused metal surface by zooming in the topography map to a 1 × 1 mm^2 area. This topography map shows the surface created by a LPBF process have a height variation of approximately 100 μm.

CHAPTER 4: EVALUATION OF HEIGHT MEASUREMENT PERFORMANCE

4.1 Introduction

After the fringe projection system is developed, one has to address the following questions: What is the measurement capability of the system? What is the smallest feature that can be measured? What is the physical limitation of the instrument? There are no short answers to these questions. The primary reason is that the performance of the instrument can be quantified only with a specific definition of a measurand, and the analysis is detailed and measurand specific. It is obvious that the function of a measuring instrument is taking measurements; therefore, the quality of a measurement is quantified by its uncertainty. Thus, the measurement performance of the instrument must be evaluated by determining the uncertainty of the measurements. In other words, the uncertainty measures the measurement capability of the instrument for a specific measurand. There are usually multiple measurands that can be estimated from data, and this is especially true for higher dimensional data like surface topography measurements.

Measurement noise can be divided into two parts, noise from internal sources in the instrument and noise resulting from operational and environmental errors. The idea of a better instrument leading to better measurements only holds true when the instrument is operated under ideal conditions where the instrument noise is the primary error source in the measurement procedure. The instrument noise is only a part of the measurement noise. Operational errors and environmental errors can also affect the uncertainty of the measurements. One mostly relies on the specifications provided by the manufacturer when

choosing an instrument for a certain measurement. While the instrument specifications provide a general idea of what the system is capable of measuring, they usually do not speak specifically about expected measurement uncertainty for specific measurands. Table 4-1 shows the specifications of several commercial fringe projection systems. Some of the commonly quoted parameters are the vertical resolution, the z accuracy, the measurement uncertainty, the lateral resolution, the lateral sampling/minimum point spacing. Those parameters can be roughly divided into two classes – the vertical measurement specifications (listed as specification 1 in Table 4-1) and the lateral measurement specifications (listed as specification 2 in the table). In this chapter, we will discuss the vertical measurement specifications. The lateral measurement specifications will be discussed in the next chapter.

Table 4-1: Specifications of some commercial fringe projection systems.

Instrument	Specification 1	value	Specification 2	Value
8tree DentCheck	Uncertainty (Depth)	± 50 μm (95% confidence)		
AICON StereoScan			Minimum point distance	12 μm
HP Pro S3	Resolution/Precision	0.05% of scan size		
LMI Technologies DHI advanced R4X	Accuracy (@ 212 mm FOV)	36 μm	Point to point distance (@ 212 mm FOV)	0.071 mm
LMI Technologies MikroCAD Plus	Resolution z	0.7 μm	Resolution x	0.7 μm
Shape Drive G2-20-100-1	Z accuracy, 1σ	1 μm	Lateral sampling	10 μm
Shape Drive G3-30-180SH	Z accuracy, 1σ	0.7 μm	Lateral sampling	7 μm

A common mistake in many specifications is the use of accuracy as a parameter to characterize the vertical measurement limit. Accuracy is a qualitative concept of a measurement, rather than a quantitative measure of an instrument [103]. Another problem with those specifications is the use of term ‘resolution’. Resolution is an ambiguous parameter for topography-measuring instruments. The definition of resolution varies with the field of study. In dimensional metrology, the resolution is often defined as the smallest digit of the output value, not necessarily the smallest input change that can be measured by the instrument. For example, an instrument having a 1 nm vertical resolution does not mean the instrument can measure 1 nm height change. It simply means the electronics can output a number to this digit; the resolution does not represent the measurement capability! In optics, the resolution is an important and widely used metric to characterize the performance of an imaging system. It is defined as the smallest spacing between two lines that can be resolved by an optical system. However, the meaning of resolution for a topography-measuring instrument is not well established. A survey of the commercial and scholarly literature shows that there is no widely-recognized definition of resolution for a fringe projection system. In the literature, the performance of a fringe projection system is commonly described as some kind of standard deviation or the RMS parameter of a flat surface [43], [67], [76], [86], [104], [105]. Although this isn’t completely unreasonable, the measurement capability should be defined more rigorously and specifically, with precise language. For example, the community would be better served with the definition of specific measurands and uncertainty estimates for measurements of this measurand.

The Guide of Uncertainty of Measurement gives definitions of terms commonly used for discussing instrument capabilities – repeatability, precision, and accuracy [106]. The

repeatability of measurements is the standard deviation of successive measurements of the same measurand carried out under the same measurement conditions. Measurements are repeatable when the measurement results have a small standard deviation. Measurements which have a small random error are considered precise even if they may deviate greatly from the measurand (the nominal true value). The deviation between the measurements and the measurand is a systematic error, which may be corrected by a calibration procedure. Precision requires a measurement to be repeatable, but a repeatable measurement is not necessarily precise. A measurement which has a small systematic error is considered accurate as the random error can be reduced by averaging. The means of evaluating the measurement capability in this chapter will follow the three basic concepts mentioned above. First, we adopt a metric called the surface topography repeatability as a measure of the repeatability of a surface topography measurement. Second, we carry out an intercomparison between the R_a parameter of a surface roughness sample measured by the fringe projection system and by a commercial tactile profilometer.

4.2 Surface Topography Repeatability

Repeatability is the scattering of consecutive measurements of the same measurand under the same measurement conditions over a short period of time [106]. When the measurand is a single value, the repeatability is simply the standard deviation of all measurements. However, when the measurand is a topography map, such as the output of a fringe projection system, the repeatability can be assessed by the surface topography repeatability. The surface topography repeatability is the repeatability of topography

measurements of the same surface under the same measurement conditions over a short period of time [107].

A quick way to estimate the surface topography repeatability is to calculate the standard deviation of the difference between two topography maps measured successively. This is similar to the calculation of the surface roughness parameter, *Sq*, except for the difference between two repeated topography maps rather than for a single map. Assuming the measurement noise in the two measurements is equal, the surface topography repeatability is approximately the root mean square of the difference divided by the square root of two, namely

$$r_s = \frac{RMS[h_1(x,y) - h_2(x,y)]}{\sqrt{2}}. \qquad (4\text{-}1)$$

More rigorously, the surface topography repeatability can be estimated as the mean root-mean-square (RMS) of the difference between a number of topography maps and their mean, namely

$$r_s = \frac{1}{N}\sum RMS\left[h_i(x,y) - \bar{h}(x,y)\right]_i. \qquad (4\text{-}2)$$

As the number of measurements increases, the random noise in the average decreases as $\sqrt{N}$. The surface topography repeatability quantifies the scattering of successive topography measurements, and expresses it as a single value. The surface topography repeatability is a good estimate of the measurement noise of the instrument, including the internal instrument noise and the external noise such as the environment and operational factors [107]. When the instrument is operated under ideal conditions (meaning the environmental factors and other factors are small) with a sample that is considered suitable

for the measurement principle, the surface topography repeatability can be a good estimate of the instrument noise.

We evaluated the surface topography repeatability of our instrument with three different surfaces -- a sprayed float glass surface (coated with a thin layer of Spotcheck spray paint), a powder surface and a fused metal surface. The coated glass surface is also used in the effective wavelength calibration procedure because it is considered as an ideal (or at least close to ideal) surface for the fringe projection technique. Of course, surface topography repeatability of the powder surface and the fused metal surface are of particular interest. The measurements of those surfaces are taken using the local topography measurement setup on the LPBF machine as shown in Figure 3-12. The measurement area on the sprayed glass surface and the powder surface is the full measurement area of the camera, namely about 28 × 15 mm. The measurement area on the fused metal surface is approximately 5.5 × 5.5 mm. For each surface, we took $N=30$ measurements in approximately 10 minutes. The piston and the tilt are removed from each topography map. This means we only measure the deviation of the relative height on each topography map from a best-fit plane.

Figure 4-1 to Figure 4-3 shows the difference between one topography measurement and the mean of the 30 measurements for the three surface samples. The color bar range is set to ±3σ of the surface height. The deviation on the powder surface is approximately the same as that on the sprayed glass surface, indicating the powder surface is close to the ideal surface for the measurement principle. For the fused metal surface, the difference map between one topography and the mean of 30 topographies has a bigger deviation compared to that of the sprayed glass surface and the powder surface. This is because the signal-to-

noise ratio of the acquired fringe patterns on the metal surface is lower than on the powder surface due to the low diffuse scattering properties of the metal surface. There is also a noticeable percentage of data dropouts (pixels are removed from the measurement results because the pixels are either saturated or not receiving enough signal) in the fused metal surface measurement owing to setting high and low thresholds, 240 and 40 respectively, on the fringe images. The data dropout is an important observation, but it does not directly affect the calculation of surface topography repeatability, as the missing data points are removed from the RMS calculation.

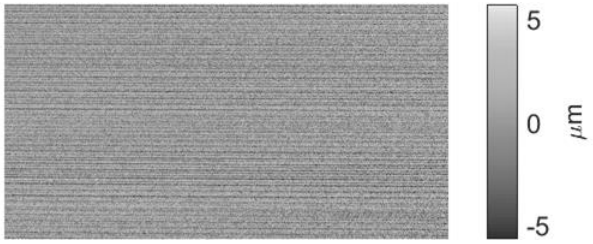

Figure 4-1: Difference between one measurement of the sprayed glass surface and the mean of 30 measurements (Color bar range ±3σ).

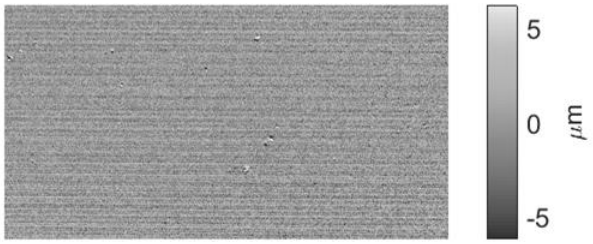

Figure 4-2: Difference between one measurement of the powder surface and the mean of 30 measurements (Color bar range ±3σ).

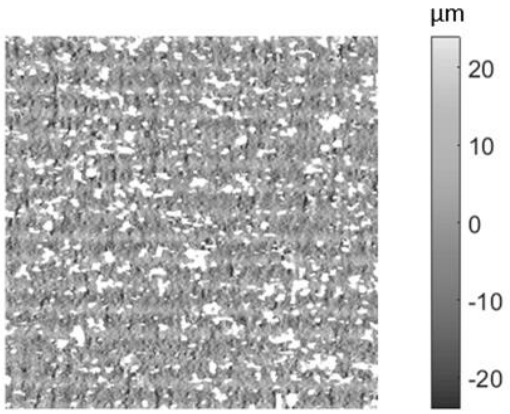

Figure 4-3: Difference between one measurement of the fused metal surface and the mean of 30 measurements (Color bar range ±3σ). The white regions are data dropouts.

Figure 4-4 shows the RMS of the difference between each measurement (of the thirty) and the mean for the three surface samples. The RMS values are approximately the same for the sprayed glass surface and the powder surface, while the RMS values on the fused metal surface are much larger. This is because the fused metal surface is less diffuse; therefore, the signal-to-noise ratio of the fringe images is significantly lower compared to that on the sprayed glass surface and powder surfaces. The mean of these RMS values is the surface topography repeatability, r_s (Equation 4-2). For the three different surfaces, the surface topography repeatabilities are 2.0 μm, 2.1 μm, and 8.4 μm, which are about 0.4%, 0.4% and 1.7% of the average effective wavelength of 0.5 mm/cycles, respectively. The surface topography repeatability is surface-dependent as the signal-to-noise ratio of the acquired fringe pattern is subjective to the surface scattering; therefore, it should be evaluated on a case-by-case basis. The sprayed glass surface is considered an ideal surface for the fringe projection system; hence, the surface topography repeatability is as low as 2.0 μm, implying the measurement limit is 2.0 μm when the system uses an effective wavelength of 0.5 mm/cycles. The powder surface has a surface topography repeatability, 2.1 μm, close to that of the sprayed glass surface, meaning the repeatability is very close

to the measurement limit and the surface is very close to the ideal surface. The metal surface presents a much larger surface topography repeatability of 8.4 μm, meaning the measurement on this surface is typically less repeatable. Table 4-2 summarizes the results.

Table 4-2: Surface topography repeatability on three surface samples.

Surface	Surface topography repeatability (μm)
Sprayed glass surface	2.0
Metal powder surface	2.1
Fused metal surface	8.4

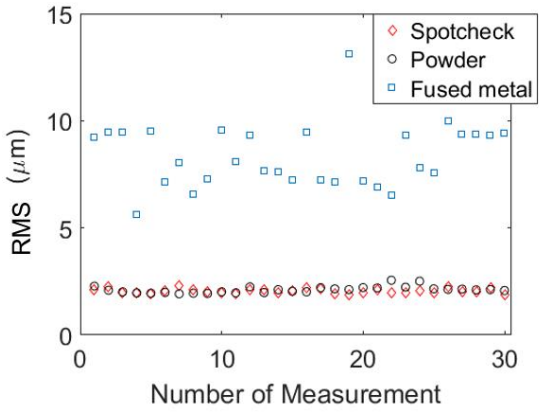

Figure 4-4: RMS of the difference maps for three surface samples.

4.3 Intercomparison of R_a

Carrying out an inter-comparison is useful in evaluating instrument performance. Measuring the same measurand using two different instruments is a good approach to check the performance of a newly developed instrument. Direct comparison between two topography measurements is not practical because each measurement has its own uncertainty associated with the instrument noise and the noise from the measurement procedure. A practical approach is to measure the same roughness parameter on the same surface with two instruments and then compare the measurements. An example of an

intercomparison between fringe projection and tactile sensor can be found in the paper by Windecker et. al. [105]. This section discusses an arithmetic mean roughness, R_a, comparison of a surface roughness sample as an example of this test.

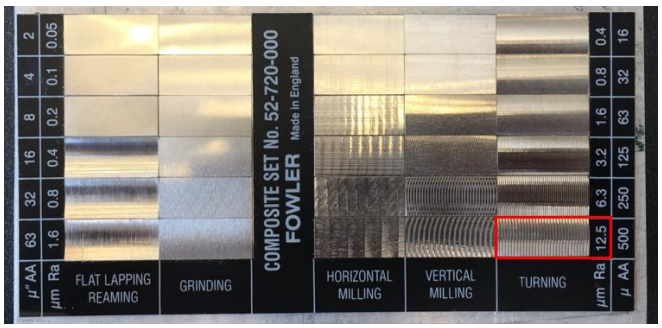

Figure 4-5: Surface roughness sample plate.

Figure 4-5 shows the surface roughness sample plate (Fowler No. 52-720-000) used in this experimental study. This plate includes five different types of surface roughness samples each of which was created by a specific machining process. Each surface type contains six different roughness levels. We choose the surface roughness sample produced by a machine turning process because its primary spatial wavelength of 0.72 mm is far below the cut-off wavelength of our fringe projection system. This sample is approximately 20×6 mm^2 which is roughly one-third of the measurement field. The nominal value of the R_a parameter is 12.7 ±1.5 μm and the nominal R_t parameter (peak-to-valley depth roughness) is 50 ± 15 μm. The nominal values are not for benchmarking for this intercomparison study since these roughness samples are made for a visual comparison purpose only [108].

The metallic surface finish of the roughness sample is not ideal for a fringe projection technique, but it is possible to produce topography measurements when proper operational parameters are chosen. Here the projector is illuminating the surface at an angle of

approximately 50° and the camera is imaging perpendicular to the surface. Most specularly reflected light is avoided and the camera collects scattered light from the surface. A relatively long exposure time is used to accommodate the low scattered signal. Figure 4-6 shows the topography map of the roughness sample measured by the fringe projection system. The topography map is approximately 20 mm in length and 4.38 mm in width with a sampling interval of 4.7 μm. The color bar presents the peak-to-valley height difference of the surface. This surface has a primary wavelength of 0.72 mm, which is the wavelength of the roughness.

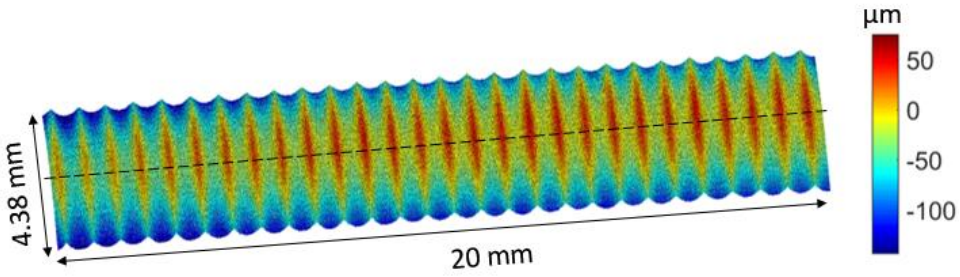

Figure 4-6: Topography map of turned surface from a Fowler surface roughness sample measured by the fringe projection system. The dashed line indicates where the roughness parameter is calculated.

To calculate the roughness parameter R_a from the topography map, a profile from the center of the sample is extracted as shown in Figure 4-7 (a). The extracted profile has significant random noise which will affect the roughness calculation. To reduce the noise, 100 profiles around the center line are extracted and the R_a values of the 100 profiles are calculated. The average of the 100 R_a values is 17.9 μm, and the standard uncertainty of the mean is 0.3 μm (k=1). To reduce the random noise, the extracted 100 profiles are averaged to create an averaged roughness profile as shown in Figure 4-7 (b). The difference between profiles (a) and (b) is shown in Figure 4-7 (c). The RMS value of the difference profile is 3.6 μm. The R_t value is also estimated by reading the peak-to-valley distance from

the averaged roughness profile in Figure 4-7 (b). The measured R_t parameter is approximately 60 μm.

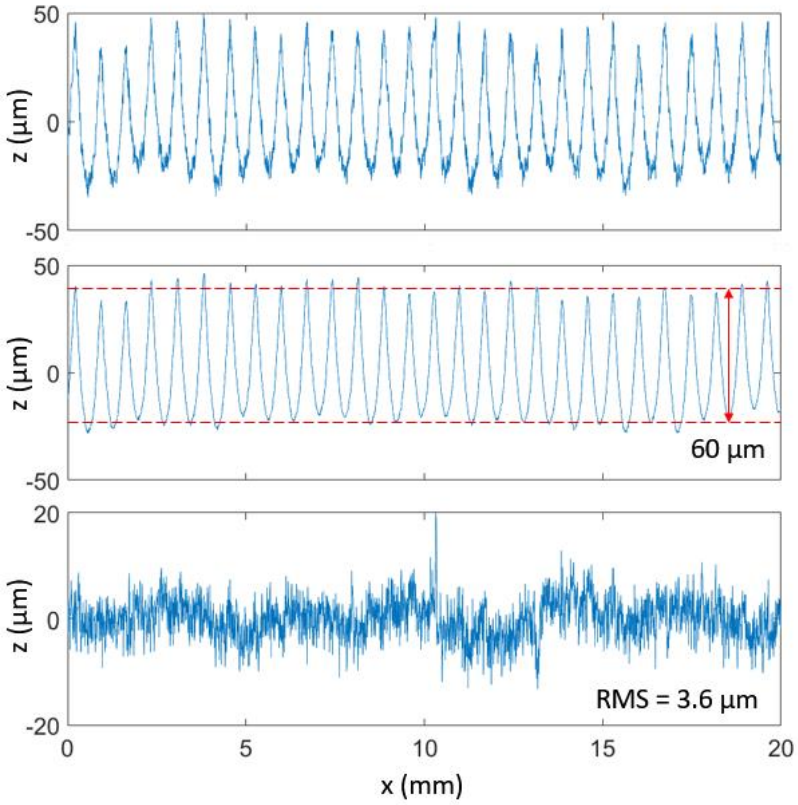

Figure 4-7: Calculating the roughness parameter R_a from the topography map in Figure 4-6: (a) One profile from the center of the surface (b) the average profile from 100 lines around the center of the surface, and (c) the difference between the averaged profile and the profile at the center.

The surface roughness sample is then measured by a commercial surface profilometer (Mahr LD 260) which is believed to have a higher degree of accuracy. Three measurements were made; each measurement is approximately 18 mm in length with a sampling interval of 0.1 μm. The R_a value for the three measured profiles are 18.31 μm, 18.33 μm and 18.13 μm, respectively. The mean R_a value is 18.3, and the standard deviation is 0.1 μm. For a visual comparison, the mean of the three profiles is calculated and aligned with the mean

of 100 profiles measured by the fringe projection system as shown in Figure 4-8. The comparison shows the two averaged roughness profiles are similar.

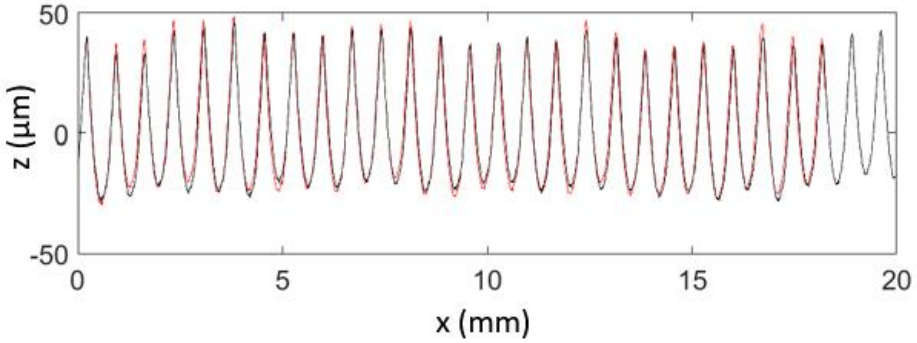

Figure 4-8: Comparison of surface roughness measurements by a fringe projection system (black line) and a commercial profilometer Mahr LD 260 (red line).

Table 4-3 compares the R_a values measured by the fringe projection system and by the contact profilometer. The two measurement results have an overlap with a k=3 expanded uncertainty, suggesting the fringe projection system is well calibrated and can produce accurate measurements for the right roughness samples. In the roughness calculation, the measured profile is usually filtered based on the spatial wavelength of the roughness. We measured similar R_a values from both measurements even without applying spatial filtering. A possible reason for that is the primary wavelength of the roughness sample is very low; therefore, although measured by different instruments, the two profile measurements have a similar powder spectra density function.

Table 4-3: Comparison of the measured R_a roughness parameters.

	Nominal	Fringe projection	Tactile profilometer
R_a (μm)	12.5 ± 1.5	17.9 ± 0.3 (k=3)	18.3 ± 0.3 (k=3)

CHAPTER 5: CHARACTERIZATION OF THE SPATIAL RESOLUTION

5.1 Introduction

Fringe projection is a novel technique for surface inspection of the layered metal additive manufacturing (AM) process [109], [110]. When used as a surface texture/roughness measuring tool, this technology offers several benefits over traditional interferometry methods. Firstly, the instrument can be placed far from the object to be measured such that the measurements can be made in situ. Secondly, the fabrication cost is relatively low compared to interferometers because of the less rigid optical fabrication and alignment tolerances. Fringe projection metrology is widely used for 3D shape and surface form measurement applications where the surface texture/roughness is not of interest; therefore, the spatial frequency response is not a concern. The spatial frequency response becomes important when the surface texture is of interest. Rough and textured surfaces, particularly additive manufactured surfaces, contain rich spatial frequency content; the fidelity of measurement greatly depends on the spatial frequency response of the system. Some studies of fringe projection as a surface texture/roughness measuring technique exist, but the spatial frequency response is not investigated in these papers [38], [86], [105].

The instrument transfer function (ITF) has been proposed as a useful metric for characterizing the spatial frequency response for a topography measuring instrument, but the knowledge is limited to interferometers [88], [111], [112]. ITF is a useful metric for characterizing the fidelity with which the instrument will respond to height changes on the

surface. This is a complementary metric to the idea of resolution as a minimum separation needed to distinguish two small features on a surface. ITF characterizes the ratio of measured amplitude to the actual amplitude. The spatial frequency length scale where the ITF falls to 50% is called the lateral period limit; this is claimed as an appropriate number to quote as the lateral resolution for a topography measuring instrument [113].

The application of ITF to fringe projection metrology is relatively new, and the literature related to this is limited. Berssenbrugge, et. al. investigated what they call the 3D transfer function of a fringe projection system [114]. The definition of this 3D transfer function is identical to the ITF, but the study overlooks the applicability of ITF to a fringe projection system. An ITF analysis approach is only valid when the system is linear. A fringe projection system is intrinsically nonlinear unless certain conditions are met.

In this chapter, we investigate the meaning, applicability and measurement of ITF to a custom fringe projection system designed for in situ measurement of metal AM surfaces. We examine two major factors that affect the linearity of the system – the system geometry and the optical filtering. The linearity conditions are defined and tested through simulations. We also explore the connection between the ITF and the MTF of the camera through a mathematical analysis as well as through simulations. We propose and demonstrate an ITF measurement technique using a stepped surface with a step height that is under the linearity limit. The measurement results are compared with an ITF prediction calculated through the simulation with an experimental MTF.

5.2 Theory

5.2.1 Definition of ITF

ITF can be defined as the ratio of the Fourier transform of a surface measurement to the Fourier transform of the actual surface. It is a comparison of the measured surface to the actual surface as a function of the spatial frequency. Only a linear system (or at least approximately linear) can be usefully characterized by the ITF. The linearity ensures that the frequency response of the measurement is independent of the frequency content of the surface being measured – that is, the measured amplitude of any spatial frequency is not a function of the amplitude of any other frequency.

For a linear system, the output, *g(x)*, can be described as a function of the input, *f(x)*, convolved with the impulse response, *h(x)*, namely

$$g(x) = f(x) \otimes h(x). \tag{5-1}$$

Taking the Fourier transform of this equation, the spectrum of the output can be written as

$$G(f) = F(f) \cdot H(f) \tag{5-2}$$

where *G(f)*, *F(f)* and *H(f)* are the Fourier transform of *g(x)*, *f(x)* and *h(x)*, respectively. The function *H(f)* is called the transfer function. If the input is a two-dimensional irradiance map (or an image), then the function *H(f)* is called the optical transfer function (OTF). To generalize this idea, when the input is a three-dimensional height map, the function *H(f)* is called the instrument transfer function, or the ITF,

$$H(f) = \frac{G(f)}{F(f)}. \tag{5-3}$$

5.2.2 Linearity Condition

Linearity is a requirement for a valid transfer function analysis. A fringe projection system is intrinsically nonlinear, but can be approximated as linear within a certain operational range. To decide this linear region, we can plot the output height (at each pixel) as a function of the input height, if known, and find the linear region in the plot. Linearity can also be interpreted in the spatial frequency domain. A linear system only attenuates the spatial frequency content through convolution with the impulse response function. A nonlinear system generates added spatial frequency content not present in the input signal. Thus, the system cannot be characterized with the ITF and therefore the ITF is not applicable.

For a fringe projection system, we investigate the linearity condition by first analyzing the system geometry. In section 2.2, we showed that the measured phase shift is linear to the height variations on the surface as long as the surface height variation is much smaller than the working distance ($z<<d$), or equivalently the fringe shift is much smaller than the distance between camera and projector ($\Delta x<<l$). This sets a geometric linearity constraint, that is the output and input are approximately linearly related if the surface variation is much smaller than the camera working distance. Our system satisfies this condition because the surface variation to be measured is always far smaller than the camera working distance. Further proof of this linear relationship is the phase versus height measurements taken for the effective wavelength calibration. Within the 1-mm vertical range, the measured phase is observed to change linearly with the relative height of the build platform.

Geometry is not the only constraint of linearity; a more important factor is the spatial filtering caused by optical diffraction and spatial sampling. A fringe projection system is

intrinsically nonlinear because of the optical filtering leading to a distortion of the "measured" surface. The modulation transfer function determines the attenuation of the spatial frequency components in the acquired images, leading to a systematic phase error in the measured phase maps. The phase shift introduced by the surface variations is encoded as the lateral fringe shift in the irradiance map. The spatial filtering of the irradiance map changes the apparent lateral fringe shift. The decrease of fringe shift is equivalent to an added phase error to the phase shift caused by the surface. The total phase shift captured by the system is the sum of the contributions both from the surface variations and from the spatial filtering.

We can gain more understanding of the source of nonlinearity by analyzing the irradiance map on a sinusoidal surface. For a linear shift-invariant system, the output of a sinusoidal input is also a sinusoidal signal [115]. For a nonlinear system, the output of a sinusoidal input is a distorted sinusoidal signal where the distortion gives rise to harmonics in the output signal. We use a sinusoidal surface to test the linearity of the fringe projection system. The irradiance modulation caused by the surface variations is written as

$$I(x,y) = I_0 + I_1 \cos\left[2\pi f_{carrier} x + 2\pi \cdot \frac{A}{\lambda_{eff}} sin\left(2\pi f_{surf} x\right)\right], \tag{5-4}$$

where I_0 is the average irradiance, I_1 is the amplitude of the sinusoidal irradiance pattern, A is the amplitude of the sinusoidal surface, f_{surf} is the spatial frequency of the sinusoidal surface (object frequency), and $f_{carrier}$ is the spatial frequency of the sinusoidal fringe pattern (carrier frequency). The sinusoidal surface acts like a phase grating that modulates the phase of the sinusoidal irradiance pattern (the carrier frequency). The depth of

modulation is determined by the ratio of surface amplitude to the effective wavelength. We call this the phase contrast, and it is written as

$$m = 2\pi \cdot \frac{A}{\lambda_{eff}}. \tag{5-5}$$

We can further analyze the irradiance map by converting the sine function to its exponential equivalent, i.e.

$$\begin{aligned} I(x,y) = I_0 + \frac{I_1}{2}\exp\left[i2\pi f_{carrier}x + im \cdot sin\left(2\pi f_{surf}x\right)\right] \\ + \frac{I_1}{2}\exp\left[-i2\pi f_{carrier}x - im \cdot sin\left(2\pi f_{surf}x\right)\right]. \end{aligned} \tag{5-6}$$

Using the mathematical properties of the Bessel function, this equation can also be expressed as

$$\begin{aligned} I(x,y) = I_0 + \frac{I_1}{2}\sum_{q=-\infty}^{+\infty} J_q(m)\exp[\, i2\pi f_{carrier}x + iq \cdot 2\pi f_{surf}x] \\ + \frac{I_1}{2}\sum_{q=-\infty}^{+\infty} J_q(m)\exp[\, -i2\pi f_{carrier}x + iq \cdot 2\pi f_{surf}x], \end{aligned} \tag{5-7}$$

where J_q is the Bessel function of the 1st kind at the q-th order. In the phase grating analogy, the q subscripts are the diffraction orders. Notice the amplitude of each "diffraction" order in our equation is directly related to the phase contrast, m. A bigger phase contrast yields a bigger amplitude of the "diffraction" orders. From the equation, we also find the spatial frequencies of the "diffraction" orders are

$$f_d = q \cdot f_{surf} \pm f_{carrier} \;\; (q = 1,2,3 \ldots). \tag{5-8}$$

Each "diffraction" order has two peaks shifted by $\pm f_{carrier}$ from the center frequency, $q \cdot f_{surf}$. This is due to the orientation of the sinusoidal surface that is parallel to the fringe direction.

In this case, both the fringes and the sinusoidal surface are along the x-axis. If the direction of sinusoidal surface is perpendicular to the fringe pattern, the irradiance map is expressed as

$$I(x,y) = I_0 + \frac{I_1}{2}\sum_{q=-\infty}^{+\infty} J_q(m)\exp[\, i2\pi f_{carrier} y + iq \cdot 2\pi f_{surf} x] + \frac{I_1}{2}\sum_{q=-\infty}^{+\infty} J_q(m)\exp[\, -i2\pi f_{carrier} y + iq \cdot 2\pi f_{surf} x]. \quad (5\text{-}9)$$

In this case, the surface sinusoid is along the x-axis, and the fringes are along the y-axis. Therefore, the spatial frequencies of the "diffraction" orders are

$$f_d = q \cdot f_{surf} \;\; (q = 1,2,3 \ldots). \quad (5\text{-}10)$$

In the absence of a point spread function from the imaging system, these surface modulated fringe patterns are simply captured in the image, with at most an overall attenuation, and the measurement remains linear. The nonlinearity comes into play when the MTF limitations of the imaging optical system are considered. A realistic MTF means the amplitude drops for higher-spatial-frequency components of the surface irradiance pattern. When the spatial frequency components of the higher-order "diffraction" frequencies begin to fall at frequencies for which the MTF is significantly low, the system becomes nonlinear.

A simulation of the modulated irradiance patterns on a sinusoidal surface with the spatial frequency of 10 cycles/mm is used to validate the theory. Figure 5-1 shows the fringe pattern with an effective wavelength of λ_{eff} =0.5 mm/cycles on two sinusoidal surfaces. The top graph shows the surface with an amplitude of 10 μm and the bottom graph an amplitude of 50 μm. The graphs to the right show the cross-section irradiance

profiles before (red) and after (blue) the spatial filtering. The spatial filtering of the irradiance patterns is modeled as a convolution of the modulated irradiance pattern with the PSF. The 50-μm surface creates a bigger phase shift; therefore, the system behaves more nonlinear. This is more easily seen in the Fourier spectrum of the irradiance profile as shown in Figure 5-2. The 50-μm surface generates more diffraction orders and a bigger amplitude at each order. The attenuation of diffraction is based on the MTF curve: higher orders attenuate more than lower orders after spatial filtering. Consequently, the reconstructed surface is no longer a pure sinusoidal surface, but a distorted sinusoidal surface with harmonics. If each diffraction order attenuates at the same percentage, the reconstructed surface would have been still a sinusoid. But the MTF causes larger attenuation at the higher orders than at the lower orders. This is the root cause of the nonlinearity in the fringe projection system.

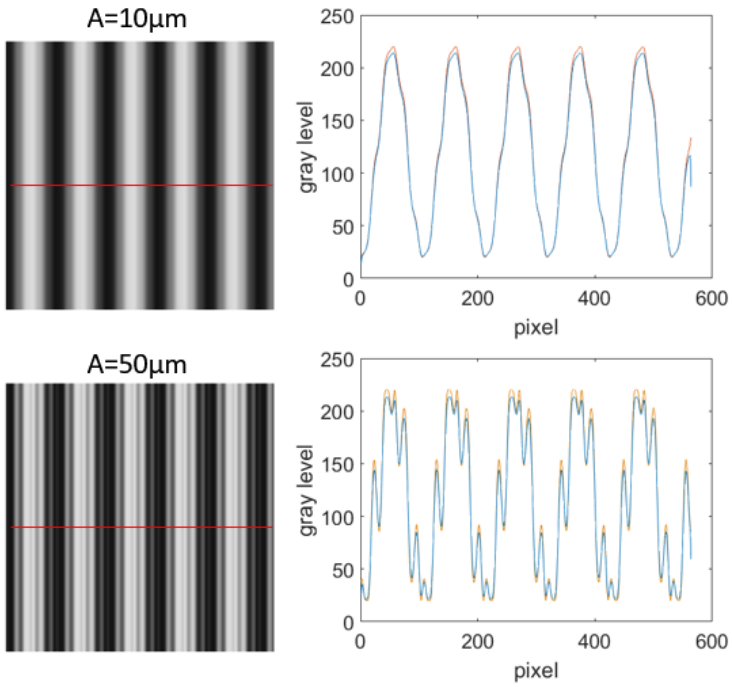

Figure 5-1: Distortion of fringe pattern on sinusoidal surfaces with amplitudes of 10 μm and 50 μm, and the cross-section profiles. The red and blue lines are the irradiance profiles before and after the optical filtering, respectively.

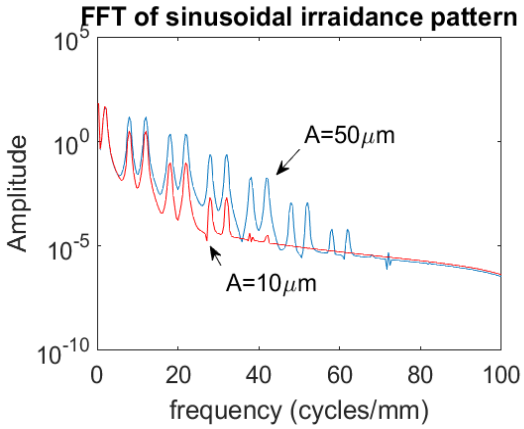

Figure 5-2: Spectrum of a fringe pattern ($f_{carrier}$=2 mm^{-1}) on a sinusoidal surface ($f_{surface}$=10mm^{-1}). The spectrum has split peaks centered at $k \cdot f_{surface}$ (k=0,1,2...) and separated by $\pm f_{carrier}$. A larger surface amplitude generates more peaks.

Rigorously, the system is always nonlinear, but a small amount of distortion in the reconstructed surface can be tolerated – a distortion that is small enough such that the output of a sinusoidal input is close enough to a sinusoid. Therefore, we can define a surface height limit within which the system is still an approximately linear system. If the surface has a small amplitude compared to the effective wavelength, the irradiance map will only have a few diffraction orders which most likely fall in the region where the MTF is close to one. Therefore, the reconstructed surface will be close to a perfect sinusoidal surface. In summary, if all sinusoidal components on the surface are below the height limit, the system can be regarded as an approximately linear system.

The amplitude of each sinusoidal component on the surface is one major factor that determines whether the system is linear. There is an amplitude limit for each sinusoidal component on the surface. Simulation of the measurement of a sinusoidal surface using fringe projection technique shows that the nonlinearity causes the ITF to artificially increase with increasing amplitude. Figure 5-3 shows the ITF as a function of surface amplitude at 10 cycles/mm. Taking a practical approach, we define a height limit within

which the ITF changes less than 1% and call this amplitude the surface height limit for the linear region. The surface height limit varies with spatial frequency. We can calculate the surface height limit through simulation for spatial frequencies up to the cut-off frequency and obtain a curve of the surface height limit. This curve defines the boundary of the amplitude of all sinusoidal components on a surface for the system to behave approximately linear. The region below the curve is called the linear region.

Figure 5-4 shows the surface height limit obtained through simulation. We created a series of sinusoidal surfaces with spatial frequencies 3, 5, 10, 20, 30, 50, 70 and 90 cycles/mm. At each spatial frequency, we started with a very small amplitude of 0.1 μm (in the linear region) and calculated the ITF as the ratio of the amplitude of the measured sinusoid to the amplitude of the input sinusoid. We then increased the amplitude until the ITF was increased by 1% of the smallest ITF. This amplitude is the surface height limit at this spatial frequency. For example, for a 10 cycles/mm sinusoidal surface, the smallest ITF is 0.888 as shown in Figure 5-3. The ITF that is 1% larger than that is 0.897, which corresponds to an amplitude of 57 μm. Therefore, the surface height limit at 10 cycles/mm is 57 μm.

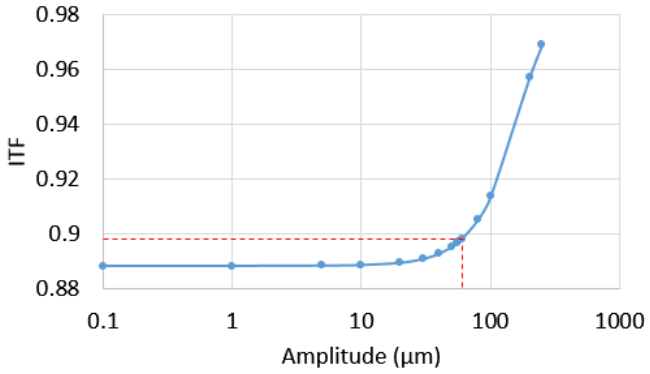

Figure 5-3: ITF calculated on a 10-cycles/mm sinusoidal surface through simulations. The ITF is increased by 1% at the height amplitude of 57 μm corresponding to an approximate linearity limit.

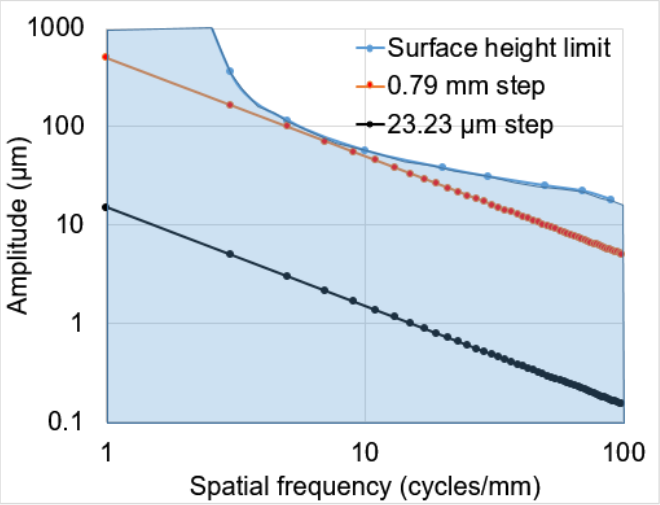

Figure 5-4: An approximate linear region calculated through simulations, and the spatial frequency contents of two stepped surfaces.

The surface height limit curve is important for selecting a proper artifact for measuring the ITF. All sinusoidal components on a surface must be below this curve to meet the linearity conditions. We rarely see any surface with a constant amplitude for all spatial frequencies; it is generally not common for the high-spatial-frequency components to have the same or bigger amplitude than the low-spatial-frequency components. Most surfaces have smaller amplitudes for higher spatial-frequency components. An example of this surface is a stepped surface. Mathematically, a stepped surface has infinite spatial frequency components, and the amplitude of each sinusoidal component is inversely proportional to the spatial frequency. Figure 5-4 shows the spectra of a 0.79-mm stepped surface and a 23.23-μm stepped surface. The 0.79-mm step has a spatial frequency curve right below the surface height limit, while the curve for the 23.23-μm step is far below the surface height limit curve. The 23.23-μm step artifact is readily available on campus so it is what we used to make the ITF measurements. Since the amplitude of the 23.23-μm step is far smaller for all spatial frequencies than the surface height limit, the system will behave

close to a linear system. However, a drawback of using such a small step height is that the signal-to-noise ratio will be low.

The geometric linearity constraint is negligible in the high-spatial-frequency region because the amplitude of high-spatial-frequency components is typically much smaller than the amplitude of the low-spatial-frequency components, and of course much smaller than the working distance. It is highly unlikely for a surface to have high-spatial-frequency sinusoids with a large amplitude that breaks the geometric linearity constraint. The geometric linearity constraint becomes significant in the low-spatial-frequency region. Generally, low spatial frequency components on a surface (less than $1/\lambda_{eff}$) are less subject to the surface height limit constraint, because the harmonics of a low spatial frequency on a surface are very close to the carrier frequency of the irradiance pattern and not impacted significantly by the MTF. But a low-spatial-frequency sinusoid can have a large amplitude that is not negligible compared to the working distance, violating the geometric linearity constraint and breaking the system linearity because the phase to height conversion is no longer linear.

Selection of the effective wavelength also has an impact on the surface height limit. If the system uses a different effective wavelength, it will have a different surface height limit. Decreasing the effective wavelength increases the sensitivity of the system, but leads to tighter constraints of the linear region (smaller surface height limit). Smaller effective wavelength is usually used to measure high-spatial-frequency features which typically have a small amplitude. However, if we choose to continue decreasing the effective wavelength, it will eventually reach a lower bound of measurability which is limited by the spatial sampling of the digital sensor array. A rule of thumb is to keep the fringe period

larger than ten times the digital sensor sampling interval. A shorter fringe period will correspond to insufficient sampling and cause errors. On the other hand, increasing the effective wavelength will extend the surface height limit, but it decreases the phase contrast, decreasing the signal to noise ratio. Decreasing the phase contrast reduces the number of diffraction orders, leading to an expansion of the linear region.

5.2.3 ITF Measurement Methodology

The key to measuring the ITF is finding the right artifact. Such an artifact should have the two following features: 1) it should contain a wide spatial frequency band that suits the measurement principle, i.e. 1 to 100 cycles/mm; 2) the amplitudes of the sinusoidal components on the surface are under the linear surface height limit, but are large compared to the typical measurement noise of the system. It is not necessary to use a single-frequency sinusoidal surface to measure the ITF at each spatial frequency. Sinusoidal surfaces are expensive to manufacture, and measuring the complete spatial frequency band of the ITF curve would require many sinusoidal surfaces [116]. Perhaps, one may think of a chirped sinusoidal surface because of its continuously varying spatial frequency band. However, such a surface usually has a small amplitude, typically a few micrometers for all spatial frequencies. This amplitude is too small for the fringe projection system because the typical measurement noise is at the same magnitude, if not bigger.

A stepped surface is a superior choice than the two surfaces mentioned above. A stepped surface is relatively less expensive to fabricate, and it contains a wide spatial frequency band for an ITF measurement. A mathematically perfect step has an amplitude that is inversely proportional to the spatial frequency. However, the sharpness of the step

edge decides how close the spatial frequency components of a real step edge to the theoretical formula. A rounded step edge has reduced amplitudes at high-spatial-frequency range compared to a mathematically perfect step. Fortunately, the step edge doesn't have to be perfectly sharp for a sensible ITF measurement, but the spatial frequency components below the cut-off frequency must follow the theoretical formula.

Once the stepped surface is measured, a profile across the step is extracted to calculate the ITF. There are two ways to analyze the measured step profile and to calculate the ITF. The first approach is to compute the ratio of the Fourier transform of the measured step profile to the mathematically perfect step profile (Equation 5-3), or equivalently to calculate the ratio of the square roots of the power spectral density (PSD) functions of the measured and the mathematically perfect step profiles [117]. However, due to the nature of the discrete Fourier transform (DFT), also called the fast Fourier transform (FFT), which extends the sample length by duplicating the sample itself before calculating the Fourier transform, the connection of the two ends of the sample must be continuous. This is apparently not true for the step profile; however, one can circumvent this problem by duplicating and folding the step profile about the vertical axis, forming an artificial measurement of a double-sided step profile. The second approach is to calculate the FFT of the line spread function (the derivative of the measured step profile). This method is a standard for MTF measurement of a digital imaging device and it is well documented in ISO 1223 standards [118]–[122]. The principle of using the derivative of a step profile to measure the ITF is described as follows.

The input function, the step function, is written as

$$f(x) = step(x). \tag{5-11}$$

The output, or the measured step function, is the input function convolved with the impulse response as expressed in Equation 5-1. Then, the derivative of the measured step function is calculated as

$$\frac{d}{dx}g(x) = \frac{d}{dx}[step(x) \otimes h(x)] = \left[\frac{d}{d}step(x)\right] \otimes h(x) = \delta(x) \otimes h(x). \qquad (5\text{-}12)$$

Since the Fourier transform of the delta function equals one, and the Fourier transform of a convolution is a dot product, taking the Fourier transform of both sides of this equation gives the ITF,

$$F.T.\left[\frac{d}{dx}g(x)\right] = H(f). \qquad (5\text{-}13)$$

Until now, we have introduced the definition of ITF and the methods of calculating ITF. Later, we will reveal another finding of this research, that is the ITF is indirectly connected with the MTF. This connection will be discussed in Section 5.2.5, but first, we need to discuss the camera MTF model.

5.2.4 Camera MTF Model

The MTF is defined as the contrast of the image as a function of spatial frequency. The MTF of a digital camera is determined by optical diffraction, aberrations, the detector footprint and the sampling interval [115]. The total camera MTF is the product of the MTF of each subsystem and is written as

$$MTF_{camera} = MTF_{diffraction} \cdot MTF_{footprint} \cdot MTF_{sampling} \qquad (5\text{-}14)$$

The diffraction-limited MTF of a circular-aperture optical system is expressed as

$$MTF_{Diffraction}\left(\frac{f}{f_{cutoff}}\right) = \frac{2}{\pi}\left[cos^{-1}\left(\frac{f}{f_{cutoff}}\right) - \frac{f}{f_{cutoff}}\sqrt{1 - \left(\frac{f}{f_{cutoff}}\right)^2}\right] \qquad (5\text{-}15)$$

where f_{cutoff} is the cut-off frequency and is determined by the working f-number and the wavelength,

$$f_{cutoff} = \frac{1}{\lambda \cdot (f/\#)}. \quad (5\text{-}16)$$

The f-number shown on the camera lens is, by default, the infinite conjugate f-number, meaning the working f-number when the object is placed at an infinite distance from the camera. The image, in this case, is at the back focal plane. The infinite conjugate f-number is defined as the ratio of the effective focal length to the diameter of the entrance pupil. For our fringe projection system, the camera is placed at a finite distance from the object; therefore, the working f-number is different from the infinite conjugate f-number. The relationships between the working f-number and the infinite conjugate f-number is

$$(f/\#)_{img} = (1 - m) \cdot f/\#\,, and \quad (5\text{-}17\ a)$$

$$(f/\#)_{obj} = \frac{1 - m}{-m} \cdot f/\# \quad (5\text{-}17\ b)$$

where $(f/\#)_{img}$ is the working f-number in the image space, $(f/\#)_{obj}$ is the working f-number in the object space, and m is the magnification of the lens [123]. Figure 5-5 shows the geometric configurations for the infinite conjugate f-number and the finite distance working f-number. If the infinite conjugate f-number is 10 and the magnification of the camera is -1.09, the working f-number in the object space is $(f/\#)_{obj}$=(1+0.91)/0.91×10=21.

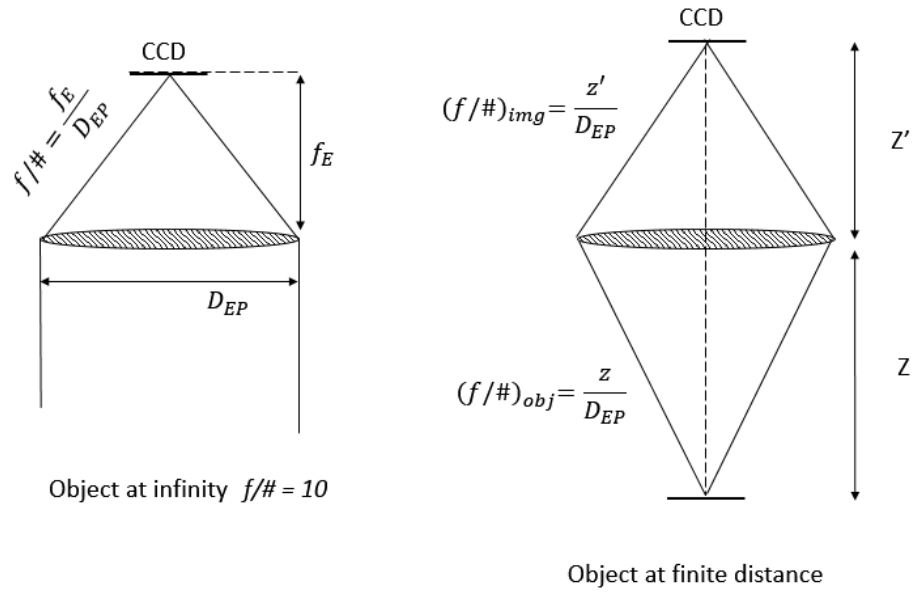

Figure 5-5: Infinite conjugate f-number (left) compared with working f-number (right).

The pixel footprint is the projection of a camera pixel in object space. The pixel footprint has the effect of averaging the radiation emitted over the projected pixel area. A square pixel can be mathematically described as a rectangular function; therefore, the MTF of the pixel footprint is the Fourier transform of the rectangular function, namely the absolute value of the sinc function. The equation of the pixel footprint MTF is given as

$$MTF_{footprint}(f) = |\mathrm{sinc}(w \cdot f)| \tag{5-18}$$

where *w* is the width of the pixel footprint.

The spatial sampling of the digital detector array, or the charge-coupled device (CCD), also impacts the camera MTF. A digital imaging device is not a shift-invariant system, meaning the location of the image on the CCD will affect the image quality. Imagine an image of a straight line that is aligned with one column of pixels; the produced signal will be narrow and strong. On the other hand, if the line image falls between two columns of pixels, the corresponding signal will be broad and weak. This indicates that the camera has

a different MTF depending on where the image is located with respect to the spatial sampling sites on the CCD. The shift variance inherently prevents the use of the transfer function as an image analysis tool. To preserve the transfer function approach, we need to find a shift-invariant MTF which considers the spatial sampling effect. The solution is to model the sampling effect into the MTF. This sampling MTF equals the average of all the MTFs when a sensor is imaged with all possible alignments. The sampling MTF is expressed as

$$MTF_{sampling}(f) = \left|\mathrm{sinc}(x_{sampling} \cdot f)\right| \tag{5-19}$$

where the variable $x_{sampling}$ denotes the sampling interval [115].

In general, the CCD pixels don't have to be contiguous; a sparse pixel arrangement is also possible. For the case which the pixels are contiguous, the pixel footprint is equal to the sampling interval, therefore the footprint MTF is equal to the sampling MTF.

Figure 5-6 shows the theoretical camera MTF and the MTF components. The optical diffraction limit MTF is governed by the working f-number as expressed by Equation 5-8 and 5-9. The working f-number in object space is a function of the camera magnification and the infinite conjugate f-number as expressed by Equation 5-17 (b). The camera magnification is measured by imaging a ruler and calculating the pixel size in object space (the pixel footprint). The ratio of the pixel size at the detector plane (4.3 μm) and the pixel footprint in object space (4.7 μm) gives the magnification (-4.3/4.7=-0.91). Knowing the infinite conjugate f-number (*f/#*=10), the working f-number in object space is $(f/\#)_{obj}$=(1+0.91)/0.91×10=21. Thus, the cut-off frequency due to optical diffraction is f_{cutoff}=1/(0.5[μm]×21)=95 cycles/mm.

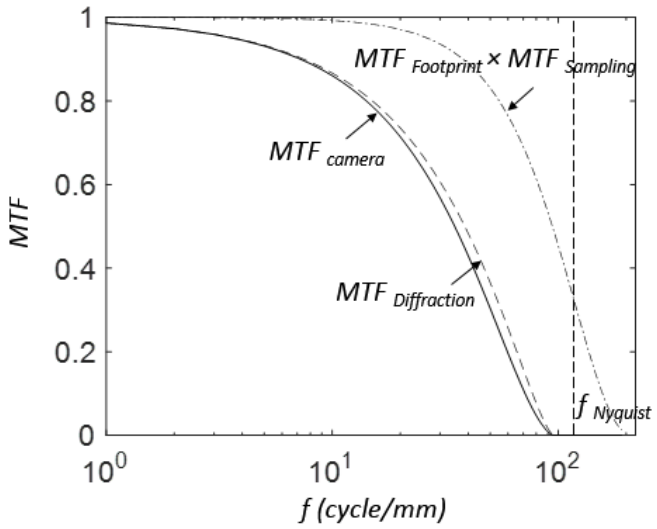

Figure 5-6: Diffraction-limit MTF, sampling MTF, pixel footprint MTF and total MTF.

The MTFs of the pixel footprint and the sampling are given by Equation 5-18 and 5-19. Since the pixel footprint and the sampling interval are the same, the combined MTF due to the two contributors is the square of the sinc function as shown in Figure 5-7. The cut-off frequency of the pixel footprint and the sampling is $f_{cut\text{-}off}$ =1/4.7μm=213 cycles/mm. Thus, the Nyquist frequency is half of the sampling frequency, f_{Nquist} =106 cycles/mm.

5.2.5 Relationship between ITF and MTF

Optical filtering is the root cause of dropping amplitude with spatial frequency in ITF. If the acquired images are not optically filtered, the ITF will remain at one for all spatial frequencies. The MTF describes the low-pass filtering effect of the camera hardware (including the optics and the sensor array) on the acquired irradiance maps. A fringe projection measurement has a similar filtering effect on the measured topography maps, and it is related to the camera MTF. The images acquired by the camera have a reduced

grayscale visibility at the high-spatial-frequency regions on the surface. The visibility of the carrier fringes does not decrease because the carrier frequency is at the far-left end of the MTF curve. Although the phase shifting algorithm is not sensitive to the amplitude of the modulation, the apparent phase shift caused by the surface variations will be affected by the decreased MTF irradiance modulation. The reduced irradiance modulation will effectively reduce the relative phase difference between adjacent pixels, therefore, reducing the height amplitude for that frequency. The spatial frequencies beyond the MTF cut-off frequency have no grayscale modulation; therefore, the fringe projection measurement cannot determine a phase for these frequencies and therefore cannot deliver a height amplitude for these frequencies. While not exactly the same, the ITF can be understood as a consequence of the MTF of the camera, and this connection can be understood by breaking the fringe projection measurement into the basic components.

The analysis begins with understanding how the surface variations is measured from the deformation of the sinusoidal fringe pattern. The surface variation causes deformation of the sinusoidal irradiance map, equivalently a shift in phase of the carrier fringes. The underlying phase map is the addition of the object phase map and the carrier phase map. Thus, the deformed fringe pattern can be expressed as

$$I_i(x,y) = I_0 + I_1 sin(\varphi_{obj}(x,y) + \varphi_{carrier}(x,y) + \delta_i) \tag{5-20}$$

where I_0 is the average irradiance, I_1 is the amplitude of the irradiance modulation, φ_{obj} is the object phase map, $\varphi_{carrier}$ is the carrier phase map, and δ_i is the phase stepping constant (refer to Equation 2-8). The object phase map is a function of the effective wavelength and the height map, and it is expressed as

$$\varphi_{obj}(x,y) = \frac{2\pi}{\lambda_{eff}} height(x,y). \tag{5-21}$$

Assuming the fringe is along the x-axis, the carrier phase map is written as

$$\varphi_{carrier}(x,y) = \frac{2\pi}{p} x\,, \tag{5-22}$$

where *p* is the fringe pitch. The acquired fringe images are optically filtered, and the spatial filtering process can be modeled as the convolution of the deformed fringe image and the PSF of the camera, namely

$$I_{i,blurred}(x,y) = I_i(x,y) \otimes PSF. \tag{5-23}$$

Because the filtered images lose high-spatial-frequency content, the acquired images are blurred compared to the actual irradiance map on the surface. The blurred images are then used to calculated the phase map through the least-square phase shifting algorithm [89], and the resulting wrapped phase map is

$$\varphi'(x,y) = arctan\left(\frac{-\sum_{i=1}^{N} \sin(\delta_i)\, I_i(x,y) \otimes PSF}{\sum_{i=1}^{N} \cos(\delta_i)\, I_i(x,y) \otimes PSF}\right). \tag{5-24}$$

where *N* is the number of buckets used for the phase shifting algorithm. The prime is used to denote the reconstructed phase. Substituting Equation 5-20 into Equation 5-24, and applying the four-step phase-shifting algorithm, the measured phase map is simplified as

$$\varphi'(x,y) = arctan\left(\frac{\sin\varphi(x,y) \otimes PSF}{\cos\varphi(x,y) \otimes PSF}\right), \tag{5-25}$$

where *φ(x,y)* is the wrapped true phase map which contains both the object phase map and the carrier phase map, namely

$$\varphi(x,y) = \varphi_{obj}(x,y) + \varphi_{carrier}(x,y)\,. \tag{5-26}$$

For clarity, the phase location *(x,y)* will be omitted in the equations. Thus, the measured phase map can also be written as

$$tan\varphi' = \frac{\sin(\varphi_{obj} + \varphi_{carrier}) \otimes PSF}{\cos(\varphi_{obj} + \varphi_{carrier}) \otimes PSF}. \quad (5\text{-}27)$$

This equation can be further simplified as

$$\begin{aligned} tan\varphi' &= \frac{sin(\varphi_{obj} + \varphi_{carrier}) \otimes PSF}{cos(\varphi_{obj} + \varphi_{carrier}) \otimes PSF} \\ &= \frac{(sin\,\varphi_{obj}\, cos\varphi_{carrier} + sin\varphi_{carrier}\, cos\varphi_{obj}) \otimes PSF}{(cos\,\varphi_{obj}\, cos\varphi_{carrier} - sin\varphi_{carrier}\, sin\varphi_{obj}) \otimes PSF} \\ &= \frac{\varphi_{obj}\, cos\varphi_{carrier} \otimes PSF + sin\varphi_{carrier} \otimes PSF}{cos\varphi_{carrier} \otimes PSF - \varphi_{obj} sin\varphi_{carrier} \otimes PSF} \\ &= \frac{sin\varphi_{carrier} + (\varphi_{obj}\, cos\varphi_{carrier}) \otimes PSF}{cos\varphi_{carrier} - (\varphi_{obj}\, sin\varphi_{carrier}) \otimes PSF}. \end{aligned} \quad (5\text{-}28)$$

In this equation, we made a small angle approximation, i.e. $sin(\varphi_{obj}) \approx \varphi_{obj}$ and $cos(\varphi_{obj}) \approx 1$, by assuming the surface deviation is much smaller than the effective wavelength ($height(x,y) << \lambda_{eff}$). Note that the convolution of the carrier sine wave with a symmetric PSF only decreases the amplitude, and when the width of the PSD is much smaller than the carrier wavelength, the amplitude does not decrease after the convolution, namely $sin\varphi_{carrier} \otimes PSF = sin\varphi_{carrier}$ and $cos\varphi_{carrier} \otimes PSF = cos\varphi_{carrier}$.

There is one critical step of the derivation remaining – showing that the convolution of the PSF with the product of the object phase map and the carrier irradiance map is approximately equal to the product of the carrier irradiance map and the convolution of the object phase map with the PSF, namely

$$(\varphi_{obj}\, cos\varphi_{carrier}) \otimes PSF \approx (\varphi_{obj} \otimes PSF) cos\varphi_{carrier}. \quad (5\text{-}29)$$

This approximation stands under the condition that the width of the PSF is much smaller than the carrier wavelength, meaning $cos(\varphi_{carrier})$ can be regarded as a constant over the

spread of the PSF. The extreme case would be where the carrier wavelength is infinite; therefore, $cos(\varphi_{carrier})$ equals a constant. Substitute this equation to Equation 5-28, we have

$$\begin{aligned} tan\varphi' &= \frac{sin\varphi_{carrier} + (\varphi_{obj}\, cos\varphi_{carrier}) \otimes PSF}{cos\varphi_{carrier} - (\varphi_{obj}\, sin\varphi_{carrier}) \otimes PSF} \\ &\approx \frac{sin\varphi_{carrier} + (\varphi_{obj} \otimes PSF)\, cos\varphi_{carrier}}{cos\varphi_{carrier} - (\varphi_{obj} \otimes PSF)\, sin\varphi_{carrier}} \\ &\approx \frac{sin\varphi_{carrier}\cos(\varphi_{obj} \otimes PSF) + \sin(\varphi_{obj} \otimes PSF)\, cos\varphi_{carrier}}{cos\varphi_{carrier}\cos(\varphi_{obj} \otimes PSF) - \sin(\varphi_{obj} \otimes PSF)\, sin\varphi_{carrier}} \\ &= \frac{\sin(\varphi_{obj} \otimes PSF + \varphi_{carrier})}{cos\big(\varphi_{obj} \otimes PSF + \varphi_{carrier}\big)} \\ &= \tan\big(\varphi_{obj} \otimes PSF + \varphi_{carrier}\big). \end{aligned} \tag{5-30}$$

In this derivation, we again use the approximation that $\varphi_{obj} \otimes PSF \approx \sin(\varphi_{obj} \otimes PSF)$ and $cos(\varphi_{obj} \otimes PSF) \approx 1$ in the limit the object phase is very small compared to the effective wavelength. From this equation, we can draw the conclusion that the measured phase is approximately equal to the sum of the carrier phase and the convolution of the object phase with the PSF, namely

$$\varphi' \approx \varphi_{carrier} + \varphi_{obj} \otimes PSF. \tag{5-31}$$

The carrier phase is removed from Equation 5-31 with subtraction of the tilt in the measured phase map. What remains can then be written as

$$\varphi'_{obj}(x, y) \approx \varphi_{obj}(x, y) \otimes PSF. \tag{5-32}$$

Since the height map is linearly proportional to the object phase map when geometric linearity condition is satisfied, this equation can also be written as

$$h'_{obj}(x, y) \approx h_{obj}(x, y) \otimes PSF. \tag{5-33}$$

This equation means that the measured object height map is approximately the convolution of the actual object height map and the PSF under the conditions that 1) the surface deviation is much smaller than the effective wavelength, and 2) the width of the PSF is much smaller than the fringe wavelength. Also in the spatial frequency domain, the ITF will be similar to the MTF when these two conditions are satisfied. This can be mathematically demonstrated as

$$ITF = \frac{FT\left(h'_{obj}\right)}{FT\left(h_{obj}\right)} \approx \frac{FT\left(h_{obj}\right) \cdot FT(PSF)}{FT\left(h_{obj}\right)} = MTF. \quad (5\text{-}34)$$

5.3 ITF Simulation

Matlab is a useful platform for simulation of fringe projection measurements which can be used to calculate ITF. Simulation is a great approach to validate the system's linearity and to compare the ITF with the MTF. As discussed previously, a linear system is surface independent and its ITF is approximately equal to the MTF of the camera. Based on this, we conduct a simulation study with several different types of surfaces and compare the resulting ITF curves. We assume the geometric linearity condition is met by making the height proportional to the phase shift, and the camera is perpendicular to the surface so that the perspective distortion is not considered, nor is shadowing and pixel saturation. The system parameters used in the simulation are similar to the operational parameters of the experiment, namely an object-space working f-number of 21, an object-space pixel footprint/sampling interval of 4.7 μm and an effective wavelength of 0.5 mm/cycle. This gives an optical cut-off frequency of approximately 95 cycles/mm, meaning the spatial frequency of the sample surfaces should be less than this frequency.

The basic principle of the simulation is to create a sinusoidal irradiance pattern on the computer-generated surfaces and to include the optical filtering effect by calculating the convolution of the irradiance map with the PSF. These filtered irradiance maps are then used to create a simulation of the "measured" surface through the phase shifting algorithm. Finally, the ITF is calculated by comparing the amplitudes of the spatial frequency components of the "measured" surface to those of the actual surface.

5.3.1 ITF Simulation with Sinusoidal Surfaces

The simplicity of sinusoidal surfaces provides a useful way to test the linearity of a system, but measuring the ITF on sinusoidal surfaces experimentally is impractical because it requires too many samples. However, numerical measurement simulations of many sinusoidal surfaces can be easily done. To measure the complete spectrum (up to the cut-off frequency) of the ITF, we generated a series of sinusoidal surfaces from 5 to 95 cycles/mm with an increment of 5 cycles/mm. The amplitude of these sinusoidal surfaces is 10 μm, and it satisfies the linearity conditions. The unfiltered irradiance map is expressed as Equation 5-20. Figure 5-7 shows the simulation of a sinusoidal fringe pattern on a 1×1 mm^2 sinusoidal surface with a spatial frequency of 10 cycles/mm. Notice the small ripples on the fringe pattern are due to the fringe modulation caused by the surface variations.

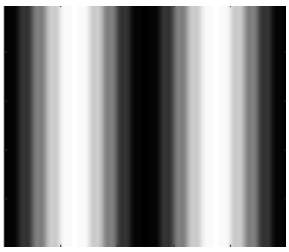

Figure 5-7: Computer-generated sinusoidal irradiance map ($f_{carrier}$=2 cycles/mm) on a sinusoidal surface ($f_{surface}$=10 cycles/mm).

Assuming the PSF is circularly symmetric, the 2D PSF is computed as the inverse Fourier transform of the theoretical MTF. The optical filtering process is simulated as the convolution of the unfiltered irradiance map with the PSF as shown in Figure 5-8. The image area is 5 × 5 mm^2. The resulting irradiance map is blurred where the visibility[1] of each spatial frequency component decreases based on the MTF curve. Since the carrier fringes only have a spatial frequency of 2 cycles/mm, its visibility does not decrease. The fringe modulation caused by the surface variations has a higher spatial frequency; therefore, the visibility of the fringe modulation decreases with the spatial filtering. The higher the spatial frequency is, the more decrease in the visibility.

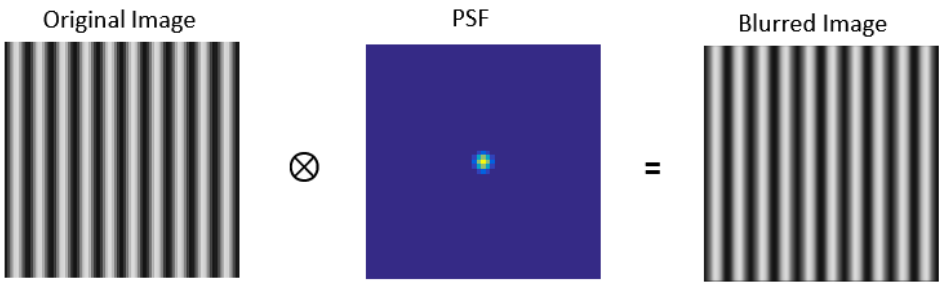

Figure 5-8: The optical filtering process on the 10-cycles/mm sinusoidal surface is modeled as the convolution of the irradiance map and the PSF.

The blurred irradiance maps are then used to generate a simulation of the "measured" surface through the phase shifting algorithm. Figure 5-9 shows the "measured" sinusoidal profile compared to the actual sinusoidal profile. The amplitude of the "measured" sinusoidal surfaces is measured directly from the "measured" profile. This "measured" amplitude is 9.1 μm, smaller than the actual amplitude of 10 μm. The ratio of the two amplitude values is the ITF at this frequency, namely *ITF* (*f*=10cycles/mm) =0.91.

[1] Visibility is defined as $V=(I_1-I_2)/(I_1+I_2)$, where I_1 is the maximum irradiance and I_2 is the minimum irradiance.

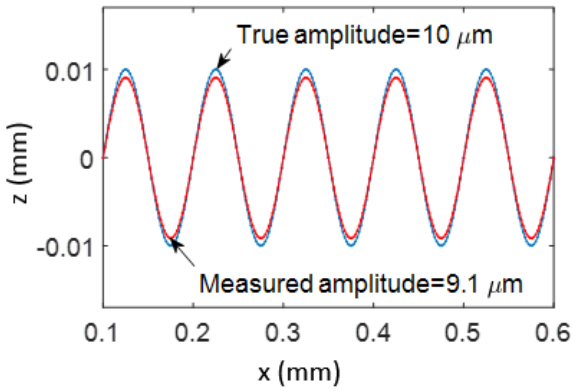

Figure 5-9: Comparison of the measured sinusoidal profile and the actual sinusoidal profile.

To complete the ITF curve, the simulation is repeated over a range of spatial frequencies. Figure 5-10 shows the simulated ITF curve compared with the theoretical MTF curve. Since the amplitude of the surface is small compared to the effective wavelength, the ITF curve is expected to be approximately equal to the MTF curve as discussed previously. We also computed the ITF curve through simulation where the sinusoidal surface is placed perpendicular to the fringe direction. The simulation result shows the same ITF curve, indicating the ITF does not change when the orientation of the surface frequencies changes relative to the carrier fringe orientation.

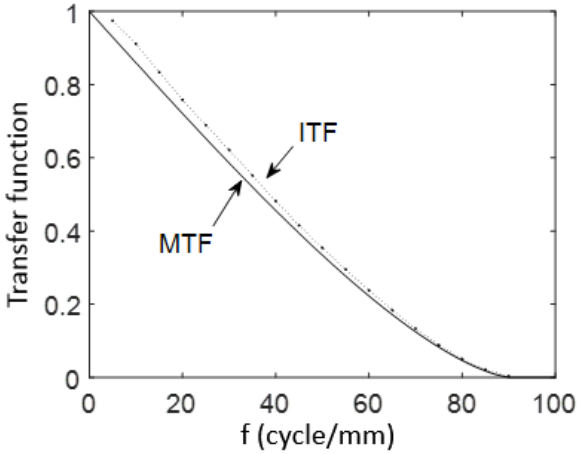

Figure 5-10: The ITF curve calculated with the simulation of fringe projection measurements on a series of sinusoidal surfaces and the theoretical MTF curve.

5.3.2 ITF Simulation with a Multi-frequency Surface

For a linear system, the ITF at one spatial frequency is not affected by other spatial frequencies, i.e. the ITF is independent of the surface type. This can be tested by introducing more spatial frequency components to the surface. A multi-frequency surface is a surface which consists of many spatial frequency components. To generate such a surface, a series of sinusoidal components with spatial frequencies of 2, 4, 8, 10, 20, 25, 40, 50 and 100 cycles/mm are created and combined together. These spatial frequencies contain an integer number of the wavelength for a sample length of 4 mm. This avoids the complication arising from the boundary discontinuity in the FFT computation. The amplitude of each sine wave is inversely proportional to the spatial frequency, namely 0.05mm/spatial frequency. This amplitude satisfies the linearity conditions. The initial phase of each sine wave is set to a random value. Figure 5-11 shows the computer-generated multi-frequency surface and a line profile along the x-axis. The surface is 4 mm long and 3 mm wide. The peak-to-valley deviation of the surface is about 40 μm.

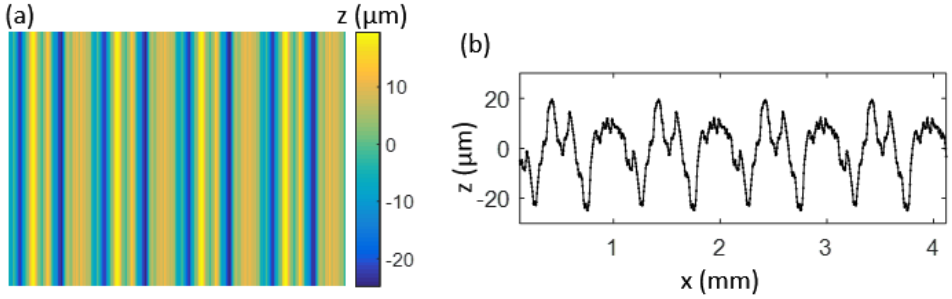

Figure 5-11: The ITF simulation of a multi-frequency surface. (a) The height map of the multi-frequency surface and (b) the profile of the surface along the x-axis.

Knowing the exact spatial frequencies and their amplitude on the computer-generated surface, we create the distorted irradiance maps based on Equation 5-20, and then incorporate the optical filtering effect, modeled as the convolution of the distorted

irradiance map with the PSF. Figure 5-12 shows the convolution of the unfiltered irradiance map with the PSF. The subsequent filtered irradiance map is blurred, indicating a decrease in the modulation visibility with increasing spatial frequency.

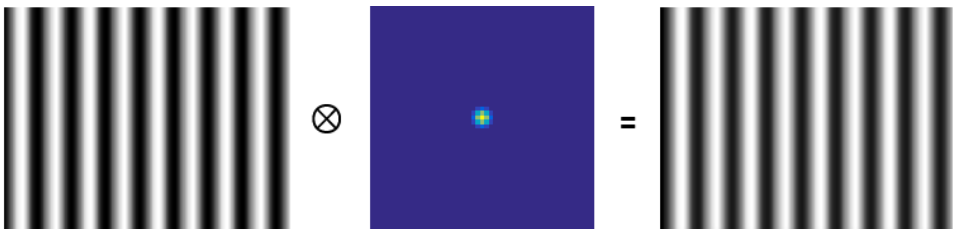

Figure 5-12: Convolution of a distorted irradiance map of a multi-frequency surface with the PSF.

The filtered irradiance maps are then used to generate a simulation of the "measured" surface through the phase shifting algorithm. Unlike the pure sinusoidal surfaces where the amplitude can be directly measured from the graph, the amplitudes of the spatial frequency components on the multi-frequency surface are measured through a Fourier analysis. Figure 5-13 shows the FFTs of both the "measured" surface and the actual surface. For clarity purpose, the FFT of the actual surface is plotted as a dashed line, while the FFT of the "measured" surface is plotted as discrete peaks. The amplitudes of the spatial frequency components are then read from the spectra.

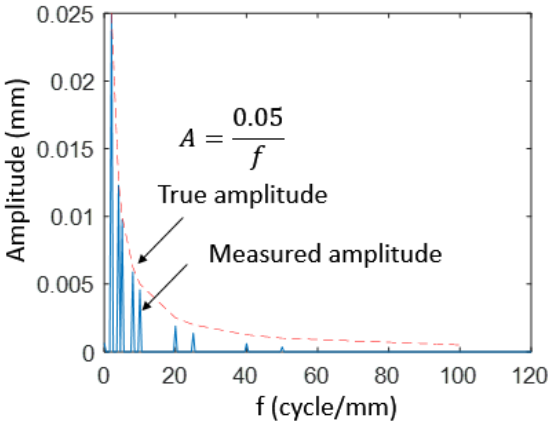

Figure 5-13: FFTs of the reconstructed surface and the actual multi-frequency surface. The dashed line indicates the amplitude at the frequency peaks on the actual surface.

The ITF is then calculated as the ratio of the "measured" amplitude to the actual amplitude. Figure 5-14 shows the IFT curve calculated from the multi-frequency surface compared to the ITF calculated from the pure sinusoidal surfaces. The two ITF curves overlap, indicating that the transfer function of the fringe projection system does not change because of the added spatial frequencies, that the system is approximately linear, and that the IFT is applicable to the fringe projection system.

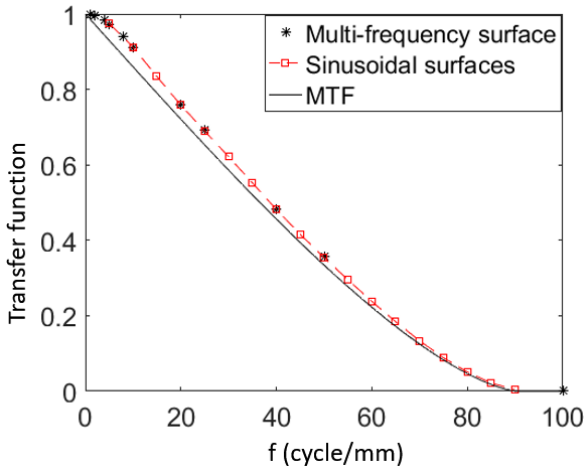

Figure 5-14: Simulation of the ITF (stars) on the multi-frequency surface and the theoretical MTF (solid line).

5.3.3 ITF Simulation with a Stepped Surface

A stepped surface is a special multi-frequency surface. An ideal stepped surface has infinite spatial frequencies and amplitudes that are inversely proportional to the spatial frequency. Figure 5-15 shows a 50-μm stepped surface created by a piecewise function.

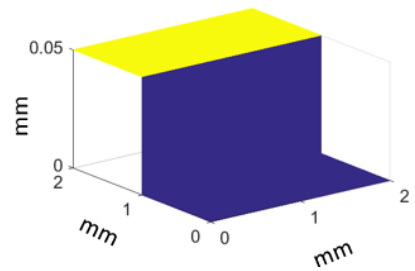

Figure 5-15: A computer-generated 50-μm stepped surface.

To simulate the ITF measurement using the stepped surface, the deformed fringe pattern on the step surface is first generated and then the PSF is created based on the theoretical MTF, where the object-space working f-number is 21 and the pixel footprint/sampling interval is 4.7 μm. Again, the optical filtering process is modeled as the convolution of the unfiltered irradiance map and the PSF. The convolution produces a blurred irradiance map, as shown in Figure 5-16.

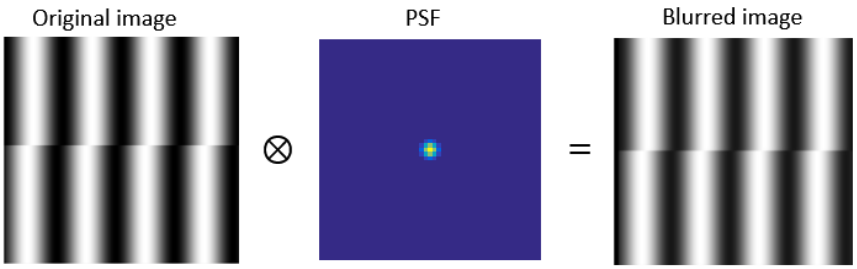

Figure 5-16: Convolution of a fringe pattern on a 50-μm stepped surface and the PSF.

The filtered irradiance maps are then used to generate a "measured" stepped surface through the phase-shifting algorithm. Figure 5-17 (a) shows the "measured" step surface, and Figure 5-17 (b) is a line trace along the x-axis as indicated by the red arrow. Since the surface is noise-free, one profile is sufficient to calculate the ITF. As expected, the "measured" step profile has rounded edges due to the spatial filtering of the system, and the roundness of the edge contains the information we need to calculate the ITF.

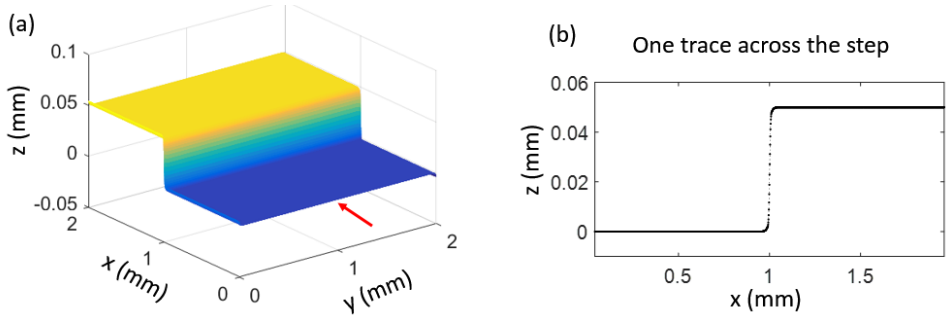

Figure 5-17: Simulation of a step surface. (a) The measured step surface. (b) The profile of the step along the x-axis.

As discussed previously, there are two calculation choices. One calculates the ratio of the Fourier transform of the "measured" step profile to the Fourier transform of the mathematically perfect step profile. The discontinuity of the step is circumvented by duplicating and folding the step profile around the vertical axis, creating an artificial measurement of a double-sided step as shown in Figure 5-18 (a). Then, the Fourier transforms of "measured" and the mathematically perfect step profiles are calculated. The absolute amplitude of the Fourier transform is not important because the two Fourier spectra are generated from the same process, and only the relative amplitude matters. Figure 5-18 (b) shows the Fourier spectra of the "measured" and the mathematically perfect step profiles. As expected, the "measured" step profile has smaller amplitudes than the mathematically perfect step profile. Finally, the ITF is calculated by dividing the Fourier transform of the "measured" step profile by the Fourier transform of the mathematically perfect step profile. The resulting ITF curve is shown in Figure 5-20.

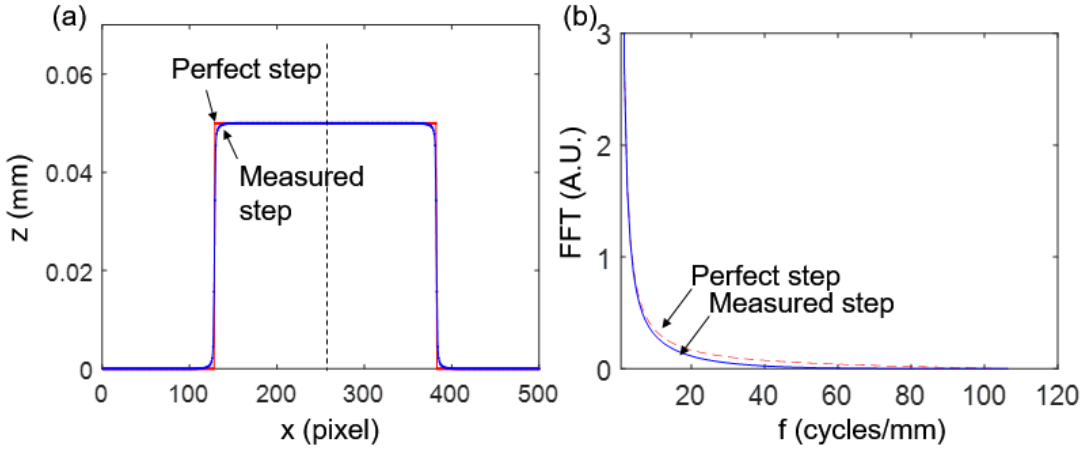

Figure 5-18: Calculating the ITF using the Fourier-transform-ratio method. (a) The "measured" and the mathematically perfect step profiles, both of which are duplicated and folded to create artificial double-sided steps. (b) The Fourier transform of the "measured" step profile and the mathematically perfect step profile.

We also simulate the ITF curve with the LSF approach. The derivative of the measured step, LSF, is first calculated as shown in Figure 5-19. The ITF is then calculated as the Fourier transform of the LSF. The resulting ITF curve is shown in Figure 5-20.

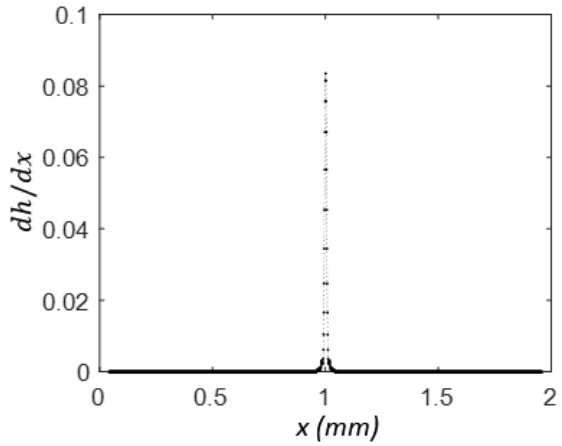

Figure 5-19: Line spread function.

The ITF curves calculated from the two methods are approximately equal, indicating both methods are valid. The MTF curve (dashed line) is also included in the Figure 5-20 for comparison. The ITF curves are approximately equal to but slightly larger than the MTF curve. Although the difference between the ITFs calculated by the two methods is very small, the ITF calculated from the LSF approach is consistently slightly larger than the ITF calculated from the Fourier-transform-ratio approach. The absolute difference of the ITFs obtained by the two approaches is shown in Figure 5-21. The biggest difference is 0.012 at the frequency of around 8.3 cycles/mm.

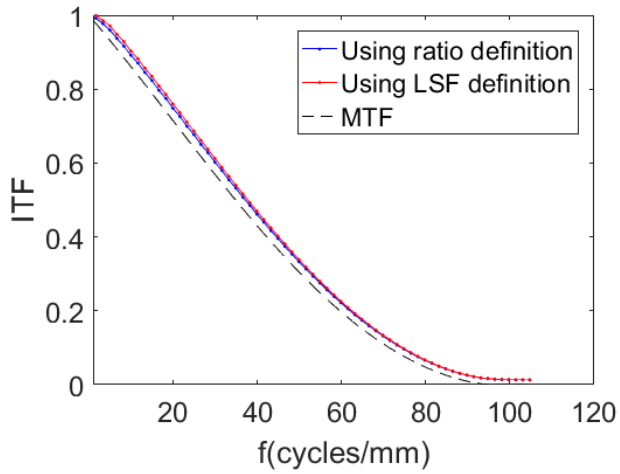

Figure 5-20: Simulation of the ITF from a step height artifact and the theoretical MTF.

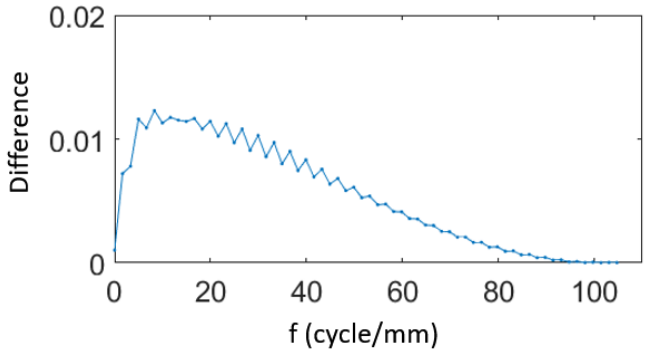

Figure 5-21: Absolute difference between the ITFs calculated with the LSF approach and the Fourier-transform-ratio approach.

Figure 5-22 compares the ITF curves calculated from a stepped surface, pure sinusoidal surfaces, and a multi-frequency surface. The ITF curves calculated from different methods are approximately equal, indicating that the fringe projection system is surface independent. This further means that the fringe projection system is approximately linear and that the use of ITF to characterize its spatial measurement performance is appropriate.

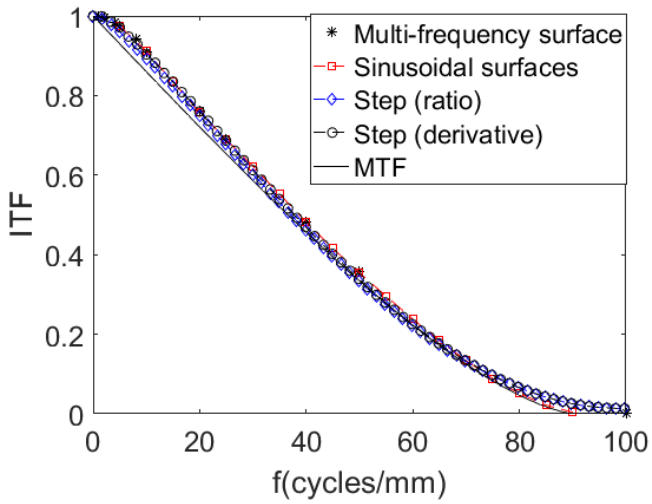

Figure 5-22: Comparison of ITFs calculated through simulations on several types of surfaces.

5.3.4 ITF Simulation with an AM Surface

We also applied the same simulation procedure using a surface topography measurement of an AM surface. We first measured an AM sample with a confocal microscope (Olympus LEXT 4100) which has a cut-off frequency considerably higher than that of the fringe projection system. Figure 5-23 shows this measurement. Even though a confocal microscopy is expected to measure rough surfaces well, measurement of an AM surface is challenging and sensitive to instrument configuration details. Our measurements showed an asymmetry in the surface profile that is not realistic; however, the measured topography should have enough spatial frequency content for a linearity test since the confocal microscope has a high cut-off frequency.

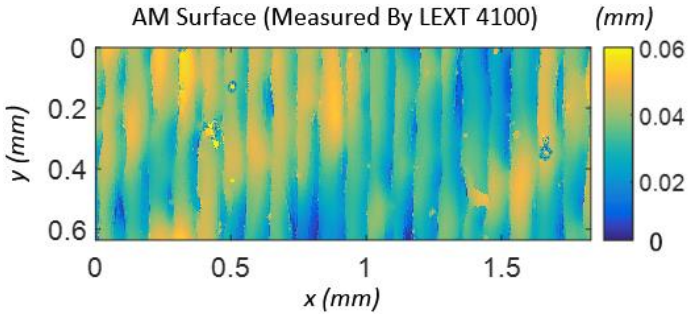

Figure 5-23: A measurement of an AM surface.

The simulation starts with generating a sinusoidal irradiance map on the AM surface based on Equation 5-20. The simulated fringe patterns are shown in Figure 5-24. Again, the optical filtering process is modeled as the convolution of the irradiance map with the PSF created from the theoretical MTF. These filtered irradiance maps are then used to create a simulation of the "measured" surface through the phase shifting algorithm.

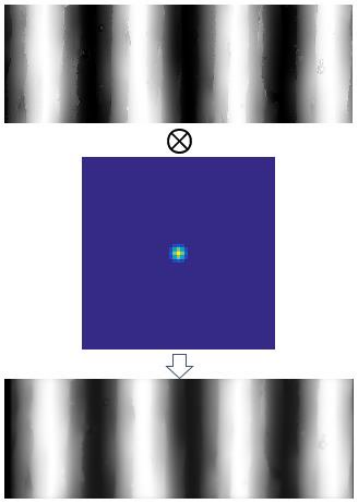

Figure 5-24: Simulation of optical filtering of fringe pattern on an AM surface measurement.

The "measured" surface is then compared with the original surface measurement to calculate the ITF. Figure 5-25 shows the line traces of the "measured" surface and the original surface measurement from the same location. The "measurement" profile is

smoother than the original measurement profile, indicating that the "measured" surface contains filtered amplitudes of the high-spatial-frequency contents of the surface.

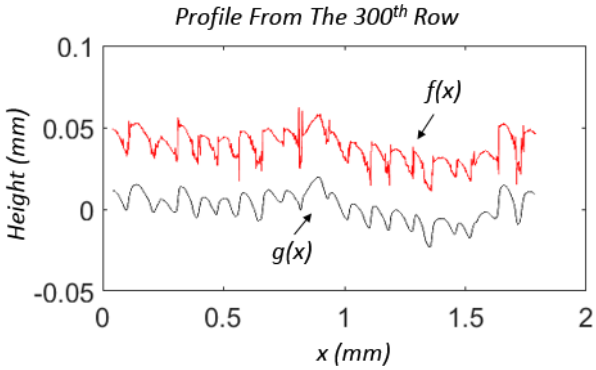

Figure 5-25: Line traces of the "measured" surface (black) and the original surface measurement (red).

A Hann window is applied to both profiles before the FFT calculation to reduce the boundary discontinuity. Figure 5-26 shows the FFTs of the "measured" profile and the original measurement profile. The Fourier spectrum of the "measured" profile has lower amplitudes than the original measurement, indicating the spatial frequency content is filtered.

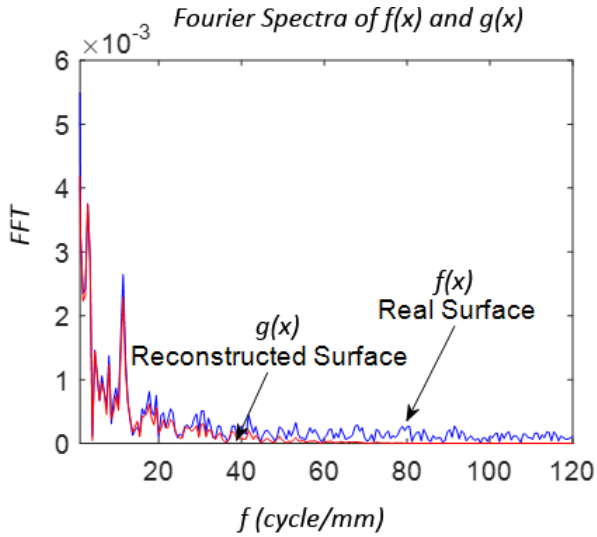

Figure 5-26: Fourier spectra of the "measured" surface and the original surface measurement. A Hann window is applied before the FFT calculation to reduce the discontinuity.

The ITF is then calculated as the ratio of the Fourier transform of the "measured" profile to the Fourier transform the original measurement profile. To reduce the uncertainty, the ITF calculation is repeated on 100 lines from the measurement, and the average of the ITF curves is plotted in Figure 5-27. The ITF curve and the theoretical MTF curve are similar, showing the simulation agrees with the expectation. Unlike all the previous simulations where the ITF curve is consistently slightly higher than the MTF curve, some data points, particularly those above 40 cycles/mm, on the ITF curve obtained with the AM surface fall below the MTF curve. This could be due to an underestimation of the Fourier transform of the measured profile perhaps related to the windowing operation.

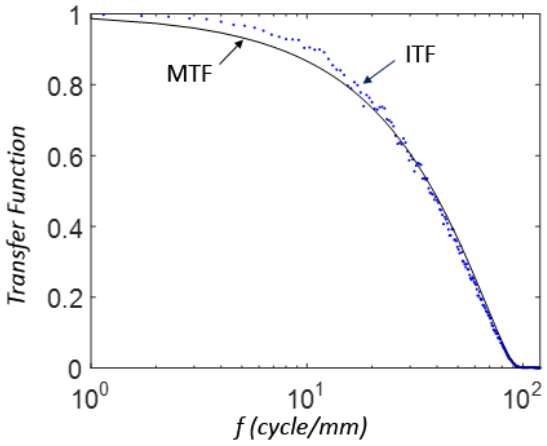

Figure 5-27: ITF calculated through the simulation of fringe projection measurement of an AM surface measurement.

Figure 5-28 shows the comparison of the ITF curves calculated with all the surface samples discussed above. All the curves are very close to each other, with a reasonably small amount of deviation. Again, this shows the fringe projection system has approximately the same ITF for different types of surfaces. In other words, the system is approximately linear when the two linearity conditions are met. This means the use of ITF

to characterize the spatial frequency response of the system for measuring rough surfaces is valid.

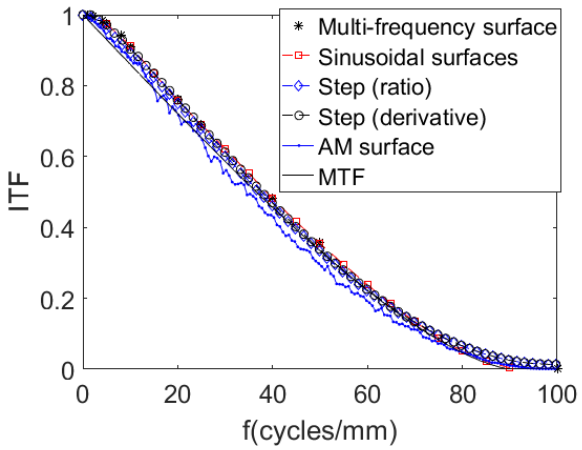

Figure 5-28: Comparison of ITFs calculated from simulations on several types of surfaces.

5.4 Experiments

The fringe projection system operates as a linear system under two linearity conditions – 1) the amplitudes of spatial frequency components on the surface are under the linearity height limit, and 2) the width of the PSF is much smaller than the spatial wavelength of the fringes. As we continue to validate our proposal of using ITF to characterize the spatial frequency response of the system, we move to our next study which is to measure the ITF experimentally.

5.4.1 Experimental Setup

The fringe projection system under investigation is shown in Figure 5-29. The system is installed on a mock-up of the LPBF machine, mimicking the geometrical configuration of the machine chamber. The projector (Qumi Q5) includes a customized projection lens illuminating a test platform at an angle of around 50°. The camera (Canon T3i) with a 60-

mm lens (Canon EF-S 60mm) is mounted approximately 200 mm above the test platform. The captured image size is around 24.4 × 16.2 mm^2, and the projection image size is approximately 48 × 36 mm^2. The test platform is mounted on a vertical translation stage such that the surface to be measured can be adjusted in order to bring it in focus. The average effective wavelength of the system is about 0.5 mm/cycle, and the pixel footprint is 4.7 μm. The object-space working *f/#* of the camera is 21. The MTF of the setup is first measured as a comparison to the ITF curve. The measured MTF is also used to calculate an ITF prediction curve through simulation.

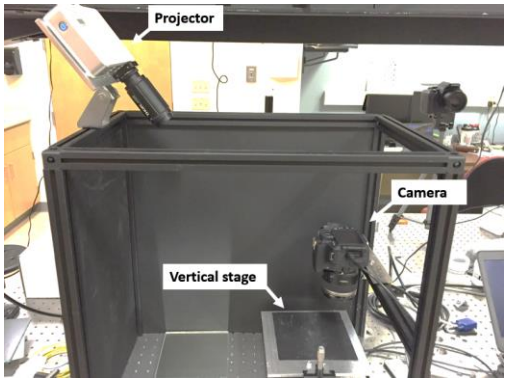

Figure 5-29: Mockup of LPBF machine with a fringe projection system installed.

5.4.2 MTF Measurements

Measurement of the MTF adopts the slanted edge MTF testing method described in ISO-12233 [121]. The benefit of imaging a knife edge at a slightly tilted angle is that the edge can be resampled with a sampling interval smaller than the camera pixel pitch; therefore, the frequency content of the measured step edge can reach over twice the Nyquist frequency.

To measure the MTF of the camera, a razor blade is placed at the focal plane of the camera and back illuminated by a flat illuminator; specifically we used a Kindle e-book

readers the flat illuminator. Figure 5-30 shows the knife edge image captured by the camera. This image is then used to calculate the MTF. The details on how to process the image can be found in the literature [118]–[122]. Mitja *et al.* have created a plugin for ImageJ that can easily calculate the MTF with a slanted edge image [124].

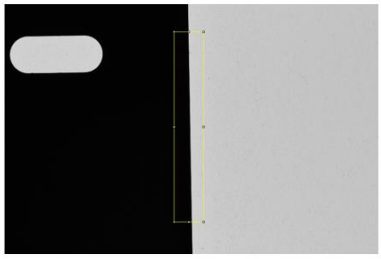

Figure 5-30: Image of a slanted knife edge for MTF measurement.

Figure 5-31 shows the measured MTF curve compared with the theoretical MTF curve. Both curves have a low cut-off frequency of 1 cycle/mm and have a high cut-off frequency of around 95 cycles/mm. The measured MTF is slightly lower than the theoretical MTF curve, which is expected because the theoretical MTF does not consider aberrations of the lens.

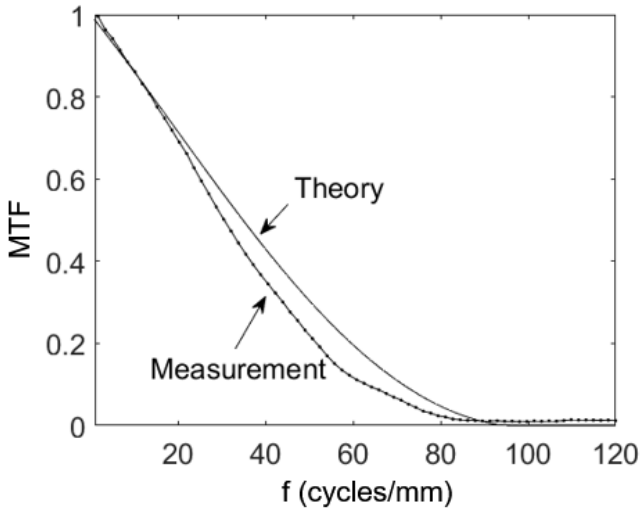

Figure 5-31: Measured MTF compared with theoretical MTF.

The MTF curve is very sensitive to defocus. Focusing by eye can lead to a significant uncertainty in the MTF measurement due to defocus. The camera has an object-space working f-number of 21 and magnification of -0.915, creating a depth of field approximately ±0.5 mm. Within this distance, the geometric paraxial blur spot is smaller than the Airy's disk. To study the influence of defocus, we repeated the MTF measurement by moving the knife edge to slightly above and below the visual best focus. Figure 5-32 shows the MTF curves measured at four distances. The "0" curve is the curve measured at visual best focus, and the "-0.5 mm" and the "+0.5 mm" curves are measured at 0.5 mm below and above "best" focus, respectively. Notice the "-0.5 mm" curve is higher than the "+0.5 mm" curve, implying the "0" curve is not measured at the true focus, and the curve for the true focus should be below the "0" position. The "-0.1" curve is measured 0.1 mm below the "0" plane. The MTF measured at this position is indeed higher than the MTF measured at the "0" position. Thus, the MTF measured at the "-0.1" position is considered the MTF at best focus.

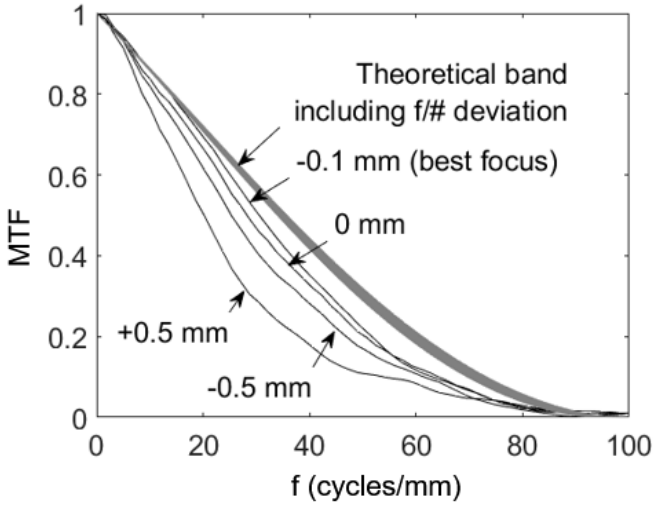

Figure 5-32: Measured MTF at various foci compared with the theoretical MTF with a confidence band which considers uncertainty in *f/#* estimation.

5.4.3 ITF Measurement with a Stepped Surface

From the previous discussion, we have concluded that using a stepped surface is the most practical approach for the ITF measurement. We have also discussed two different approaches to calculating the ITF curve from a stepped surface measurement. In this section, we will measure the ITF with both approaches and compare the results.

The ITF measurement begins with measuring the topography map of a stepped surface (VSLI 23.23 μm). This stepped surface has a calibrated step height of 23.23 μm. The amplitude of the spatial frequency components is less than the linearity limit. This artifact is made from quartz and the stepped surface is coated with a thin layer of chrome. Ideally, a fringe projection system measures diffuse surfaces, but a precision-manufactured stepped surface with a rough finish does not exist. The specular finish of the stepped surface leads to extremely weak surface scattering, meaning the optical signal captured by the camera is low. This effect makes the measurement challenging. To compensate the low scattered light, the projector is set to the highest brightness and the camera a long exposure time (30 seconds) so that the camera can gather as much scattered light as possible. The specular reflection angle is avoided to prevent pixel saturation due to the limited dynamic range of digital cameras. Figure 5-33 (a) shows a frame of acquired fringe images on the stepped surface. Even with the long exposure time and high projector brightness, the modulation depth of the fringes is still extremely low (around 10 out 255 levels of gray). Figure 5-33 (b) shows the topography measurement of the stepped surface area outlined in red in Figure 5-33 (a). Due to the low fringe modulation, the measurement is extremely noisy. This noise can be reduced by averaging many lines across the edge, which requires the alignment of the rows with respect to the edge position.

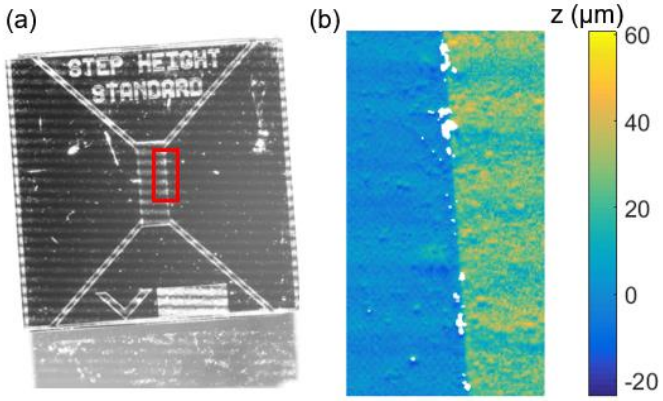

Figure 5-33: Measuring ITF using a stepped surface. (a) A frame of fringe image on the 23.23-μm stepped surface. (b) The height map of the area outlined in red.

To align the rows, the orientation of the edge must be determined. In the MTF measurement, this is achieved by taking the derivative along the x-axis and fitting a straight line around the peaks of the derivatives. This is not possible because the measured step profile is extremely noisy and a clear peak in the derivative of a line trace is not present. We determine the step orientation based on the fact that the alignment of the rows with the optimum orientation would yield the biggest slope of the averaged step profile since any angle misalignment will only make the averaged edge profile less sharp.

To compute the averaged step profile, a small shift (angle × row number) is added to each row so that the edge of each row is aligned at the same x position. Then all the data points are plotted in the same graph as shown in Figure 5-34 (a). The combined 1-D step profile has a much higher data density which can reduce the measurement noise by averaging with a larger sampling interval. Since the Nyquist sampling rate (106 cycles/mm) is already higher than the camera cut-off frequency (95 cycles/mm), there is no need to oversample the step profile. Here we chose a sampling interval equivalent to the pixel pitch. The sampling intervals are shown in Figure 5-34 (a), and the averaged step profile is shown in Figure 5-34 (b).

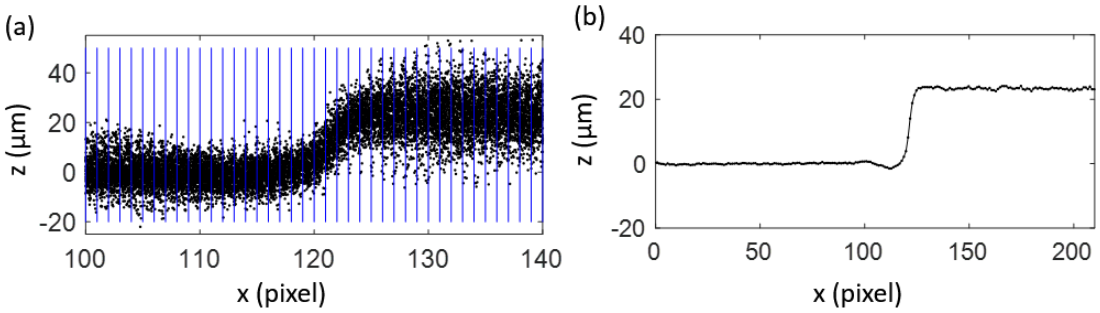

Figure 5-34: Resampling the stepped-surface measurement. (a) The combined step profile with registered edges. (b) The averaged step profile.

To find the correct alignment angle (the slope of the edge in x-y plane), the process of calculating the averaged step profile is repeated for several angles around the visually estimated angle. Then the slope of the step transition is calculated by fitting a straight line to data points around the step transition. Figure 5-35 (a) shows the averaged step profiles obtained from three alignment angles. The curve "15" is the visually determined edge angle, and curve "10" and "20" are the angles smaller and bigger than "15", respectively. Plotting the slope of the averaged step profile as a function of the alignment angle and fitting a quadratic function to the data points, the best alignment angle can be determined. Figure 5-35 (b) shows that the best alignment angle is 14.7.

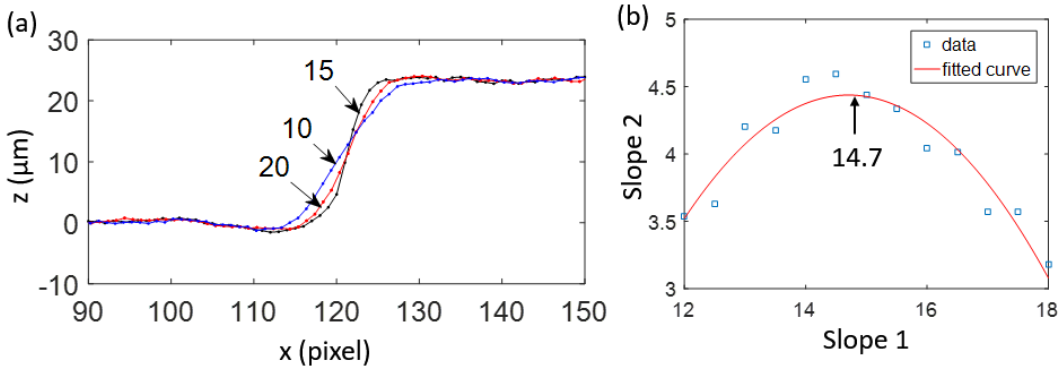

Figure 5-35: Determining the alignment angle by finding the maximum slope of the step transition in the averaged step profile. (a) Averaged edge profiles generated from different alignment angles. (b) Slope of edge versus alignment angle.

The noise on the upper and lower surfaces of the step has been greatly reduced after the averaging, but it is still not enough for a reasonable ITF calculation if a standard MTF calculation approach is followed. Even using the averaged line traces, the noise is magnified by the derivative calculation as shown in Figure 5-36 (a), causing large errors on the subsequent ITF curve as shown in Figure 5-36 (c). Since ITF is only related to the transition between the lower and the upper surfaces of the step, the noise on these two regions can be suppressed by multiplying a noise suppressing ratio. Here an empirical value of 0.1 is chosen, and multiplied to the upper and lower surface regions outlined in red as shown in Figure 5-36 (b). The transition region (between the two red outlines) is visually determined as 18 pixels in the LSF plot. The resultant LSF is much quieter, and the Fourier transform of this LSF is calculated as the new ITF. The ITF curves before and after the noise suppression are compared in Figure 5-36 (c) and (d). The noise suppression process has significantly reduced the random noise on the ITF curve at the expense of introducing an uncertainty. The primary uncertainty sources are the step transition region which is determined visually and the noise suppression noise which is determined empirically. The uncertainties of these two factors are estimated by repeating the ITF calculation with various transition regions and noise suppression ratios. The variation of the transition region is 18±2 pixels, and variation of the noise suppression ratio is from 0.1 to 0.01. We also consider the uncertainty of the slope fitting using the same approach. The variation of the slope is 14.7 ±0.5. To reduce the measurement uncertainty, the ITF curve is measured ten times and the repeatability of the ten measurements is also calculated. The total uncertainty is the root-mean-square of the sum of the four variances.

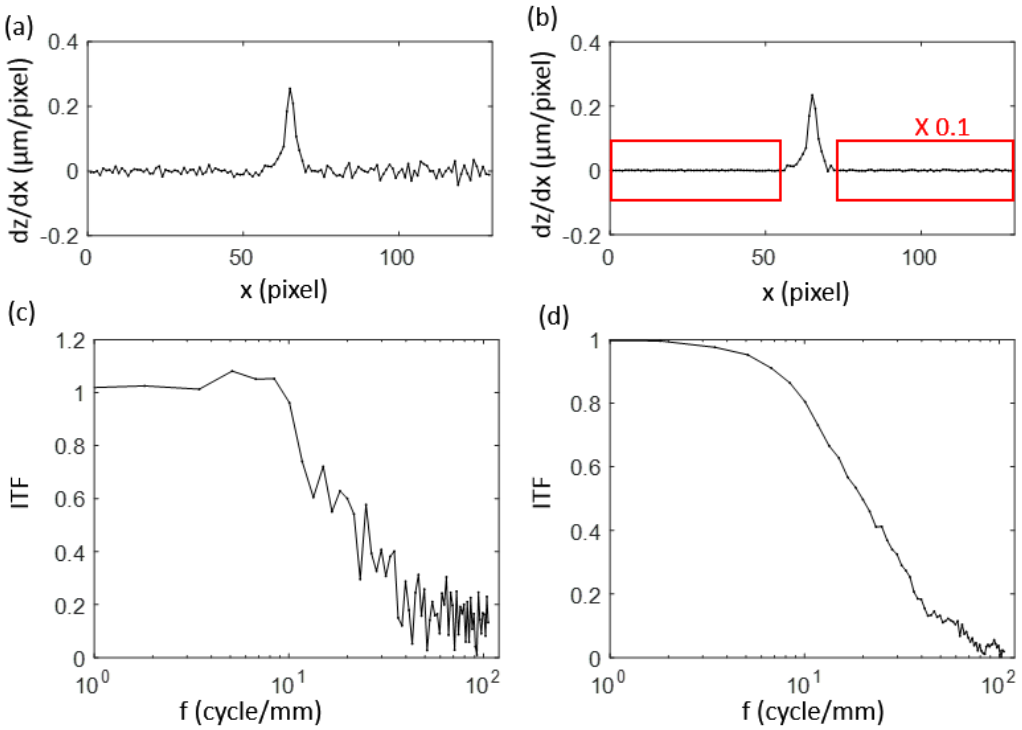

Figure 5-36: Calculation of ITF in the LSF approach with and without noise suppression. (a) and (b) are LSF before and after noise suppression. (c) and (d) are the corresponding ITFs.

Figure 5-37 shows the averaged ITF curve and the total uncertainty that includes four uncertainty factors, namely, the repeatability, the transition region, the noise suppression ratio and the slope fit. To validate the measured ITF curve, a prediction of the ITF curve is generated through simulation using the measured MTF curve. A 2D PSF is created from the measured MTF by assuming the PSF is circularly symmetric, and the convolution of the irradiance map and the PSF is calculated. The details on the ITF simulation can be found above in Section 5.3.3. The uncertainty of the ITF prediction is also calculated, and it considers the inability of imaging the step at the best focal plane. This uncertainty is the deviation of the predicted ITF curve caused by a PSF defocus of ±0.5 mm. This number equals to the range over which the paraxial blur spot is no bigger than the airy disk of the system. Comparison between the ITF measurement and the ITF prediction reveals that the

ITF measurement is valid. The measured ITF curve falls on the lower bound of the ITF prediction band meaning the stepped surface is indeed not placed at the best focus.

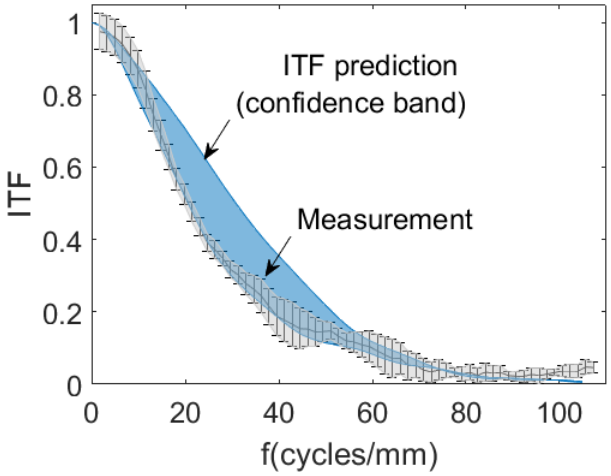

Figure 5-37: The measured ITF in the LSF approach and the confidence band which considers defocus within the depth of field.

Another approach to calculating the ITF is to calculate the ratio of the Fourier transform of the measured step profile to the Fourier transform of the mathematically perfect step profile. Similarly, the noises on the upper and lower surfaces are suppressed by multiplying a noise suppression ratio of 0.1. A window of 18 pixels at the transition region is chosen. The discontinuity of the step boundaries leads to artificially high-frequency content in the Fourier spectrum, as discussed previously. Again, we circumvent this problem by duplicating and folding the step profile about the y-axis at the end of the upper surface, creating an artificial measurement of a double-sided step, as shown in Figure 5-38. The black line is the measured step profile, and the blue line is the mathematically perfect profile. Processing the data in this way virtually eliminates edge discontinuities in the FFT calculation and reduces high-frequency artifacts.

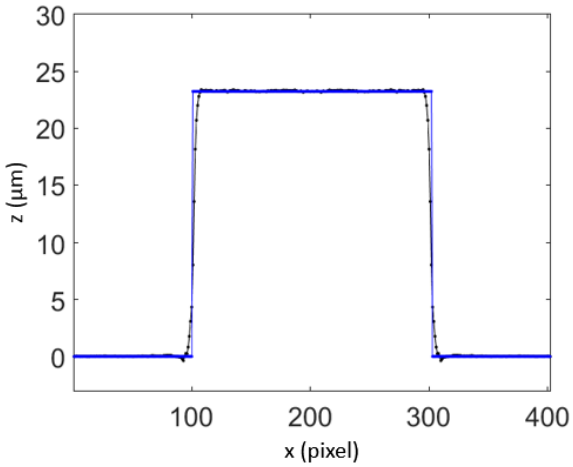

Figure 5-38: Artificially generated double-sided step profiles: the measured step profile (black) and the mathematically perfect step profile (blue).

Figure 5-39 shows the calculated ITF with this approach compared with the corresponding ITF prediction. Ten measurements of the stepped surface are used to calculate the average and standard uncertainty of the ITF curve. Again, the uncertainty of the process parameters is considered and added to the total uncertainty of the experimental ITF curve. The ITF prediction is calculated with the PSF obtained from the measured MTF with the Fourier transform ratio approach. The uncertainty of the ITF prediction is calculated with defocused PSFs for a ±0.5 mm defocus. The low-spatial-frequency region (below 10 cycles/mm) of the experimental ITF curve falls on the upper bound of the predicted ITF curve, while the mid-spatial-frequency region (10 to 50 cycles/mm) mostly falls on the lower bound of the predicted ITF band. The high-spatial-frequency region (above 90 cycles/mm) has a high measurement uncertainty due to the low signal-to-noise ratio. The amplitudes of the sinusoidal components of a stepped surface decreases with spatial frequency, meaning the signal-to-noise ratio also decreases with the spatial frequency, causing an increase of the uncertainty of the measured ITF.

Figure 5-40 compares the experimental ITFs calculated by the Fourier transform ratio approach and the LSF approach. The two curves have roughly the same shape and magnitude. The ITF calculated in the LSF approach is slightly smaller than that in the Fourier transform ratio approach. This difference is consistent with the simulation results

discussed in Section 5.3.3, but it is not clear what causes the bias. This graph shows the LSF approach has the advantage of producing lower noise at high-spatial-frequency region (over 80 cycles/mm) because it avoids calculating the division between the small amplitudes of the sinusoidal components on the stepped surface. The Fourier transform ratio approach seems more advantageous in the low-spatial-frequency region (below 20 cycles/mm) because the uncertainty band is smaller than that calculated with the LSF approach.

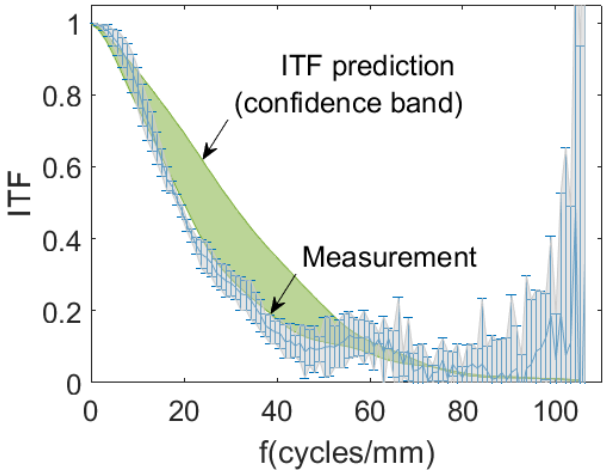

Figure 5-39: The measured ITF in the Fourier transform ratio approach and the confidence band which considers defocus within the depth of field.

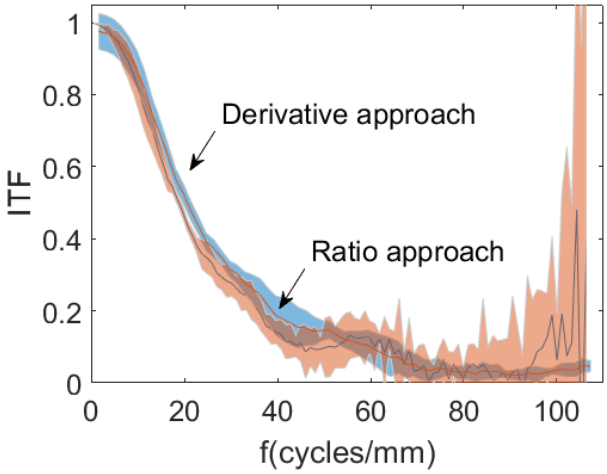

Figure 5-40: Comparison of the ITFs calculated by the Fourier-transform-ratio approach and the LSF approach.

5.5 Summary

Fringe projection is a novel technique for in situ surface inspection of the layered metal AM process. When used as a surface texture/roughness measuring tool, this technology offers many benefits over state-of-the-art interferometry methods, such as a long working distance and a low fabrication cost. However, for such an application where the surface has rich spatial frequency content, it is important to understand the spatial frequency response to evaluate the fidelity of the measurement. The ITF analysis is an appealing approach. To apply an ITF analysis, the fringe projection system must be, at least approximately, linear. The linearity requirement is met if 1) the surface variations are much smaller than the effective wavelength, and 2) the width of the PSF is much smaller than the fringe wavelength. A mathematical analysis of a phase-shifting fringe projection measurement reveals the connection between the ITF and the MTF – ITF is close to MTF when the two linearity conditions are met. To test our hypothesis, fringe projection measurements are generated with four different types of surfaces which all satisfy the linearity conditions. The simulation results are then used to calculated the ITF curves. The four ITF curves and the MTF curve are close to each other, suggesting that the ITF is surface independent, the system is approximately linear, and the ITF analysis approach is applicable.

A practical approach to measuring the ITF of a fringe projection system with a stepped surface artifact is demonstrated experimentally. A LSF approach and a Fourier transform ratio approach are demonstrated and compared. Both approaches are valid and yield similar results. The LSF approach produces less uncertainty in the high-spatial-frequency region. Predictions of the ITF curves with both approaches are also calculated through simulations. The results show the measured ITF curves are consistent with the predicted ITF curves.

CHAPTER 6: CONCLUSION

6.1 Summary of Work

In situ monitoring of the LPBF process has become more and more important to the metal AM industry. The current LPBF process suffers from poor surface finish, inconsistent mechanical properties, and fabrication defects such as pores and delamination. In-process control will help minimize these problems. A closed-loop control mechanism will improve the product quality; however, adequate in-process metrology systems for such a closed-loop control are not yet available. In-process metrology system development is an ongoing research topic. Among them, many studies are interested in thermography and machine vision techniques. Our work presents a novel approach to measure the topography of fused metal surfaces and unfused powder layers with a fringe projection technique.

The development of such a system includes design of the hardware, the software, and the calibration procedures. The design challenges associated with the limited machine space and a required measurement sensitivity have been addressed by choosing proper hardware and the appropriate effective wavelength. Two versions of the fringe projection systems have been developed. The first one is developed for measurements of the global powder bed surface and the second-generation system is for higher magnification measurements of a local fused area. The basic principles of fringe projection profilometry, including the basics of triangulation, fringe analysis, phase unwrapping, and calibration are also described in this dissertation.

The topographies produced by the in-house developed fringe projection system are very informative. Signatures of LPBF process present in the topographies are not seen by any other techniques, such as thermography and machine vision cameras. Some of these signatures include the evenness of powder layers, height variations on the fused metal surfaces, and the average height drop of the fused regions. Topography maps are measured in a layered manner, and all measurements are relative to a reference coordinate system. This provides a way of tracking relative height of powder layers and drift in layer thickness. The experimental results indicate that fringe projection is a viable solution for in situ measurements of the surface topography of the LPBF process. In situ surface topography measurements will add to our knowledge of the LPBF process, help with process optimization, and provide useful feedback for future closed-loop process control.

The performance of the fringe projection system is characterized both vertically and laterally. The vertical measurement performance is investigated by two approaches – by measuring a measurand called the surface topography repeatability and by comparing R_a roughness measurement with a commercial stylus profilometer. Three surface samples are used for measuring the surface topography repeatability and the measured values on them are 2.0 μm, 2.1 μm and 8.4 μm, respectively. A surface roughness sample with a primary wavelength of 0.72 mm is used for an intercomparison study. The R_a roughness measured by the fringe projection system is 17.9 ± 0.5 μm, and R_a measured by the contact profilometer is 18.3 ± 0.3 μm. These results indicate the proposed fringe projection system can produce accurate measurement for suitable surface samples.

Characterization of the spatial measurement performance is important for the AM applications because the surfaces generated by LPBF process contain rich spatial frequency

content. The fidelity of the measurement is subject to the spatial frequency response of the instrument. One appealing way to characterize the spatial frequency response is the ITF. We first investigated the applicability of the ITF to a fringe projection system through mathematical analysis and simulation. The results show a fringe projection system is approximately linear when 1) the amplitude of sinusoidal component on the surface is smaller than a height limit, and 2) the width of PSF is much smaller than the effective wavelength. A practical ITF measurement technique with a stepped surface artifact is then investigated through experiment. The experimental results are compared with an ITF prediction generated through simulation.

6.2 Future Work

A limitation of our current fringe projection system is that the projector brightness and camera exposure time are adjusted manually for the highest possible fringe contrast. The reflectance of the metal surface varies with the orientation of the laser scan, causing an inconsistent data drop-out rate between alternating layers of the measurements. Using the same camera settings for both scan orientations is not ideal. An automatic algorithm can be implemented to adjust the projector intensity and the camera exposure time for different surfaces. Thus, a further study regarding the implementation of a dynamic range enhancement algorithm would be worth doing. Some existing dynamic enhancement techniques are reported in the references [125], [126].

Another future work relates to application of the fringe projection measurement. The measurements taken by the proposed fringe projection system are not limited to the applications we demonstrate in this dissertation. Analysis of the topographies, investigation

on the process signatures, and correlations between the signatures and the final part quality should be new research territories. Some examples of future work in this area are a boundary finding algorithm, a surface segmentation algorithm and an investigation of the porosity.

Another future work is the applications of the ITF. This work is not covered in this dissertation and is worth studying in the future. The function of ITF is not limited to interpreting the fidelity of topography measurement as to what spatial-frequency content can be trusted; it can also be used to compensate/correct the systematic error due to spatial filtering. The damped spatial frequency content on the surface can be “re-amplified” based on the ITF curve. Thus, the spatial resolution of the instrument can be enhanced.

REFERENCES

[1] G. N. Levy, R. Schindel, and J. P. Kruth, “RAPID MANUFACTURING AND RAPID TOOLING WITH LAYER MANUFACTURING (LM) TECHNOLOGIES, STATE OF THE ART AND FUTURE PERSPECTIVES,” *CIRP Ann. - Manuf. Technol.*, vol. 52, no. 2, pp. 589–609, 2003.

[2] J. P. Kruth, “Material Incress Manufacturing by Rapid Prototyping Techniques,” *CIRP Ann. - Manuf. Technol.*, vol. 40, no. 2, pp. 603–614, 1991.

[3] B. Vandenbroucke and J. Kruth, “Selective laser melting of biocompatible metals for rapid manufacturing of medical parts,” *Rapid Prototyp. J.*, vol. 13, no. 4, pp. 196–203, Aug. 2007.

[4] “EBM for Orthopedic Implants - Additive Manufacturing | Arcam AB.” [Online]. Available: http://www.arcam.com/solutions/orthopedic-implants/.

[5] J.-P. Kruth, M. C. Leu, and T. Nakagawa, “Progress in Additive Manufacturing and Rapid Prototyping,” *CIRP Ann. - Manuf. Technol.*, vol. 47, no. 2, pp. 525–540, 1998.

[6] J. P. K. Florian Bechmann, Sebastian Berumen, Tom Craeghs, Frank Herzog, “Method for producing a three-dimensional component,” WO 2012019577 A3, 2011.

[7] “Metal 3D Printing EADS,” 2016. [Online]. Available: http://www.eos.info/press/customer_case_studies/eads.

[8] “Additive Manufacturing Solutions for orthopaedic applications,” 2016. [Online]. Available: http://www.eos.info/industries_markets/medical/orthopaedic_technology.

[9] M. Mahesh, B. Lane, A. Donmez, S. Feng, S. Moylan, R. Fesperman, M. Mani, B. Lane, A. Donmez, S. Feng, S. Moylan, and R. Fesperman, “Measurement Science Needs for Real-time Control of Additive Manufacturing Powder Bed Fusion Processes,” Gaithersburg, MD, Feb. 2015.

[10] M. W. Khaing, J. Y. H. Fuh, and L. Lu, “Direct metal laser sintering for rapid tooling: Processing and characterisation of EOS parts,” *J. Mater. Process. Technol.*, vol. 113, pp. 269–272, 2001.

[11] M. Agarwala, D. Bourell, J. Beaman, H. Marcus, and J. Barlow, “Direct selective laser sintering of metals,” *Rapid Prototyp. J.*, vol. 1, no. 1, pp. 26–36, Mar. 1995.

[12] T. T. Wohlers, “Wohlers Report,” 2016.

[13] S. Kleszczynski, J. zur Jacobsmühlen, J. T. Sehrt, and G. Witt, “Mechanical

Properties of Laser Beam Melting Components Depending on Various Process Errors," in *Digital Product and Process Development Systems*, Springer Berlin Heidelberg, 2013, pp. 153–166.

[14] D. R. Tobergte and S. Curtis, "Modeling and Experimental validation of Nickel-based super alloy (Inconel 625) made using Selective Laser Melting," in *Solid Freeform Fabrication 2013*, 2013, pp. 463–473.

[15] A. Simchi, F. Petzoldt, and H. Pohl, "On the development of direct metal laser sintering for rapid tooling," *J. Mater. Process. Technol.*, vol. 141, pp. 319–328, 2003.

[16] H. Meier and C. Haberland, "Experimental studies on selective laser melting of metallic parts," *Materwiss. Werksttech.*, vol. 39, no. 9, pp. 665–670, Sep. 2008.

[17] Y. Ning, Y. S. Wong, J. Y. H. Fuh, and H. T. Loh, "An approach to minimize build errors in direct metal laser sintering," *IEEE Trans. Autom. Sci. Eng.*, vol. 3, no. 1, pp. 73–80, 2006.

[18] A. B. Spierings, N. Herres, and G. Levy, "Influence of the particle size distribution on surface quality and mechanical properties in additive manufactured stainless steel parts," *Rapid Prototype J.*, vol. 17, no. 3, pp. 195–202, 2011.

[19] E. Yasa, J. Deckers, T. Craeghs, M. Badrossamay, and J.-P. Kruth, "INVESTIGATION ON OCCURRENCE OF ELEVATED EDGES IN SELECTIVE LASER MELTING," in *the International Solid Freeform Fabrication Symposium*, 2009, pp. 673–685.

[20] K. Abd-Elghany and D. L. Bourell, "Property evaluation of 304L stainless steel fabricated by selective laser melting," *Rapid Prototyp. J.*, vol. 18, no. 5, pp. 420–428, Jul. 2012.

[21] J. Delgado, J. Ciurana, and C. A. Rodríguez, "Influence of process parameters on part quality and mechanical properties for DMLS and SLM with iron-based materials," *Int. J. Adv. Manuf. Technol.*, vol. 60, no. 5–8, pp. 601–610, May 2012.

[22] K. Shahzad, J. Deckers, J.-P. Kruth, and J. Vleugels, "Additive manufacturing of alumina parts by indirect selective laser sintering and post processing," *J. Mater. Process. Technol.*, vol. 213, no. 9, pp. 1484–1494, 2013.

[23] S. K. Everton, M. Hirsch, P. Stravroulakis, R. K. Leach, and A. T. Clare, "Review of in situ process monitoring and in situ metrology for metal additive manufacturing," *Mater. Des.*, vol. 95, pp. 431–445, 2016.

[24] S. Berumen, F. Bechmann, S. Lindner, J.-P. Kruth, and T. Craeghs, "Quality control of laser- and powder bed-based Additive Manufacturing (AM) technologies," *Phys. Procedia*, vol. 5, pp. 617–622, 2010.

[25] T. Craeghs, S. Clijsters, E. Yasa, and J.-P. Kruth, “ONLINE QUALITY CONTROL OF SELECTIVE LASER MELTING,” in *22nd International Solid Freeform Fabrication Symposium*, 2011.

[26] T. Craeghs, S. Clijsters, J.-P. Kruth, F. Bechmann, and M.-C. Ebert, “Detection of Process Failures in Layerwise Laser Melting with Optical Process Monitoring,” *Phys. Procedia*, vol. 39, pp. 753–759, 2012.

[27] S. Clijsters, T. Craeghs, S. Buls, K. Kempen, and J.-P. Kruth, “In situ quality control of the selective laser melting process using a high-speed, real-time melt pool monitoring system,” *Int. J. Adv. Manuf. Technol.*, vol. 75, no. 5–8, pp. 1089–1101, Nov. 2014.

[28] M. Pavlov, M. Doubenskaia, and I. Smurov, “Pyrometric analysis of thermal processes in SLM technology,” *Phys. Procedia*, vol. 5, pp. 523–531, 2010.

[29] P. Lott, H. Schleifenbaum, W. Meiners, K. Wissenbach, C. Hinke, and J. Bültmann, “Design of an Optical system for the In Situ Process Monitoring of Selective Laser Melting (SLM),” *Phys. Procedia*, vol. 12, pp. 683–690, 2011.

[30] T. Furumoto, T. Ueda, M. R. Alkahari, and A. Hosokawa, “Investigation of laser consolidation process for metal powder by two-color pyrometer and high-speed video camera,” *CIRP Ann. - Manuf. Technol.*, vol. 62, no. 1, pp. 223–226, 2013.

[31] M. A. Davies, T. Ueda, R. M’Saoubi, B. Mullany, and A. L. Cooke, “On The Measurement of Temperature in Material Removal Processes,” *CIRP Ann. - Manuf. Technol.*, 2007.

[32] J. zur Jacobsmuhlen, S. Kleszczynski, G. Witt, and D. Merhof, “Detection of elevated regions in surface images from laser beam melting processes,” in *IECON 2015 - 41st Annual Conference of the IEEE Industrial Electronics Society*, 2015, pp. 001270–001275.

[33] S. Kleszczynski, J. zur Jocobsmuhlen, and J. T. Sehrt, “Error Detection in Laser Beam Melting Systems by High Resolution Imaging,” in *the Twenty Third Annual International Solid Freeform Fabrication Symposium*, 2012.

[34] J. Zur Jacobsmuhlen, S. Kleszczynski, D. Schneider, and G. Witt, “High resolution imaging for inspection of Laser Beam Melting systems,” in *2013 IEEE International Instrumentation and Measurement Technology Conference (I2MTC)*, 2013, pp. 707–712.

[35] H. Krauss, T. Zeugner, and M. F. Zaeh, “Layerwise Monitoring of the Selective Laser Melting Process by Thermography,” in *Physics Procedia*, 2014, vol. 56, pp. 64–71.

[36] H. Krauss, T. Zeugner, and M. F. Zaeh, “Thermographic process monitoring in

powderbed based additive manufacturing," 2015, vol. 1650, no. 1, pp. 177–183.

[37] A. Townsend, N. Senin, L. Blunt, R. K. Leach, and J. S. Taylor, "Surface texture metrology for metal additive manufacturing: a review," *Precis. Eng.*, vol. 46, pp. 34–47, 2016.

[38] R. W. Wygant, S. P. Almeida, and O. D. D. Soares, "Surface inspection via projection interferometry," *Appl. Opt.*, vol. 27, no. 22, pp. 4626–4630, Nov. 1988.

[39] B. Zhang, W. S. Land, J. Ziegert, A. Davies, W. S. L. Ii, J. Ziegert, and A. Davies, "In Situ Monitoring of Laser Powder Bed Fusion Additive Manufacturing Using Digital Fringe Projection Technique," in *Proceedings: ASPE 2015 Spring Topical Meeting*, 2015, pp. 47–52.

[40] B. Zhang, J. Ziegert, F. Farahi, and A. Davies, "In situ surface topography of laser powder bed fusion using fringe projection," *Addit. Manuf.*, vol. 12, 2016.

[41] S. Zhang, "Recent progresses on real-time 3D shape measurement using digital fringe projection techniques," *Opt. Lasers Eng.*, vol. 48, no. 2, pp. 149–158, Feb. 2010.

[42] C. Reich, R. Ritter, and J. Thesing, "3-D shape measurement of complex objects by combining photogrammetry and fringe projection," *Opt. Eng.*, vol. 39, no. 1, p. 224, Jan. 2000.

[43] X. Su and Q. Zhang, "Dynamic 3-D shape measurement method: A review," *Opt. Lasers Eng.*, vol. 48, no. 2, pp. 191–204, 2010.

[44] B. Li, Y. Wang, J. Dai, W. Lohry, and S. Zhang, "Some recent advances on superfast 3D shape measurement with digital binary defocusing techniques," *Opt. Lasers Eng.*, vol. 54, pp. 236–246, Mar. 2014.

[45] F. Lilley, M. J. Lalor, D. R. Burton, and B. Street, "Robust fringe analysis system for human body shape measurement," *Opt. Eng.*, vol. 39, no. 1, p. 187, Jan. 2015.

[46] "breuckmann stereoSCAN neo AICON 3D Systems." [Online]. Available: http://www.aniwaa.com/product/3d-scanners/aicon-3d-systems-breuckmann-stereoscan-neo/.

[47] S. H. Rowe and W. T. Welford, "Surface Topography of Non-optical Surfaces by Projected Interference Fringes," *Nature*, vol. 216, no. 5117, pp. 786–787, Nov. 1967.

[48] M. Takeda, H. Ina, and S. Kobayashi, "Fourier-transform method of fringe-pattern analysis for computer-based topography and interferometry," *J. Opt. Soc. Am.*, vol. 72, no. 1, p. 156, 1982.

[49] M. Takeda and K. Mutoh, “Fourier transform profilometry for the automatic measurement of 3-D object shapes,” *Appl. Opt.*, vol. 22, no. 24, p. 3977, 1983.

[50] X. Su and W. Chen, “Fourier transform profilometry: a review,” *Opt. Lasers Eng.*, vol. 35, no. 5, pp. 263–284, 2001.

[51] J. Salvi, S. Fernandez, T. Pribanic, and X. Llado, “A state of the art in structured light patterns for surface profilometry,” *Pattern Recognit.*, vol. 43, no. 8, pp. 2666–2680, 2010.

[52] J. Salvi, J. Pagès, and J. Batlle, “Pattern codification strategies in structured light systems,” *Pattern Recognit.*, vol. 37, no. 4, pp. 827–849, Apr. 2004.

[53] M. K. Kaims, W. Juptner, and W. Osten, “Automatic Adaption of Projected Fringe Patterns using a programmable LCD-Projector,” 1997, vol. 3100, pp. 156–165.

[54] P. Gupta, “Gray Code Composite Pattern Structured Light Illumination,” p. 100, 2007.

[55] Q. Kemao, “Two-dimensional windowed Fourier transform for fringe pattern analysis: Principles, applications and implementations,” *Opt. Lasers Eng.*, vol. 45, no. 2, pp. 304–317, Feb. 2007.

[56] L. Huang, Q. Kemao, B. Pan, and A. K. Asundi, “Comparison of Fourier transform, windowed Fourier transform, and wavelet transform methods for phase extraction from a single fringe pattern in fringe projection profilometry,” *Opt. Lasers Eng.*, vol. 48, no. 2, pp. 141–148, Feb. 2010.

[57] Y. Hu, J. Xi, J. Chicharo, and Z. Yang, “Improved three-step phase shifting profilometry using digital fringe pattern projection,” in *Proceedings - Computer Graphics, Imaging and Visualisation: Techniques and Applications, CGIV’06*, 2006, vol. 2006, no. July, pp. 161–166.

[58] S. Zhang, D. Van Der Weide, and J. Oliver, “Superfast phase-shifting method for 3-D shape measurement,” *Opt. Express*, vol. 18, no. 9, p. 9684, Apr. 2010.

[59] H. A. Z. and C. L. W. Richard M. Goldstein, R. M. Goldstein, H. A. Zebker, and C. L. Werner, “Satellite Radar Interferometry: Two-dimensional Phase Unwrapping,” *Radio Science*, vol. 23, no. 4. pp. 713–720, 1988.

[60] M. Gdeisat and F. Lilley, “Two-Dimensional Phase Unwrapping Problem,” 2013. [Online]. Available: http://www.ljmu.ac.uk/GERI/CEORG_Docs/Two_Dimensional_Phase_Unwrapping_Final.pdf. [Accessed: 26-May-2014].

[61] Q. Kemao, W. Gao, and H. Wang, “Windowed Fourier-filtered and quality-guided phase-unwrapping algorithm,” *Appl. Opt.*, vol. 47, no. 29, pp. 5420–5428, 2008.

[62] R. Talebi and J. Johnson, “Binary Code Pattern Unwrapping Technique in Fringe Projection Method,” in *17th International Conference on Image Processing, Computer Vision, & Pattern Recognition*, 2013.

[63] K. Itoh, “Analysis of the phase unwrapping algorithm.,” *Appl. Opt.*, vol. 21, no. 14, p. 2470, 1982.

[64] T. R. Judge and P. J. Bryanston-Cross, “A review of phase unwrapping techniques in fringe analysis,” *Opt. Lasers Eng.*, vol. 21, no. 4, pp. 199–239, Jan. 1994.

[65] P. S. Huang, “Novel method for structured light system calibration,” *Opt. Eng.*, vol. 45, no. 8, p. 83601, 2006.

[66] J. Heikkila and O. Silven, “A four-step camera calibration procedure with implicit image correction,” in *Proceedings of IEEE Computer Society Conference on Computer Vision and Pattern Recognition*, 1997, pp. 1106–1112.

[67] Y. Fu, Y. Wang, W. Wang, and J. Wu, “Least-squares calibration method for fringe projection profilometry with some practical considerations,” *Optik (Stuttg).*, vol. 124, no. 19, pp. 4041–4045, 2013.

[68] L. Huang, P. S. K. Chua, and A. Asundi, “Least-squares calibration method for fringe projection profilometry considering camera lens distortion.,” *Appl. Opt.*, vol. 49, no. 9, pp. 1539–1548, Mar. 2010.

[69] M. Vo, Z. Wang, T. Hoang, and D. Nguyen, “Flexible calibration technique for fringe-projection-based three-dimensional imaging.,” *Opt. Lett.*, vol. 35, no. 19, pp. 3192–3194, 2010.

[70] H. Liu, W. H. Su, K. Reichard, and S. Yin, “Calibration-based phase-shifting projected fringe profilometry for accurate absolute 3D surface profile measurement,” *Opt. Commun.*, vol. 216, no. 1–3, pp. 65–80, 2003.

[71] T. M. Hoang, “Simple Gamma Correction for Fringe Projection Profilometry System,” *Image (Rochester, N.Y.)*, vol. 1428, no. 2001, pp. 4503–4503, 2010.

[72] K. Liu, Y. Wang, D. L. Lau, Q. Hao, and L. G. Hassebrook, “Gamma model and its analysis for phase measuring profilometry.,” *J. Opt. Soc. Am. A. Opt. Image Sci. Vis.*, vol. 27, no. 3, pp. 553–62, 2010.

[73] S. Zhang, “Comparative study on passive and active projector nonlinear gamma calibration,” *Appl. Opt.*, vol. 54, no. 13, p. 3834, 2015.

[74] T. Hoang, B. Pan, D. Nguyen, and Z. Wang, “Generic gamma correction for accuracy enhancement in fringe-projection profilometry.,” *Opt. Lett.*, vol. 35, no. 12, pp. 1992–1994, 2010.

[75] M. J. Baker, J. F. Chicharo, and J. Xi, “An investigation into temporal gamma luminance for digital fringe fourier transform profilometers,” in *2007 IEEE International Symposium on Intelligent Signal Processing, WISP*, 2007, pp. 1–6.

[76] H. Guo, H. He, and M. Chen, “Gamma correction for digital fringe projection profilometry.,” *Appl. Opt.*, vol. 43, no. 14, pp. 2906–14, May 2004.

[77] P. Zhou, X. Liu, Y. He, and T. Zhu, “Phase error analysis and compensation considering ambient light for phase measuring profilometry,” *Opt. Lasers Eng.*, vol. 55, pp. 99–104, 2014.

[78] Z. Cai, X. Liu, X. Peng, Z. Zhang, H. Jiang, Y. Yin, and S. Huang, “Phase error compensation methods for high-accuracy profile measurement,” *Meas. Sci. Technol.*, vol. 27, no. 4, p. 45201, 2016.

[79] S. Zhang and P. S. Huang, “Phase Error Compensation for a 3-D Shape Measurement System Based on the Phase-Shifting Method,” in *Optics East 2005*, 2005, vol. 6000, p. 60000E–60000E–10.

[80] S. Ma, C. Quan, R. Zhu, and C. J. Tay, “Investigation of phase error correction for digital sinusoidal phase-shifting fringe projection profilometry,” *Opt. Lasers Eng.*, vol. 50, no. 8, pp. 1107–1118, 2012.

[81] P. S. Huang, “High-speed 3-D shape measurement based on digital fringe projection,” *Opt. Eng.*, vol. 42, no. 1, p. 163, 2003.

[82] J. Xu, N. Xi, C. Zhang, Q. Shi, and J. Gregory, “Real-time 3D shape inspection system of automotive parts based on structured light pattern,” *Opt. Laser Technol.*, vol. 43, no. 1, pp. 1–8, 2011.

[83] J. Xu, N. Xi, C. Zhang, J. Zhao, B. Gao, and Q. Shi, “Rapid 3D surface profile measurement of industrial parts using two-level structured light patterns,” *Opt. Lasers Eng.*, vol. 49, no. 7, pp. 907–914, 2011.

[84] H.-N. Yen, D.-M. Tsai, and J.-Y. Yang, “Full-Field 3-D Measurement of Solder Pastes Using LCD-Based Phase Shifting Techniques,” *IEEE Trans. Electron. Packag. Manuf.*, vol. 29, no. 1, pp. 50–57, Jan. 2006.

[85] T.-W. Hui and G. K.-H. Pang, “Solder paste inspection using region-based defect detection,” *Int. J. Adv. Manuf. Technol.*, vol. 42, no. 7–8, pp. 725–734, Jun. 2009.

[86] K. Leonhardt, U. Droste, and H. J. Tiziani, “Microshape and rough-surface analysis by fringe projection.,” *Appl. Opt.*, vol. 33, no. 31, pp. 7477–7488, 1994.

[87] S. Toyooka and Y. Iwaasa, “Automatic profilometry of 3-D diffuse objects by spatial phase detection,” *Appl. Opt.*, vol. 25, no. 10, pp. 1630–1633, 1986.

[88] M. R. Foreman, C. L. Giusca, J. M. Coupland, P. Török, and R. K. Leach, “Determination of the transfer function for optical surface topography measuring instruments—a review,” *Meas. Sci. Technol.*, vol. 24, no. 5, p. 52001, 2013.

[89] K. Creath and J. Wyant, “Phase Shifting Interferometry,” in *Optical Shop Testing*, 1992, p. 602.

[90] Y.-L. Xiao, J. Xue, and X. Su, “Robust self-calibration three-dimensional shape measurement in fringe-projection photogrammetry.,” *Opt. Lett.*, vol. 38, no. 5, pp. 694–6, Mar. 2013.

[91] B. Li and S. Zhang, “Structured light system calibration method with optimal fringe angle.,” *Appl. Opt.*, vol. 53, no. 33, pp. 7942–7950, 2014.

[92] J.-Y. Bouguet, “Camera Calibration Toolbox,” 2013. [Online]. Available: http://www.vision.caltech.edu/bouguetj/calib_doc/.

[93] I. Martynov, J. K. Kamarainen, and L. Lensu, “Projector calibration by ‘Inverse camera calibration,’” in *Image Analysis*, vol. 6688, Springer Berlin Heidelberg, 2011, pp. 536–544.

[94] L. Fit, “Levenberg-Marquardt algorithm Matlab code.” .

[95] H. Guo, H. He, Y. Yu, and M. Chen, “Least-squares calibration method for fringe projection profilometry,” *Opt. Eng.*, vol. 44, no. 3, p. 33603, Mar. 2005.

[96] L. C. Chen and C. C. Liao, “Calibration of 3D surface profilometry using digital fringe projection,” *Meas. Sci. Technol.*, vol. 16, no. 8, pp. 1554–1566, 2005.

[97] D. Purcell, A. Davies, and F. Farahi, “Effective wavelength calibration for moiré fringe projection,” *Appl. Opt.*, vol. 45, no. 34, p. 8629, 2006.

[98] D. K. R. Philip R. Bevington, *Data Reduction and Error Analysis for Physical Sciences*, 3rd ed. McGrw-Hill, 2002.

[99] G. Wolberg, “Digital Image Wrapping,” in *Digital Image Wrapping*, Los Alamitos,CA, USA: IEEE Computer Society Press, 1994, pp. 41–56.

[100] Texas Instruments, “DLP 0.45 WXGA DMD.” pp. 1–36, 2013.

[101] Texas Instruments, “Gemetric optics for DLP,” 2013.

[102] X. Colonna De Lega and P. de Groot, “Lateral resolution and instrument transfer function as criteria for selecting surface metrology instruments,” *Imaging Appl. Opt. Tech. Dig.*, pp. 1–3, 2012.

[103] “Guidlines for evaluating and expressing the uncertainty of NIST measurement results,” p. 14, 1994.

[104] S. Wang, C. J. Tay, C. Quan, and H. M. Shang, “Investigation of membrane deformation by a fringe projection method.,” *Appl. Opt.*, vol. 41, no. 1, pp. 101–7, 2002.

[105] R. Windecker, S. Franz, and H. J. Tiziani, “Optical roughness measurements with fringe projection,” *Appl. Opt.*, vol. 38, no. 13, p. 2837, May 1999.

[106] BIPM, “GUM: Evaluation of measurement data - Guide to the expression of uncertainty in measurement,” 2008.

[107] ISO25178-604:2013, “Geometrical product specifications (GPS) - Surface texture: Areal - Part 604: Nominal characteristics of non-contact (coherence scanning interferometry) instruments,” no. 117101, pp. 1–4, 2013.

[108] “Fowler No. 52-720-000 Specifications.” .

[109] B. Zhang, J. Ziegert, F. Farahi, and A. Davies, “In situ surface topography of laser powder bed fusion using fringe projection,” *Addit. Manuf.*, vol. 12, pp. 100–107, 2016.

[110] B. Zhang, J. Ziegert, and A. Davies, “In Situ Surface Metrology of Laser Powder Bed Fusion Processes Using Fringe Projection 2 Department of Mechanical Engineering and Engineering Science,” in *Proceedings ASPE 2016 Summer Topical Meeting*, 2016, no. 1.

[111] P. de Groot, X. C. De Lega, and X. C. de Lega, “Interpreting interferometric height measurements using the instrument transfer function,” *Fringe 2005*, vol. 2005, pp. 30–37, 2006.

[112] W. Xie, P. Lehmann, and J. Niehues, “Lateral resolution and transfer characteristics of vertical scanning white-light interferometers,” *Appl. Opt.*, vol. 51, no. 11, p. 1795, Apr. 2012.

[113] R. Leach, C. Giusca, A. Henning, B. Sherlock, and J. Coupland, “ISO Definition of Resolution for Surface Topography Measuring Instruments,” in *Fringe 2013*, Berlin, Heidelberg: Springer Berlin Heidelberg, 2014, pp. 405–410.

[114] P. Berssenbrügge, M. Dekiff, B. Kemper, C. Denz, and D. Dirksen, “Characterization of the 3D resolution of topometric sensors based on fringe and speckle pattern projection by a 3D transfer function,” *Opt. Lasers Eng.*, vol. 50, no. 3, pp. 465–472, 2012.

[115] G. D. Boreman, “MTF in Optical Systems,” *Modul. Transf. Funct. Opt. Electr-Optical Syst.*, pp. 1–10, 2001.

[116] T. Su, A. Maldonado, P. Su, and J. H. Burge, “Instrument transfer function of slope measuring deflectometry systems.,” *Appl. Opt.*, vol. 54, no. 10, pp. 2981–90, 2015.

[117] P. Z. Takacs, M. X. Li, K. Furenlid, and E. L. Church, “A step-height standard for surface profiler calibration,” in *Optical Scattering*, 1993, pp. 235–244.

[118] S. E. Reichenbach, S. K. Park, and R. Narayanswamy, “Characterizing digital image acquisition devices,” *Opt. Eng.*, vol. 30, no. 2, p. 170, 1991.

[119] P. D. Burns, “Slanted-Edge MTF for Digital Camera and Scanner Analysis,” *Burns*, vol. 3, pp. 135–138, 2000.

[120] P. D. Burns, “Refined slanted-edge measurement for practical camera and scanner testing,” *IS&T PICS Conf.*, pp. 191–195, 2002.

[121] M. Estribeau, “Fast MTF measurement of CMOS imagers using ISO 12333 slanted-edge methodology,” *Proc. SPIE*, vol. 5251, pp. 243–252, 2004.

[122] K. Masaoka, T. Yamashita, Y. Nishida, and M. Sugawara, “Modified slanted-edge method and multidirectional modulation transfer function estimation,” *Opt. Express*, vol. 22, no. 5, p. 6040, 2014.

[123] J. E. Greivenkamp, *Field Guide to Geometrical Optics*. Bellingham, Washington: SPIE Press, 2003.

[124] C. Mitja, J. Escofet, A. Tacho, and R. Revuelta, “Slanted Edge MTF,” 2011.

[125] G. Babaie, M. Abolbashari, and F. Farahi, “Dynamics range enhancement in digital fringe projection technique,” *Precis. Eng.*, vol. 39, pp. 243–251, 2014.

[126] S. Zhang and S.-T. Yau, “High dynamic range scanning technique,” *Opt. Eng.*, vol. 48, p. 33604, 2009.

APPENDIX A: MATLAB CODE EXAMPLES

Phase shifting algorithm

```
function [phi,mask1,mask2,mask3] = phase_shift(path,ind)
a2 = 0;
a1 = 0;
a0 = 0;
n_step=numel(ind);
file=dir([path,'*.jpg']);
mask1=zeros(3456,5184); %saturation mask
mask3=zeros(3456,5184); %shadow mask
%% read images
for c = 1:n_step
    img_dir=file(ind(c)).name;
    Ii=imread([path,img_dir]);
    Ii=rgb2gray(Ii);  % convert image to gray scale image
    Ii=double(Ii);
         sat=Ii>254;
         sha=Ii<40;
         mask1=mask1+sat;
         mask3=mask3+sha;
         % Least-square algorithms(optical shop testing 14.7.2)
         delta = c*2*pi/n_step;
         a2 = a2 + Ii*sin(delta);
         a1 = a1 + Ii*cos(delta);
         a0 = a0 + Ii;
end
%% N step phase shifting
phi = atan2(-a2,a1);
mod = 2*sqrt(a1.^2+a2.^2)./a0;
amp=2*sqrt(a1.^2+a2.^2)./n_step;
bias=a0./n_step;
%mask for saturation
mask1=logical(mask1);
% Definition of saturation pixel: One and more values are
saturated(255)
%mask for low modulation
th2=max(mod(:));
mask2=mod<0.07*th2;
%mask for dark shadow
mask3(mask3<n_step)=0;
mask3=logical(mask3);
end
```

Phase Unwrapping Algorithm

```
%Unwrap the image using the Itoh algorithm: the second method is
performed
%by sequentially unwrapping the all columns, one at a time.
function [Iunwrapped] = itoh_unwrap_c(Iwrapped);
[m n] = size(Iwrapped);
Iunwrapped = Iwrapped;
%% unwrapped columns
for i=1:n
    Iunwrapped(end:-1:1,i) = unwrap(Iunwrapped(end:-1:1,i));
end
% Then sequentially unwrap all the rows
for i=1:m
    Iunwrapped(i,:) = unwrap(Iunwrapped(i,:));
end
end


% referece-guided phaes unwrapping
function phi_u=unwrap_ref(phi,phi_ref)
% phi_ref is reference phase map
phi2=phi+pi;
phi2 = phi2 +2*pi*round((phi_ref-phi2)/2/pi);
phi_u=phi2;
end
```

Legendre Fitting Algorithm

```
function [Z,S0,S1,S2,S3]=Legendrefit(w);

%% preparation (Do not modity)
[k1,k2]=size(w);
[x, y] = meshgrid(1:k2, 1:k1);
x1=x;
y1=y;
x=x(:);
y=y(:);
w=w(:);
x=x(~isnan(w));
y=y(~isnan(w));
w=w(~isnan(w));

x2=x.*x;
y2=y.*y;
xy=x.*y;

%% calculate coefficients
k=size(x,1);
m=ones(k,10);
m(:,1)=ones(k,1); %L0
m(:,2)=x; % L1
m(:,3)=y; % L2
m(:,4)=(3*x2-1)/2; %L3
m(:,5)=xy; %L4
m(:,6)=(3*y2-1)/2; %L5
m(:,7)=x.*(5*x2-3)/2; %L6
m(:,8)=y.*(3*x2-1)/2; %L7
m(:,9)=x.*(3*y2-1)/2; %L8
m(:,10)=y.*(5*y2-3)/2; %L9
Z=m\w;

M0=Z(1)*ones(k1,k2); %zero order
M1=Z(2)*x1; %first order tilt
M2=Z(3)*y1;
M3=Z(4)*(3*x1.^2-1)/2; %second order porablic
M4=Z(5)*x1.*y1;
M5=Z(6)*(3*y1.^2-1)/2;
M6=Z(7)*x1.*(5*x1.^2-3)/2; %third order
M7=Z(8)*y1.*(3*x1.^2-1)/2;
M8=Z(9)*x1.*(3*y1.^2-1)/2;
M9=Z(10)*y1.*(5*y1.^2-3)/2;

S0=M0;
S1=M1+M2;
S2=M3+M4+M5;
S3=M6+M7+M8+M9;
end
```

Fourier Filtering

```
function [Zr2,FT1,FT2]=F_filter(Zr,fx,fy);

%% Spatial filtering
[m,n]=size(Zr);
cenY=m/2+1;
cenX=n/2+1;
fy = 25; % filted spatial frequency y component
fx = 12;
rx = 3;    % filter half size x component
ry = 11;
FT1=fftshift(fft2(Zr));
FT2 = FT1;
% 1st order filtering
FT2(floor(cenY-fy-ry):ceil(cenY-fy+0.5*ry),floor(cenX-fx-rx):ceil(cenX-
fx+rx))=0;
FT2(floor(cenY+fy-0.5*ry):ceil(cenY+fy+ry),floor(cenX+fx-
rx):ceil(cenX+fx+rx))=0;
% 2nd order filtering
FT2(floor(cenY-2*fy-ry):ceil(cenY-2*fy+ry),floor(cenX-2*fx-
1.2*rx):ceil(cenX-2*fx+1.2*rx))=0;
FT2(floor(cenY+2*fy-ry):ceil(cenY+2*fy+ry),floor(cenX+2*fx-
1.2*rx):ceil(cenX+2*fx+1.2*rx))=0;
% 3rd order filtering
FT2(floor(cenY-3*fy-ry):ceil(cenY-3*fy+ry),floor(cenX-3*fx-
rx):ceil(cenX-3*fx+rx))=0;
FT2(floor(cenY+3*fy-ry):ceil(cenY+3*fy+ry),floor(cenX+3*fx-
rx):ceil(cenX+3*fx+rx))=0;
% 4th order filtering
FT2(floor(cenY-4*fy-ry):ceil(cenY-4*fy+ry),floor(cenX-4*fx-
rx):ceil(cenX-4*fx+rx))=0;
FT2(floor(cenY+4*fy-ry):ceil(cenY+4*fy+ry),floor(cenX+4*fx-
rx):ceil(cenX+4*fx+rx))=0;
% 5th roder filtering
FT2(floor(cenY-5*fy-ry):ceil(cenY-5*fy+ry),floor(cenX-5*fx-
rx):ceil(cenX-5*fx+rx))=0;
FT2(floor(cenY+5*fy-ry):ceil(cenY+5*fy+ry),floor(cenX+5*fx-
rx):ceil(cenX+5*fx+rx))=0;
% 6th roder filtering
FT2(floor(cenY-6*fy-ry):ceil(cenY-6*fy+ry),floor(cenX-6*fx-
rx):ceil(cenX-6*fx+rx))=0;
FT2(floor(cenY+6*fy-ry):ceil(cenY+6*fy+ry),floor(cenX+6*fx-
rx):ceil(cenX+6*fx+rx))=0;
% 7th roder filtering
FT2(floor(cenY-7*fy-ry):ceil(cenY-7*fy+ry),floor(cenX-7*fx-
rx):ceil(cenX-7*fx+rx))=0;
FT2(floor(cenY+7*fy-ry):ceil(cenY+7*fy+ry),floor(cenX+7*fx-
rx):ceil(cenX+7*fx+rx))=0;
Zr2 = ifft2(ifftshift(FT2));
Zr2 = real(Zr2);

end
```